ADVANCED BROADBAND CARS MICROSCOPY BASED ON A SUPERCONTINUUM-GENERATING PHOTONIC CRYSTAL FIBER

A THESIS SUBMITTED TO THE
COMMITTEE ON GRADUATE STUDIES
IN PARTIAL FULFILLMENT OF THE REQUIREMENTS
FOR THE DEGREE OF
DOCTOR OF PHILOSOPHY IN THE FACULTY OF
ARTS AND SCIENCE

TRENT UNIVERSITY
Peterborough, Ontario, Canada

Materials Science Ph. D. Graduate Program
September 2019

Abstract

Advanced broadband CARS microscopy based on a supercontinuum-generating photonic crystal fiber

Jeremy Porquez

I have developed and improved a coherent anti-Stokes Raman scattering (CARS) microscope based on the spectral focusing (SF) technique. The CARS microscope uses an 800 nm oscillator and a photonic crystal fibre module to generate the supercontinuum Stokes. The photonic crystal fibre was originally designed to generate light beyond 945 nm which is useful for CARS microscopy in the CH/OH frequencies but essentially prevents access to the important fingerprint region at lower frequencies. With expert and nontraditional approaches to generating supercontinuum with sufficient power at wavelengths below 945 nm, I substantially extend the usefulness of the module for SF-CARS microscopy deep into the fingerprint region. Moreover, with the invention of a dynamic supercontinuum generation scheme we call "spectral surfing," I improve both the brightness of the CARS signal and extend the accessible CARS frequency range to frequencies as low as 350 cm^{-1} and as high as 3500 cm^{-1}—all in a single scan-window. I demonstrate the capabilities of our broadband SF-CARS system through CARS and four-wave mixing hyperspectroscopy on samples such as astaxanthin, lily pollen and glass; liquid chemicals such as benzonitrile, nitrobenzene and dimethyl sulfoxide; and on pharmaceutical samples such as acetaminophen, ibuprofen, and cetirizine. Furthermore, In search of more useful Stokes supercontinuum sources, I compare the performance of two commercial photonic crystal fibre modules for use in SF-CARS applications, ultimately finding that one module provides better spectral characteristics for static supercontinuum use, while the other provides improved characteristics when spectral surfing is implemented.

Keywords: nonlinear microscopy; spectroscopy, coherent anti-Stokes Raman scattering; supercontinuum generation; scanning microscopy; vibrational spectroscopy.

Preface

Chemical mapping allows us to understand the composition and spatial distribution of compounds. One powerful chemical mapping technique is coherent anti-Stokes Raman scattering (CARS) microscopy. CARS microscopy works by probing chemical bonds in a sample by using only light. It was first implemented by Duncan *et al.* in 1982 [1] using the boxcars geometry—a setup having non-collinear laser beams incident on a sample. Because of the technical difficulty of implementing boxCARS for imaging, CARS was relegated to niche applications in spectroscopy. In 1999 Zumbusch *et al.* [2] showed that serendipitous CARS signals are formed in the tight focusing of a microscope, thus establishing simple CARS imaging. Since then, the development of CARS microscopy has flourished, and hundreds of papers have been published on its development over the past two decades.

There is still so much work left to do to improve CARS microscopy. Even though CARS microscopy can perform quick and easy chemical mapping, it is still not a popular research tool since most CARS microscopes are relegated to probing carbon-hydrogen bonds, and are thus mostly concerned with biomedical lipid imaging. There has been a concerted effort in CARS development to find effective and simple ways to extend CARS microscopy across a much wider vibrational frequency landscape, and particularly to lower frequencies in the so-called spectroscopic fingerprint region.

In this thesis, I describe how we have expanded the capability of our multimodal CARS microscope to probe a wide range of chemical bonds and vibrational frequencies. The document is divided into six chapters, four of which are based on four of my first-authored peer-reviewed publications. This thesis assumes that the reader has some basic background in basic optics and electromagnetic theory. Words that may seemntoo technical for the reader are *italicized* as they appear first in the text and have corresponding definitions located in either the List of Abbreviations or the Glossary for convenience. The first chapter educates the reader some advanced concepts on optics, CARS, and its various implementations. And since we do CARS microscopy, using broad-wavelength light called a supercontinuum, we also discuss some details about supercontinuum generation. The second chapter discusses how we generate supercontinua to allow our microscope to probe a wide range of chemical bonds. The third chapter discusses a more advanced light generation technique called "spectral surfing", allowing our microscope to probe a wider range of chemical bonds at lower intensity. Spectral surfing has placed our system on par with other world-class CARS systems [3]. In some ways, the experimental CARS microscopy capabilities that I describe in this thesis are currently the best in the world. In the fourth chapter, we explore CARS microscopy using a different supercontinuum source as we search for ways to generate stronger and more stable signals. The fifth chapter presents a demonstration of our system via application to pharmaceutical drug characterization. This is a non-biomedical application for our multimodal CARS microscope that makes good use of our newly-expanded access to the fingerprint spectral region. Finally, the sixth chapter gives a summary of this thesis.

References

1. Duncan, M. D., Reintjes, J. & Manuccia, T. J. Scanning coherent anti-Stokes Raman microscope. *Optics Letters* **7,** 350 (1982).
2. Zumbusch, A., Holtom, G. R. & Xie, X. S. Three-Dimensional Vibrational Imaging by Coherent Anti-Stokes Raman Scattering. *Physical Review Letters* **82,** 4142–4145 (1999).
3. Camp Jr, C. H. *et al.* High-speed coherent Raman fingerprint imaging of biological tissues. *Nature Photonics* **8,** 627–634 (2014).

Acknowledgments

I would to thank the following...

My supervisor, Aaron Slepkov, for guiding me throughout my Ph. D. Our continuous and almost daily discussions helped me know a lot of things in my field. His great attitude towards research has allowed my scientific creativity to flourish, and I was able to present at several conferences and published several peer-reviewed articles, all the while having fun doing research.

The members of my thesis committee, Rachel Wortis and Franco Gaspari, for their insights and for helping me understand how to communicate my work better.

My labmates, Joel Tabarangao and Ryan Cole, for sharing their knowledge and helping me whenever I needed. They supplied constant stimulus for my curiosity and answered questions that would jump start my research. Without these gentlemen, it may have taken longer for me to publish my first paper.

Alan Godfrey for developing a multimode fiber coupling mechanism for the high-resolution spectrometer we loaned from the National Research Council (NRC) at Ottawa and Emily Korfanty for helping us out in writing the initial LabView code for the motorized rotation mount.

The following staff at the NRC—Andrew Ridsdale, for assisting us with the loan of a high-resolution spectrometer, an optical spectrum analyzer, and the FemtoWHITE

800 supercontinuum generating fiber module and for assisting us when we did experiments in the NRC, and Doug Moffat, for also assisting us when we did experiments in the NRC and also for his Matlab codes. Without his codes, it would have taken me longer learning how to retrieve Raman spectra from CARS spectra.

The staff from Trent University Graduate Studies for helping me get the prestigious Ontario Trillium scholarship and the province of Ontario for supporting me through the Ontario Trillium scholarship. Without their support, going through my Ph. D. would be a lot more challenging.

Edward Stokan for doing exceptional work in copyediting my thesis. It's so much work and thanks so much for doing it for free. Thanks a lot!

Finally, my wife, Timee, for all the love and support, and for making my life so colourful.

Table of Contents

List of Figures

List of Tables

List of Abbreviations

ADR	*anomalous dispersion region.* Also short for anomalous group velocity dispersion region. The *anomalous* dispersion region is one where the index of refraction decreases with increasing frequency of light. This is also the region where the group velocity dispersion is less than zero.
CARS	*coherent anti-Stokes Raman scattering.* A nonlinear Raman scattering process where a pump, probe, and Stokes light are supplied and a higher-frequency *anti-Stokes* light is generated when the energy difference between the pump and Stokes matches a particular vibrational resonance in the sample. In this work the pump and probe light are degenerate (are actually the same light).
CCD	*charge-coupled device.* Multi-element component of a detector used for collecting light, often in spectrometers. Two-dimensional CCD sensors are often used for imaging (i.e. as cameras).

CH/OH	*carbon–hydrogen and oxygen–hydrogen bonds.* Mostly referred to in this thesis as the vibrational frequency region between > 2600 cm^{-1} and < 3600 cm^{-1}.
cm^{-1}	*wavenumber.* A unit of measurement for frequency (or energy) most commonly used in spectroscopy. It is the inverse of the wavelength measured in cm, which is why it is sometimes referred to as a frequency.
CRS	*coherent Raman scattering.* A family of nonlinear Raman scattering processes that include CARS.
CW	*continuous wave.* Typically referred to in the context of non-pulsed laser light. A typical laser pointer is a continuous wave source.
DMSO	*dimethyl sulfoxide;* $(CH_3)_2SO$. A chemical, liquid in room temperature, used in this thesis as a CARS/Raman standard to show vibrational imaging at 2910 cm^{-1}.
KDP	*potassium dihydrogen phosphate.* A crystalline solid used in this thesis as a cheap and available standard for second-harmonic generation.
FWM	*four-wave mixing.*

	Interaction of three light beams in a material resulting in the generation of a fourth beam via third-order nonlinear processes. When the FWM signal is vibrationally resonant, the process is known as CARS. Confusingly, because of its wavelength, the generated signal in FWM is often referred to as *anti-Stokes* despite the fact that no vibrational resonances are involved.
FWHM	*Full width at half maximum.* Describes the width of single-peaked distributions. Commonly used to describe the temporal and/or bandwidth of ultrafast laser pulses.
fs	*femtosecond.* A unit of measurement; 10^{-15} seconds.
GDD	*group delay dispersion.* Related to GVD. The dispersion experienced by a pulse from an optical element at a certain wavelength. GDD equals GVD × the length of an optical element and is measured in units of fs^2.
GVD	*group velocity dispersion.* Related to the rate of change of the index of refraction with wavelength. GVD leads to temporal changes in frequency components of light and is thus directly related to chirp-matching in this thesis.
HWP	*half-wave plate.* An optical element that can control the polarization direction of

	light. Half-wave plates are most commonly used to rotate the angle of linearly polarized light. When followed by a linear polarizer, the pair form a variable light attenuator.
nm	*nanometer.* A unit of measurement; 10^{-9} m.
NA	*numerical aperture.* A measurement of the range of angles in which a system can emit or collect light. In this thesis, the NA relates to the acceptance angle of optical fibres or the tightness of focus of microscope objectives.
NL-1.4-775-945	A non-polarization maintaining fibre having negative group velocity dispersion profile from 775 nm to 945 nm.
NL-PM-750	A polarization maintaining fibre having a negative group velocity dispersion profile from 750 nm to 1260 nm.
NRB	*non-resonant background.* Anti-stokes signals that do not involve the stimulation of molecular vibrations. In the context of CARS spectroscopy/microscopy, vibrationally resonant FWM signals are called CARS signals and background FWM signals arising from exclusively elecronic processes are referred to as NRB. The two processes are indistinguishable by wavelength, but emerge with different phases.

NRC	*National Research Council of Canada.*
OSA	*optical spectrum analyzer.* A fibre-coupled high-resolution spectrometer based on interferometry.
PCF	*photonic crystal fibre.* A microstructured optical fibre containing ordered holes along its length. The fibre length and hole arrangement affects how light propagates through it. Cascaded nonlinear optical processes within PCFs can generate new wavelengths of light, often resulting in emergence of broadband pulses known as supercontinua.
PMT	*photomultiplier tube.* A single-element detector efficient in detecting scant amounts of light.
SF-CARS	*spectral focusing CARS.* A CARS technique that uses broadband “chirp-matched” beams and a single-element detector. Spectral focusing refers to the narrowing of the interaction bandwidth (frequency difference) between two dispersion-engineered broadband pulses.
SHG	*second harmonic generation.* A second-order nonlinear optical process in which the frequency of two photons are parametrically (does not involve energy states) converted to a third photon of twice the original

	frequency. The process only occurs in non-centrosymmetric system and is thus used as a nonlinear microscopy contrast mechanism sensitive to sample structure.
THG	*third harmonic generation.* A third-order nonlinear optical process in which the frequency of three photons are parametrically converted to a fourth photon of triple the original frequency. This is an emerging contrast mechanism in nonlinear microscopy.
TPEF	*two-photon excited fluorescence.* A third-order nonlinear process in which fluorescence results from the simultaneous absorption of two photons. This fluorescence is often the same as from a simple (one-photon) absorption process, but the two-photon excitation mechanism makes the signal intensity dependent (i.e. nonlinear).
USB	*universal serial bus.* A type of hardware connection.
ZDW	*zero dispersion wavelength.* Related to GVD and ADR. The wavelength where the group velocity dispersion curve crosses from positive to negative. In this thesis, the anomalous dispersion regime in a photonic crystal fibre is bounded by “two ZDWs.”

Glossary

anomalous dispersive region Also short for anomalous group velocity dispersion region. It is related to the dispersive property of a material. The wavelength region in which light with higher frequencies move faster than light with lower frequencies. This is also the wavelength region where the group velocity dispersion is less than zero.

anti-Stokes Traditionally, the blue-shifted (higher frequency) scattered light in a Raman process that originates from an excited vibrational state. The CARS signal is of this wavelength and is thus also referred to as anti-Stokes light despite originating from the sample's ground vibrational state. (See Stokes)

astaxanthin An oil-soluble natural carotenoid related to β-carotene that happens to generate strong CARS signals between 1000 cm^{-1}–1600 cm^{-1}.

attenuator A device that controls the intensity of light.

boxCARS A cumbersome technical implementation of CARS spectroscopy that uses non-parallel light beams. The approach is largely unsuitable for microscopy.

broadband Displaying a wide range of frequencies/wavelengths. In this thesis, laser pulses with wavelength spanning several nanometers.

chirp-matching Modifying dispersion of broadband light pulses to match their frequency-time behaviour.

coherent anti-Stokes Raman scattering A nonlinear Raman scattering process where a pump, probe, and Stokes pulse are supplied and a higher-energy *anti-Stokes* signal pulse is generated when the energy difference between the pump and Stokes matches a particular vibrational resonance in the sample. In this work the pump and probe pulses are degenerate (are actually the same pulse)..

coherent Raman scattering A family of nonlinear Raman scattering processes that include CARS.

continuous wave Typically referred to in the context of non-pulsed laser light. A typical laser pointer is a continuous wave source.

cross-phase modulation A contributing factor to *supercontinuum* generation. Shift in the phase of a light pulse due to the presence of another light pulse (requires a nonlinear medium).

degenerate beams Beams of the same color, frequency or energy.

delay line An optical component that controls the arrival time of a light pulse at a specific position. Delay lines are used to synchronize the temporal overlap of ultrashort pulses.

dispersion Related to index of refraction. The separation or stretching of light into its color components.

dispersive wave generation A contributing factor to supercontinuum generation. The dispersion of light in a medium within its anomalous dispersive region that is non-solitonic in nature. Also see *anomalous dispersive region* and *soliton*.

elastic scattering Scattering of photons where the kinetic energy of the system of incoming and outgoing photons are conserved.

excipient Inactive components in a drug that serves as bulking material and facilitates delivery of the active ingredient.

epi-direction Backwards direction with respect to the incoming light. Typically used in reference to microscopy for backwards-collection (as opposed to trasmitted) imaging.

Faraday isolator A device that prevents the reflection of light back into the laser cavity which may interfere with the generation of ultrashort pulses. It is a polarization-based optical diode.

fingerprint frequencies Vibrational frequencies below 1600 cm^{-1}. This vibrational region is filled with unique molecular resonances that can allow for individual chemical identification.

fluorescence Dipole-coupled emission of light from an excited state.

four-wave mixing Interaction of three light beams in a material resulting in the generation of a fourth beam via third-order nonlinear processes. When the four-wave mixing signal is vibrationally resonant, the process is known as CARS. Confusingly, because of its wavelength, the generated signal in four-wave mixing is often referred to as *anti-Stokes* despite the fact that no vibrational resonances are involved.

galvos Short for galvanometers. Scanning mirror assembly used for spatial scanning of light. It is faster than a stage scanner but the resulting image can suffer from lens aberrations.

group delay dispersion Related to *group velocity dispersion*. The dispersion experienced by a pulse from an optical element at a certain wavelength. group delay dispersion equals group velocity dispersion multiplied by the length of an optical element and is measured in units of fs^2.

group velocity dispersion Related to the rate of change of the index of refraction with wavelength. Group velocity dispersion leads to temporal changes in frequency components of light and is thus directly related to chirp-matching in this thesis.

half-wave plate An optical element that can control the polarization direction of light. Half-wave plates are most commonly used to rotate the angle of linearly polarized light. When followed by a linear polarizer, the pair form a variable light attenuator.

hyperspectroscopy Concurrent spectroscopy and imaging. The term usually refers to data stacks with two imaging dimensions and one spectroscopic dimension, irrespective of the density of the spectroscopic information. In this work, hyperspectroscopy usually refers to images with an associated CARS spectrum at each pixel.

immersol An index-matching medium used to enhance spatial resolution in microscopy.

inelastic scattering Scattering of photons where the kinetic energy of the incoming and outgoing photons are not conserved and the sample is either temporarily excited or de-excited.

intra-pulse filtering Separation of spectral components from a light pulse.

Kerr effect Change in the index of refraction caused by intense light. The index of refraction can be modelled as $\Delta n = n_0 \pm n_2 I$, where n_0 is the linear index of refraction, n_2 is the nonlinear index of refraction, and I is the pulse intensity.

long pass filter A filter that transmits longer wavelength light and blocks shorter wavelength light.

maximum entropy method A numerical method to extract Raman-like spectra from CARS spectra. Distinct from *time-domain Kramers-Kronig* based methods.

modulation instability A contributing factor to supercontinuum generation. A perturbation in the propagating wave having frequencies within the anomalous dispersion region that grows in power. (see *anomalous dispersive region*).

multimodal Multiple concurrent imaging techniques. The simultaneous collection of CARS, TPEF, and SHG is referred to as multimodal imaging in this thesis.

multiplex CARS An experimental approach to CARS microscopy that uses a spectrometer to detect the anti-Stokes. Contrasted in this thesis with spectral-focusing CARS (SF-CARS).

narrowband Narrow spectrum of light that typically spans less than a nanometer.

NL-1.4-775-945 A non-polarization maintaining fibre having negative *group velocity dispersion* profile from 775 nm to 945 nm.

NL-PM-750 A polarization maintaining fibre having a negative *group velocity dispersion* profile from 750 nm to 1260 nm.

non-resonant background *Anti-stokes* light that does not involve the stimulation of molecular vibrations. This signal contaminates the CARS signal because it emerges at the same wavelength but with a different phase that interferes with it coherently, altering both the intensity and shape of the CARS spectrum.

numerical aperture A measurement of the range of angles in which a system can emit or collect light.

optical coherence tomography An interferometric microscopy technique used for resolving three-dimensional structure of tissues.

optical spectrum analyzer A fibre-coupled high-resolution spectrometer based on interferometry.

oscillator A pulsed laser source. In this thesis, a titanium-sapphire laser generating nominally 800 nm light.

parametric process An optical process in which there is no net transfer of energy or momentum. *Four-wave mixing* is a parametric process.

peak intensity The maximum instantaneous intensity of light. Note that most detectors are only able to measure the average intensity and not peak intensity.

photomultiplier tube A highly-sensitive single-element light detector.

photonic crystal fibre A microstructured optical fibre containing ordered holes along its length. The fibre length and hole arrangement affects how light propagates through it. Cascaded nonlinear optical processes within fibre can generate new wavelengths of light, often resulting in emergence of *broadband* pulses known as supercontinua.

polymorphs Crystals of the same composition but different structure.

probe A light pulse that can be used to stimulate signal generation, usually arriving subsequent to a *pump* pulse.

pump The primary light source in nonlinear optical processes. In various *four-wave-mixing* processes such as CARS, the pump is provided in conjunction with other pulses (such as the Stokes and probe).

second-harmonic generation A second-order nonlinear optical process in which the frequency of two photons are *parametrically* converted to a third photon of twice the original frequency. The process only occurs in non-centrosymmetric system and is thus used as a nonlinear microscopy contrast mechanism sensitive to sample organization..

self-phase modulation A contributing factor to *supercontinuum* generation. Shift in the phase of a field (light) due to a self-caused Kerr effect.

single-frequency CARS A CARS technique using narrow band lasers and a single-element detector. “Single-frequency” refers to the *narrowband* aspect of the emerging anti-Stokes signal. To obtain a CARS spectrum, the vibrational frequency is scanned by varying the excitation wavelengths.

short pass filter A filter that transmits shorter wavelength light and blocks longer wavelength light.

soliton fission A contributing factor to supercontinuum generation. The splitting of a soliton into smaller pulses due to some perturbation.

spectral focusing CARS A CARS technique that uses broadband “chirp-matched” beams and a single-element detector. Spectral focusing refers to the narrowing of the interaction bandwith between two dispersion-engineered broadband pulses.

spectral surfing A technique invented in this thesis that is used to generate a more useful Stokes supercontinuum for SF-CARS. Spectral surfing refers to the synchronization of power-tuned supercontinuum generation during a CARS frequency scan.

stage scanner A controllable microscope platform moved to build up images. This is contrasted with much faster galvo scanning, but does not suffer from lens aberrations.

soliton Light propagating through a negatively dispersive medium but is not affected by dispersion due to competing Kerr effects. A self-similar propagating pulse.

supercontinuum Broad spectrum of light that typically spans several hundred nanometers and is generated using a photonic crystal fibre.

supercontinuum Stokes or Stokes supercontinuum. In this thesis, broadband light generated by a *photonic crystal fibre* module used as Stokes light in a CARS process.

Stokes The red-shifted light that is generated in a Raman scattering process. In coherent Raman scattering, the Stokes is provided along with the pump stimulate the generation a blue-shifted signal at the anti-Stokes wavelength (see *anti-Stokes*).

tight-focusing Use of a high *numerical aperture* lens to focus light into a small spot. The term is typically used to denote the presence of a wide range of wavevectors within a small volume.

time-domain Kramers-Kronig transform A numerical method used for transforming frequency-domain CARS spectra to Raman-like spectra.

transform-limited A pulse is transform-limited when it is the narrowest it can be temporally for its bandwidth. This is to be contrasted with pulses that have experienced any amount of dispersion. Un-chirped pulses in which all frequencies are temporally overlapped.

two-photon excited fluorescence A third-order nonlinear process in which fluorescence results from the simultaneous absorption of two photons. This fluorescence is often the same as from a simple (one-photon) absorption process, but the two-photon excitation mechanism makes the signal intensity dependent (i.e. nonlinear)..

ultrashort pulse Light that is a few picoseconds or less in duration. This thesis is concerned with pulse durations up to 300 fs.

vibrational resonance Frequency of a vibrational mode, typically measured in units of cm^{-1}.

virtual electronic state The virtual state is a transient state that has no well-defined energy. It serves to mediate a non-linear optical process or the interference of different optical frequencies.

zero dispersion wavelength Related to *group velocity dispersion* and *anomalous dispersive region.* The wavelength where the *group velocity dispersion* curve crosses from positive to negative. In this thesis, the anomalous dispersion regime in a photonic crystal fibre is bounded by “two ZDWs.”

Chapter 1

SF-CARS microscopy: Background

1.1 Raman scattering

This section discusses a basic form of a vibrationally-coupled scattering known as Raman scattering and serves as a preface for the more complex coherent anti-Stokes Raman scattering (CARS).

Raman scattering occurs when light couples with molecular vibrations. The emerging scattered light can have lower or higher energy than the incident light and is called Stokes and anti-Stokes, respectively. The energy difference between the incident and the scattered light corresponds to the frequency of a resonant vibration (Fig. 1.1). Depending on the symmetry of the vibrational mode, a particular vibration may or may not be "Raman active." Even Raman-active modes may not scatter light efficiently, with only about 1 in 10^6 incident photons contributing to the Raman signal. This makes Raman scattering difficult to observe with natural light sources [1], but it is more easily observed with narrow bandwidth, high-intensity lasers [2].

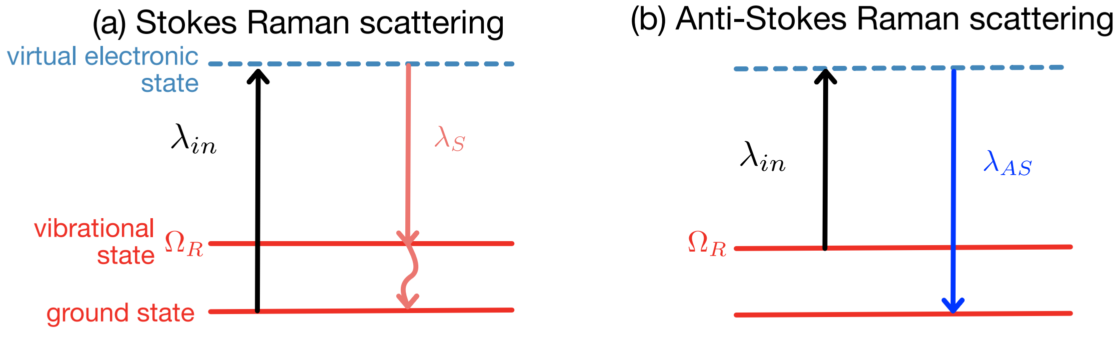

Figure 1.1: Energy diagram representations of Stokes and anti-Stokes Raman scattering. (a) Representation of Stokes Raman scattering. The coupling of photons with the vibrational state of a molecule that is in its ground state causes the emission of a red-shifted Stokes photon having wavelength λ_S. (b) Representation of anti-Stokes Raman scattering. The coupling of photons with a molecule already in its vibrational state causes the emission of a blue-shifted anti-Stokes photon having wavelength λ_{AS}. The energy level of the vibrational state is represented by Ω_R while the *virtual electronic state* is represented by the dashed blue line. The virtual electronic state does not represent a real state of the molecule but rather represents a coupling path towards the Raman process.

Raman scattering occurs as light interact with valence electrons in the molecules which in couple to the atomic nuclei via coulomb forces, thereby driving bond vibrations. This interaction can be modeled using the molecular polarization density, written as [3]

$$P = \epsilon_0 \chi E \tag{1.1}$$

where $\epsilon_0 = 8.854 \times 10^{-12}\ \mathrm{C}^2/\mathrm{N}\cdot\mathrm{m}^2$ is the vacuum permittivity, E is the amplitude of the electric field, and χ is the electric susceptibility which contains information on the coupling of light with the valence electrons and nuclei in the molecule[4]. As we will find in the next section, this (linear) expression for the polarization density (Eq. (1.1)) can be expanded to include terms that are nonlinear with field, and those nonlinear terms lead to *nonlinear optical* processes such as CARS.

Spontaneous Raman scattering is a photonically-inelastic process, which means that the total incoming and outgoing light differ in energy. The scattered photon can either be red-shifted (Stokes) or blue-shifted (anti-Stokes) with respect to the incident photon, depending on whether the vibration is being excited or de-excited. The shift in wavelength can be calculated as

$$\begin{aligned} \frac{1}{\lambda_S} &= \frac{1}{\lambda_P} - \Omega_R && \text{for the Stokes} \\ \frac{1}{\lambda_{AS}} &= \frac{1}{\lambda_P} + \Omega_R && \text{for the anti-Stokes} \end{aligned} \tag{1.2}$$

where λ_S is the Stokes wavelength, λ_{AS} is the anti-Stokes wavelength, λ_P is the incident laser (known as *pump*) wavelength, and Ω_R is the frequency of the vibrational state. Ω_R is commonly measured in wavenumbers (cm^{-1}) and is converted from wavelength (measured in nanometers) using the following equation:

$$\Omega_R = \left[\frac{1}{\lambda_P} - \frac{1}{\lambda_S}\right] \times 10^7 \text{nm/cm} \tag{1.3}$$

As each chemical has its own distinct molecular composition and structure, it also has its own distinct modes of vibration and unique set of vibrational energies. This makes Raman scattering a powerful tool for determining the chemical composition of materials and has been established as a gold standard in chemical analysis [2]. As an example, Fig. 1.2 demonstrates the consistency with which Raman spectroscopy identifies vibrational frequencies. The figure shows the comparison Raman spectra of benzonitrile obtained using a neighboring lab's Raman microscope (Vreugdenhil lab) and from an online reference [5], respectively. Note that the two different experimental implementations reproduce the vibrational landscape at the same frequencies, but

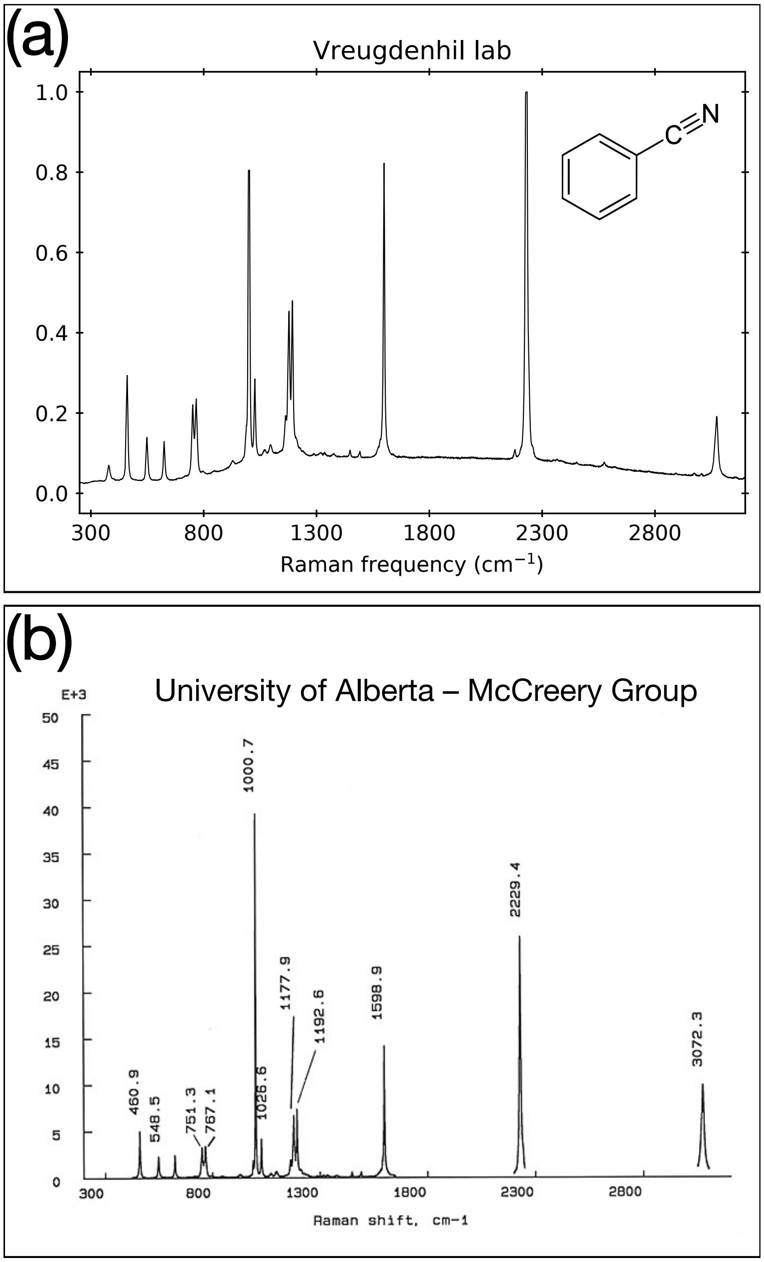

Figure 1.2: Raman spectra of Benzonitrile. (a) Raman spectrum taken from a neighboring lab (Vreugdenhil lab) with unprocessed background fluorescence. Inset shows the chemical structure of benzonitrile. (b) Raman spectrum taken from an online reference [5] with fluorescence background removed, as reflected by the flat baseline.

that both the ratios of the peaks and (fluorescence) background signals differ such that the two spectra are not identical.

1.1.1 Spectral regions of vibrational resonances

By convention, the Raman spectrum is divided into three distinct regions: the CH/OH vibrational region, the silent region, and the fingerprint region. The CH-stretch modes typically present between 2700 cm^{-1} and 3000 cm^{-1}, and various OH-stretch modes present between 3100 cm^{-1} and 3650 cm^{-1}, and thus the range of 2700 cm^{-1}–4000 cm^{-1} is collectively referred to as the CH/OH region. A Raman spectrum of a chemical showing peaks in this region strongly indicates the presence of such bonds, but since these are so common in most organic compounds, and the resonances are relatively broad and indistinguishable, the spectrum might not give detailed information about the chemical structure. The frequency region between 1600 cm^{-1} and 2600 cm^{-1} is called the silent region. Only a few relatively-rare bond arrangements show vibrational resonances in this region. A key exception is the carbon-nitrogen triple bond, which as a very strong stretching resonance near 2200 cm^{-1}. Conversely, the most informative region in a Raman spectrum is the fingerprint region below 1600 cm^{-1}. This region is particularly important when identifying the composition of chemical compounds.[1] Chemical compounds are composed of sets of molecules which have a larger collective mass than the smaller CH and OH molecules, and therefore, these sets of molecules have lower vibrational frequencies (e.g., benzene C_6H_6 is found in benzonitrile and has numerous observable vibrational resonances below 1600 cm^{-1}).

---

[1] Different literature may report different frequency ranges for the fingerprint, silent, and CH/OH regions. The primary point of the ranges discussed here is to give the reader some sense of the importance and spectral extent of these regions.

1.2 Nonlinear optics

With progress in laser technology, the peak pulse powers of lasers have reached several GW [6]. The intense electric fields produced by such lasers move electrons beyond their linear response. In that case, the polarization density can be expanded to include nonlinear terms as follows [3]:

$$P = \epsilon_0 \big(\chi^{(1)} E + \chi^{(2)} E^2 + \chi^{(3)} E^3 + ...\big) \tag{1.4}$$

where $\chi^{(n)}$ is the nth-order susceptibility. Raman scattering follows $\chi^{(1)}$ while nonlinear optical processes depend on higher-order susceptibilities such as $\chi^{(2)}$, $\chi^{(3)}$, and so on. The values of these higher-order susceptibilities are much smaller than $\chi^{(1)}$, and thus nonlinear optical processes often require lasers capable of generating intense pulses—orders of magnitude stronger than what is needed to observe Raman scattering.

Figure 1.3 shows the energy diagram representations of some second- ($\chi^{(2)}$) and third-order ($\chi^{(3)}$) nonlinear optical processes. Similar to Raman scattering, both second- and third-order nonlinear processes can be used to study the structure and composition of materials. Examples of second-order nonlinear processes are second-harmonic generation (SHG), sum-frequency generation (SFG), and difference-frequency generation (DFG), while examples of third-order processes are two-photon excited fluorescence (TPEF), third harmonic generation (THG), and coherent anti-Stokes Raman scattering (CARS). Third-order nonlinear processes involve the “mixing” of four-beams and are referred to as “four-wave mixing” (FWM) in literature [7]. In this thesis I mainly focus on the CARS process, but mention SHG and TPEF

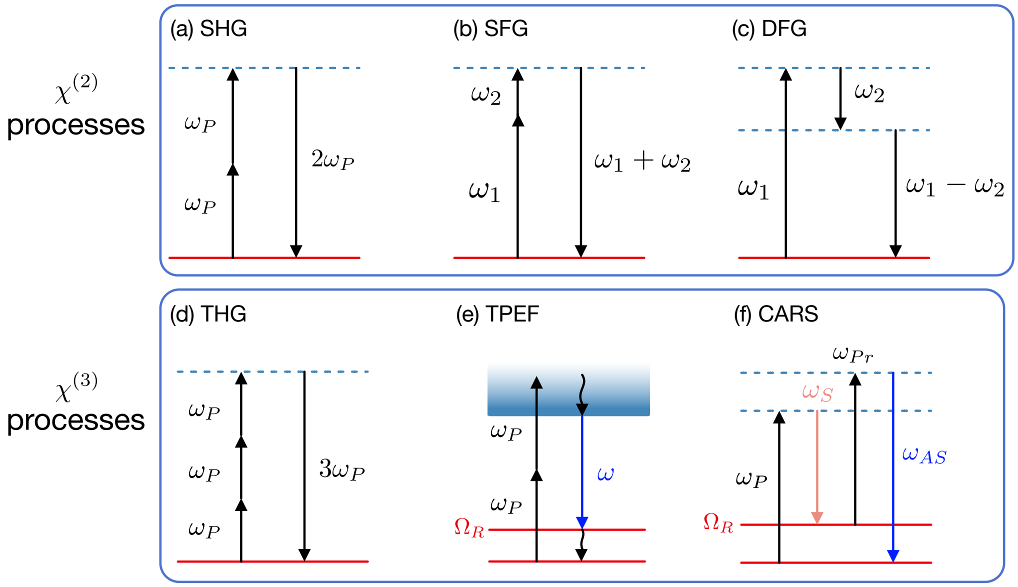

Figure 1.3: Energy diagram representations of several second- and third-order nonlinear optical processes. In these diagrams, the bottom red lines represent the ground state while the dashed blue lines represent virtual electronic states. The second red lines represent vibrational states of energy Ω_R. (a) Second-harmonic generation. Two photons with equal frequencies interact resulting in the scattering of a photon with twice the original frequency. Experimentally, ω_P is provided by a single beam and signal at $2\omega_P$ is detected. (b) Sum-frequency generation. Two photons with different frequencies interact resulting in the scattering of a photon with a frequency that is the sum of the incident photons. Experimentally, ω_1 and ω_2 are provided, and signal at the sum frequency is detected. (c) Difference-frequency generation. Two photons with different frequencies interact resulting in the scattering of a photon with a frequency that is the difference of the incident photons. Experimentally, ω_1 and ω_2 are provided, and signal at the difference frequency is detected. (d) Third-harmonic generation. Three photons of equal frequencies interact resulting in the scattering of a photon with thrice the original frequency. Experimentally, ω_P is provided by a single beam, and signal at $3\omega_P$ is detected. (e) Two-photon excited fluorescence. Two photons are simultaneously absorbed to excite electrons into an excited state, resulting in emission of lower-energy light upon de-excitation (ω, blue arrow). As with typical fluorescence processes, intermediate non-radiative decay steps are also possible (wiggly arrows). (f) Coherent anti-Stokes Raman scattering. Two incident photons with frequencies, ω_P and ω_S, drive a vibrational resonance. A probe photon with frequency, ω_{Pr}, allows the scattering of an anti-Stokes photon with frequency, ω_{AS}. Experimentally, two beams are supplied (ω_P and ω_S), and a higher energy signal is detected (ω_{AS}).

as additional techniques that provide complementary (and concurrent) information in a *multimodal* nonlinear microscopy system.

1.3 Spontaneous vs. coherent Raman scattering

The weak signals of traditional spontaneous Raman scattering mean that producing spatial chemical maps can take hours to achieve [8]. Thus, Raman “microscopy” is relatively rare, and when implemented, typically provides sparse spatial sampling. Nonlinear approaches to Raman scattering can boost signals by orders of magnitude, and are thus much more suitable for microscopy applications. Such techniques, which include CARS, are collectively known as coherent Raman scattering (CRS). CRS differs from spontaneous Raman scattering with regards to excitation and signal generation. Spontaneous Raman scattering is typically implemented using relatively-weak continuous wave (CW) lasers. With this kind of excitation, the molecules do not necessarily vibrate in-phase, and this results in the incoherent generation of radiation. On the other hand, CRS is implemented using ultrafast pulsed lasers that can generate intense (10^6 times stronger than CW lasers) and short pulses (lasting less than a few picoseconds). Pulses generated by ultrafast lasers have an increased chance of multiphoton interaction. When two photons interact having a frequency difference equal to a molecular vibrational frequency, Ω_R, the photons drive that molecular vibration. And because the excitation occurs in such a short amount of time, molecules coherently vibrate in-phase. A third photon then probes this coherence and stimulates signal generation such as the anti-Stokes in CARS. The coherence of the generated anti-Stokes signal matters for the constructive addition of signals over the excitation volume. For sample layers that are thick on the order of the several excitation wavelengths, the CARS signal can destructively interfere in the backward (or "epi-") direction, and mostly be generated in the forward direction. Thus the *coherence* in CRS relates to signal propagation and not necessarily to a phase relation between the excitation pulses [9, 10].

There are several advantages of CRS over spontaneous Raman scattering. Due to the coherent generation of radiation, signal intensities can be as much as 100 times greater than spontaneous Raman scattering [11]. Furthermore, the dwell time of a laser on a particular spot can be as short as a few nanoseconds [12, 13] to a few microseconds [14, 15]. Because of fast signal acquisition, some groups have demonstrated high-speed, video-rate imaging by tuning laser frequencies to drive a single vibrational resonance [12, 13]. In comparison, spontaneous Raman scattering has laser dwell times on the order of milliseconds [16], and because the entire spectrum is collected at each spot, imaging can take minutes to hours to finish [8].

Disadvantages of CRS over spontaneous Raman scattering are mainly its implementation complexity and cost. CRS requires a more complex optical setup since it requires at least two intense light sources. Beams need to be overlapped both in space and in time to allow the photons to interact, thus requiring the addition of delay lines and alignment optics. Furthermore, ultrafast lasers cost at least an order of magnitude more than CW lasers.

1.4 Coherent anti-Stokes Raman scattering microscopy

CARS is simpler to implement than other CRS techniques. Detecting the vibrational signal typically requires three excitation beams—the pump, probe, and Stokes. In CARS, the pump and probe can be degenerate (the same beam). Using degenerate pump and probe beams brings down the cost of a CARS system since a third laser source is no longer needed. This also simplifies beam alignment since we only need to align two beams. Furthermore, the vibrational signals are detected at the anti-Stokes wavelength which is shorter (higher frequency) than the wavelength of the excitation beams. A simple *short-pass filter* can be used to separate the shorter wavelength anti-Stokes from the longer wavelength excitation beams. Lastly, with most laser sources operating in the visible to the near infrared range (500 nm – 1300 nm), CARS signals can be generated at wavelengths (< 900 nm) for which sensitive detectors are widely available.

1.4.1 Brief theory of CARS

Since Raman scattering provides a gold standard for chemical identification, it is inevitable to compare Raman spectra with CARS spectra. Both Raman and CARS show similarities in spectra, but under certain conditions–such as low chemical concentrations or the use of a *broadband* laser–CARS spectra can differ significantly from Raman spectra. CARS peak locations can be several wavenumbers off from its Raman counterpart, and CARS peak intensities may not reflect Raman peak intensities.

To understand the mechanics behind CARS, especially its spectrum, I highlight some theoretical considerations for the technique in this section.

As a third-order nonlinear process, the CARS (i.e. anti-Stokes) field can be written as

$$E_{AS}(\omega_{AS}) = \chi^{(3)} E_P(\omega_P) E_S^*(\omega_S) E_{Pr}(\omega_{Pr}) \tag{1.5}$$

where E_P, E_S, and E_{Pr} are the pump, Stokes and probe fields, respectively; ω_P, ω_S, and ω_{Pr} are their respective frequencies; * denotes the complex conjugate. The corresponding phase[2] and energy matching conditions for the CARS process are

$$\overrightarrow{k_{AS}} = \overrightarrow{k_P} + \overrightarrow{k_{Pr}} - \overrightarrow{k_S} \tag{1.6}$$

$$\omega_{AS} = \omega_P + \omega_{Pr} - \omega_S \tag{1.7}$$

where $\overrightarrow{k}$ represents the wavevector.

In the implementation of a degenerate CARS system, i.e. $\omega_P = \omega_{Pr}$, Eq. (1.5) can be written as

$$E_{AS}(\omega_{AS}) = \chi^{(3)} E_P^2(\omega_P) E_S^*(\omega_S) \tag{1.8}$$

with the corresponding CARS intensity of

$$I_{AS}(\omega_{AS}) \propto |\chi^{(3)}|^2 I_P^2(\omega_P) I_S^*(\omega_S) \tag{1.9}$$

---

[2] The mathematical description of a propagating wave uses both energy and momentum terms in the phase, yet it has become common to refer to the spatial propagation terms (i.e. momentum) as the "phase." Thus, "phase matching" in optics is synonymous with momentum conservation.

The susceptibility is modeled using the following equation [17]:

$$\chi^{(3)} = \chi_R(\Delta) + \chi_{NR} \tag{1.10}$$

where χ_R and χ_{NR} are the vibrationally resonant and non-resonant parts of the susceptibility, and $\Delta = \omega_P - \omega_S$. The resonant part of the susceptibility follows a model based on damped molecular harmonic oscillators and can be written as [18]:

$$\chi_R(\omega_P - \omega_S) = \frac{A}{\Omega_R - (\omega_P - \omega_S) - i\Gamma_R} \tag{1.11}$$

Thus Eq. (1.10) can be written as

$$\chi^{(3)} = \frac{A}{\Omega_R - (\omega_P - \omega_S) - i\Gamma_R} + \chi_{NR} \tag{1.12}$$

where A is the amplitude, Ω_R is the vibrational energy, and Γ_R is the half-width (at half-maximum) of the Rth vibrational state. The so-called non-resonant term is electronically coupled and ever-present, but is not resonant with either a vibrational or an electronic transition. Figure 1.4 shows the energy diagram representation of both resonant (through χ_R) and non-resonant (through χ_{NR}) FWM. Since CARS is essentially a FWM process, the CARS signal always includes contributions from the non-resonant susceptibility.

By combining Eqs. (1.9) and (1.10), the CARS intensity can now be written as

$$I_{AS}(\omega_{AS}) = \Big[|\chi_R|^2 + |\chi_{NR}|^2 + 2\chi_{NR}Re(\chi_R)\Big] I_P^2(\omega) I_S^2(\omega) \tag{1.13}$$

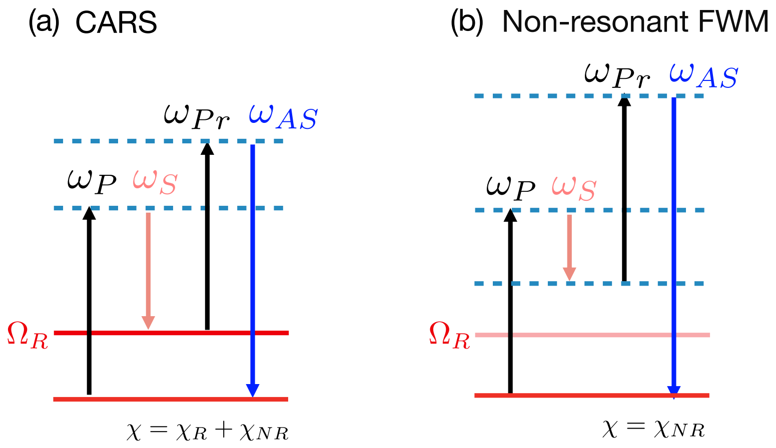

Figure 1.4: Resonant and non-resonant FWM in CARS. (a) Energy diagram for both the resonant (i.e. CARS) and non-resonant FWM (i.e. NRB) processes. The mixing of the pump (ω_P, black) and Stokes (ω_S, red) beams stimulate a vibrational resonance allowing the probe beam (ω_{Pr}, black) to generate a strong anti-Stokes (ω_{AS}, blue). (b) Energy diagram for the non-resonant FWM only process. The mixing of the pump and Stokes beams in a non-resonant condition leads to the generation of a weak anti-Stokes.

A plot of Eq. (1.13), with consideration of the susceptibility relation given by Eq. (1.12), shows a CARS spectrum that follows a so-called dispersive line shape as shown in Fig. 1.5—a feature frequently observed in CARS experiments. The first term of eq. (1.13), $|\chi_R|^2$, reflects the Raman response. The second term, $|\chi_{NR}|^2$, can be assumed constant and independent of frequency [19] and serves as an offset to the signal baseline. The third term, $2\chi_{NR}Re(\chi_R)$, is a mixing contribution from both resonant and non-resonant signals that results in the dispersive line shape of the CARS spectrum.

The simulation of the anti-Stokes intensity in Fig. 1.5, however, rarely represents an actual CARS spectrum. Real experimental CARS spectra most often include additional spectral complexities—arising from low chemical concentrations, the spectral lineshape, and noise in the excitation beams. With low chemical concentrations, the

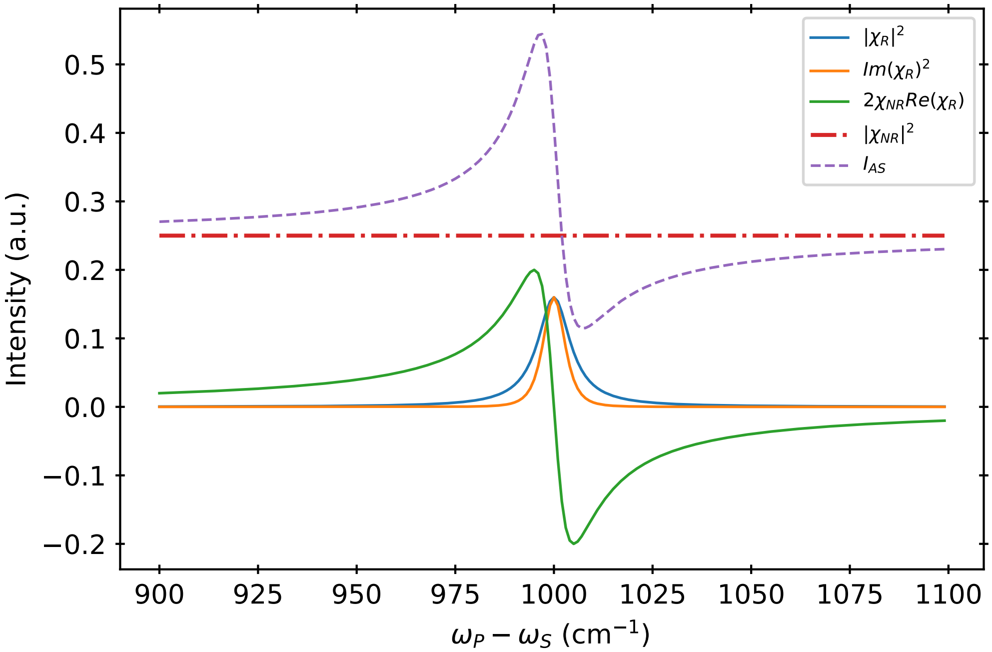

Figure 1.5: A plot of a CARS spectrum and its constituents. The vibrational resonance is set to 1000 cm^{-1}. χ_{NR} is set to 0.5, A is set to 2, Γ_R is set to 5, while both I_P and I_S are set to 1. Note how the nonresonant background mixing term leads to a dispersive lineshape for the anti-Stokes signal with a slightly blue-shifted peak frequency.

ratio χ_{NR}/χ_R will be larger. This is because both the target molecules and the sample matrix generate the non-resonant FWM signal, but only the target molecules will generate the resonant CARS signal. Figure 1.6 shows simulated CARS spectra with different values of χ_{NR} and a frequency-dependent Stokes with broad peaks centred at 1300 cm^{-1} and 2500 cm^{-1}. The anti-Stokes spectrum reflects the convolution of $I_P(\omega_P)^2$ and $I_S(\omega_S)$ in the frequency domain. Experimentally, neither the pump nor the Stokes beam is spectrally flat, thus resulting in further undesired distortions in the CARS spectrum. Because of these distortions, CARS peak locations vary

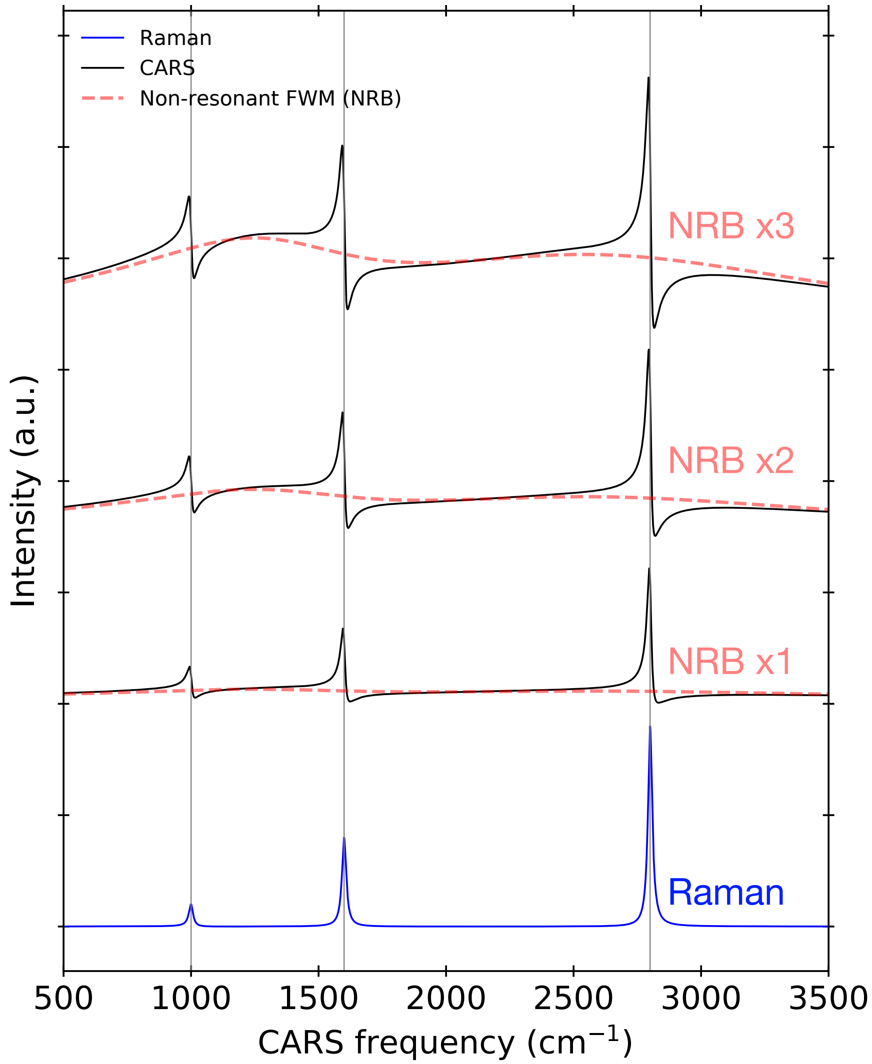

Figure 1.6: A simulated Raman spectrum and various CARS spectra that arise from increasing contribution of the nonresonant background. The resonances are set to 1000 cm^{-1}, 1600 cm^{-1} and 2800 cm^{-1}. The Stokes peaks are set to 1300 cm^{-1} and 2500 cm^{-1}. The pump and Stokes contributions for each plot are the same. From bottom to top the non-resonant susceptibility, χ_{NR}, is set by increasing order from 1×, 2×, and 3×. A simulated Raman spectrum (blue) is shown for reference. Gray vertical lines serve as a guide to show the growing deviation of the CARS peak from the true resonant frequency (i.e. Raman peak) with increasing NRB contribution.

from instrument to instrument and from sample to sample. Therefore, standardizing CARS data for chemical identification becomes a challenging task. Fortunately, CARS spectra contain buried Raman information via χ_R. Methods, such as the *maximum entropy method* [20] and *time-domain Kramers-Kronig* transform [21, 22], have been developed to extract χ_R and have shown a considerable degree of success.

1.4.2 The first CARS microscope

The first reported CARS microscope system, developed by Duncan *et al.* in 1982 [23], used a complicated non-collinear geometry to satisfy CARS phase-matching conditions (Fig. 1.7(a)). This so-called boxCARS geometry is technically challenging to implement. Probing a different vibrational frequency requires a different phase-matching condition and, consequently, a different geometry. This difficult implementation, coupled with a complicated and expensive microscopy and optics system, limited the use of CARS microscopy.

1.4.3 CARS with tightly-focused beams

In 1999, a simple and effective implementation of CARS microscopy was reported by Zumbusch *et al.* [24] by using high *numerical aperture* (NA) objectives to focus the excitation beams (Fig. 1.7(b)). The high NA allowed beams to come from a wide range of angles to (serendipitously) satisfy phase-matching conditions. While the approach sacrifices efficiency of signal generation, CARS images were acquired with ease and laser powers were significantly reduced down to a hundred μW. In comparison, Duncan *et al.* used excitation powers in the order of a hundred mW [23]. Since the use of high NA lenses in CARS microscopy, there have been significant

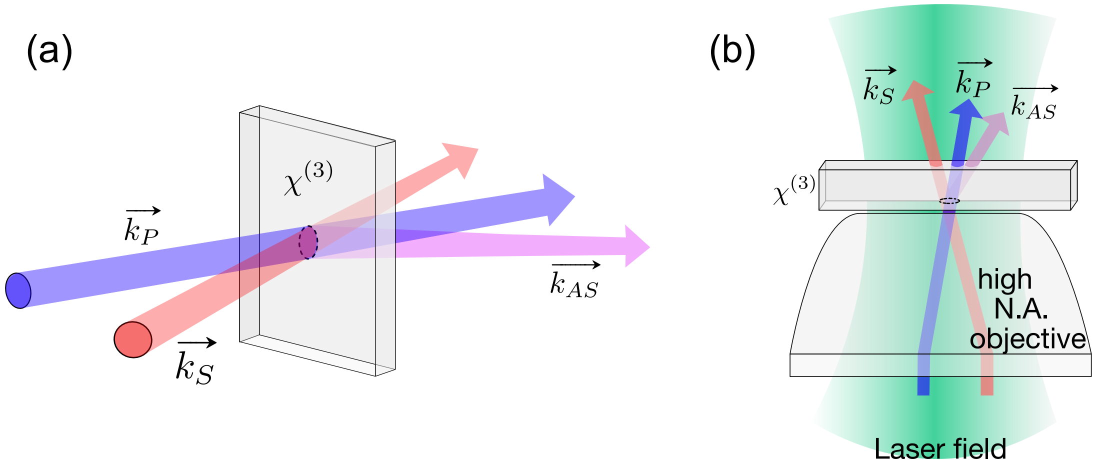

Figure 1.7: CARS microscopy geometry. (a) BoxCARS geometry. Pump (blue) and Stokes (red) beams are non-collinear and incident on the sample with nonlinear susceptibility $\chi^{(3)}$ at an angle that satisfies the phase-matching condition for four-wave mixing. The anti-Stokes (pink) is generated at a different exit angle than the pump and Stokes beams. The pump and Stokes beams can be filtered out spatially or spectrally with a color-filter. (b) Tight-focusing geometry. Collinear pump and Stokes beams (green gradient) enter a high NA objective. The beams are tightly focused allowing multiple phase-matching conditions to be satisfied.

developments in the field where video-rate imaging [13], live-cell imaging [25–27], drug particle tracking [28], and potential applications to medicine [29] have been demonstrated.

1.4.4 Multiplex, single-frequency, and spectral-focusing CARS

There are a number of experimental approaches for implementing CARS microscopy, including *multiplex* CARS[30, 31], *single-frequency* CARS [25], *spectral-focusing* CARS [32, 33], heterodyne CARS [34], polarization CARS [35], frequency-comb CARS [36], and others [37–40]. There are advantages and disadvantages of each, but for this thesis, I concentrate on spectral-focusing CARS with brief mentions of multiplex and single-frequency CARS.

Multiplex and single-frequency CARS operate in stark contrast to each other while spectral-focusing CARS can be considered as a combination of the two. In general, we can categorize the experimental implementation of CARS by two distinct methods of detection: spectral detection and imaging.

Spectral detection is best represented by multiplex CARS. In multiplex CARS, one or both of the pump/probe and Stokes beams are spectrally broad and a wide range of vibrational resonances are probed simultaneously (Fig. 1.8(a,d)). Anti-Stokes light is detected with a spectrometer and the *hyperspectral* images (data containing both spectral and spatial information) are composed one pixel-spectrum at a time using a microscope *stage scanner*. Multiplex CARS can thus be thought of as a “spectrum-first” approach, where rapid collection of good-quality and dense CARS spectra is

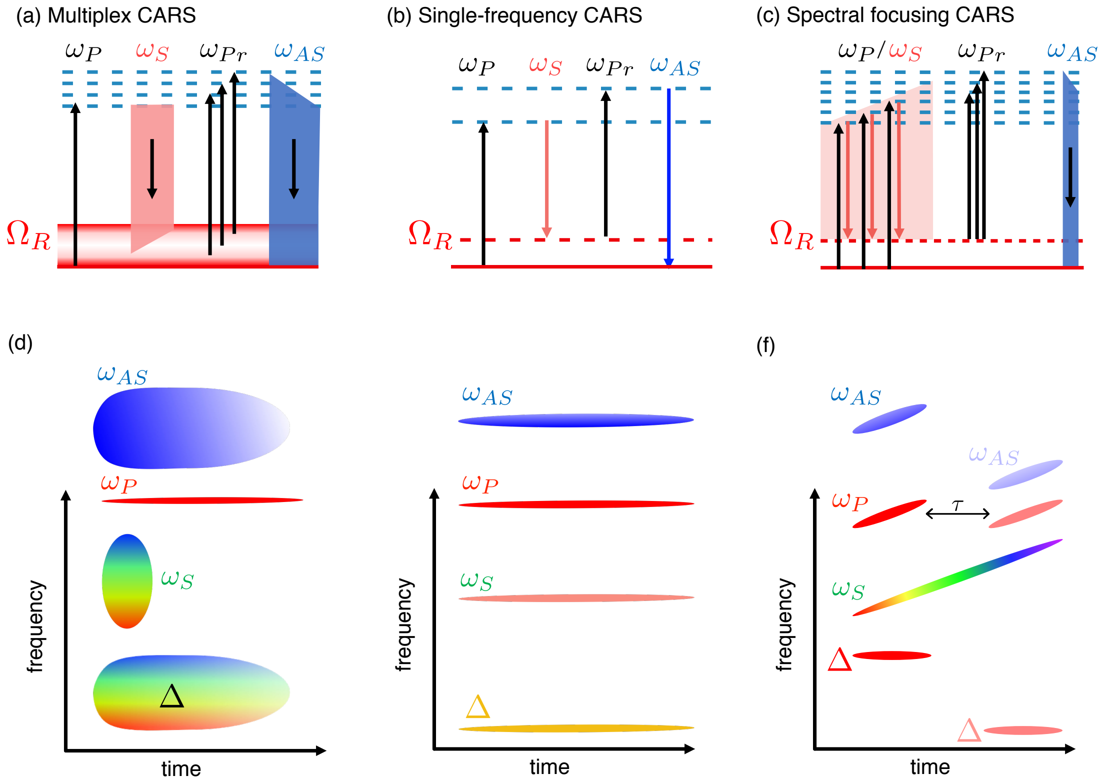

Figure 1.8: Multiplex, single-frequency and spectral focusing CARS. (a) Energy diagram representation of a form of multiplex CARS that uses a narrowband pump, ω_P, and broadband Stokes, ω_S, to stimulate multiple vibrational states, Ω_R (gradient red line). A narrowband probe (ω_{Pr}) up-converts the generation of the anti-Stokes spectrum, ω_{AS}, and is detected by a spectrometer. (b) Energy diagram representation of a single-frequency CARS system using a degenerate narrowband pump, which also acts as the probe, and a narrowband Stokes stimulating a single vibrational state. The anti-Stokes is detected by a single element detector such as a photomultiplier tube. The CARS spectrum is scanned by varying either the pump or Stokes wavelengths. (c) Energy diagram representation of SF-CARS using a supercontinuum Stokes. A narrowband pump is overlapped with a portion of the supercontinuum Stokes (red, transparent) wherein the frequency difference corresponds to a single vibrational resonance made possible through *chirp-matching*. The degenerate pump is used as a probe to generate a spectrally broad anti-Stokes, and is detected by a single element detector. The CARS spectrum is scanned by sweeping the overlap, τ, of the pump and Stokes pulses. (d)-(f) Corresponding spectral frequency vs. time plots of CARS techniques (a)-(c), respectively. Δ represents the difference frequency, $\omega_P - \omega_S$, of the pump and Stokes pulses which encompasses one or more vibrational states.

a dominant attribute. Multiplex CARS spectra can be acquired in a few ms [19]. However, dense image acquisition can take several minutes to hours.

On the other hand, CARS imaging is best represented by single-frequency CARS, which works by using narrowband (usually less than 1 nm in bandwidth) pump and Stokes beams. The excitation beams probe a single vibrational resonance resulting in the generation of a similarly narrowband anti-Stokes beam (Fig. 1.8(b,e)). A single-element detector, such as a photomultiplier tube (PMT), is used to detect the anti-Stokes while beam scanning with high-speed *galvo* scanning mirrors is used to obtain spatial information rapidly. Experimental setups of single-frequency CARS traditionally used synchronized picosecond pulses to stimulate the vibrational resonances, and the CARS spectrum is scanned by tuning the wavelength of one of laser sources. Single-frequency CARS can thus be thought of as an "imaging-first" technique, where rapid—even video rate [13]—image acquisition can enable live-cell imaging. However, due to the limited speed of wavelength control in current laser systems, the hyperspectral data generated in single-frequency CARS can be a sparse and time-consuming process.[3]

A hybrid technique that uses a single-element detector and is capable of rapidly scanning a broad range of vibrational frequencies is spectral-focusing CARS (SF-CARS). SF-CARS works by matching the frequency vs. time dependence of broadband pump and Stokes beams thereby spectrally focusing their frequency differences

---

[3] Most modern laser systems are capable of wavelength tuning at speeds of approximately 5 s per wavelength. Using it to acquire a CARS spectrum with a frequency span of 3000 cm^{-1} and resolution of 5 cm^{-1} increments will take 50 minutes. By comparison, as discussed next, our spectral-focusing-based system can acquire a CARS spectrum with a 3000 cm^{-1} span and 3.3 cm^{-1} resolution increments in 100 s; multiplex CARS systems can acquire a similarly broad CARS spectrum in 2.5 ms [18]. Furthermore, it is typical for single-frequency CARS systems to use synchronized standalone dual-laser systems, thus making it one of the more expensive CARS microscopy setups.

to stimulate a single vibrational resonance (Fig. 1.8(c,f)). This results in the generation of a spectrally broad anti-Stokes (as in multiplex CARS) but representing a narrow vibrational frequency (as in single-frequency CARS). The CARS spectrum is scanned by adjusting the temporal overlap of the pump and Stokes beams through a mechanical delay stage—which is significantly faster than tuning the laser wavelengths. Similar to single-frequency CARS, beam scanning is used to obtain spatial information rapidly. SF-CARS is predominantly an imaging-first technique, where the hyperspectral data can be scanned as quickly as a few seconds up to several minutes depending on the desired spatial and spectral quality.

1.4.5 Chirp-matching

To understand the concept of chirp, we model the ultrashort pulse using a Gaussian field where we write the field as [41]

$$E(t) \propto E_0 e^{-\alpha t^2} e^{i(\omega t + \beta t^2)} \tag{1.14}$$

where E_0 is the amplitude of the electric field, α is a parameter that represents the temporal width of the field,[4] ω is the frequency, and β is known as the linear chirp parameter (or the frequency-time slope of the pulses as shown in Fig. 1.8(f) and can be written in units of cm^{-1}/fs).

Chirp-matching the pump and Stokes pulses is essential for the implementation of SF-CARS. Without chirp-matching and if the pump and Stokes pulses remain undispersed, a broad range of vibrational states will be probed simultaneously. The use of a single-element detector—one of the robust features of SF-CARS—will not be

---

[4] In terms of FWHM, $\alpha = \frac{4ln2}{\mathrm{FWHM}^2}$.

able to distinguish among these multiple vibrational states. Therefore, performing reliable SF-CARS spectroscopy without chirp-matching becomes a challenge. In this case, a spectrometer is better used in this type of CARS system, which essentially converts to multiplex CARS.

Chirp-matched pulses are generated by passing the pulses through a dispersive medium. Pulses propagating through a medium with normal dispersion, i.e., positive *group velocity dispersion* (GVD),[5] are stretched out and experience "positive chirping"; low frequencies lead while high frequencies trail the pulse as demonstrated in Fig. 1.8(f) (note that the horizontal axis is time, not space). By contrast, pulses propagating in a medium with negative dispersion experience negative chirping; high frequencies lead while low frequencies trail the pulse.[6]

In SF-CARS, the pump and Stokes pulses are chirp-matched, meaning the chirp parameter, β, at some or all wavelengths are purposefully engineered to be equal. A good approximation for chirp-matching pulses is through matching the *group delay dispersion* (GDD)[7] of the pulses at a desired wavelength [32, 33, 41–43]. This can be done by introducing highly dispersive elements—such as glass blocks, prisms, or gratings–in the paths of the beams [33]. Ideally, this results in pulses having identical frequency-time slopes similar to Fig. 1.8(f) with a narrow frequency difference, $\Delta = \omega_P - \omega_S$. The better the chirp-match, the narrower the bandwidth of the frequency difference, which means better spectral resolution for SF-CARS spectroscopy. A

---

[5] In terms of the index of refraction, n, frequency, ω, and the speed of light, c, the GVD can be written as GVD $= \frac{2}{c}\frac{\partial n}{\partial \omega} + \frac{\omega}{c}\frac{\partial^2 n}{\partial \omega^2}$. When the derivative of the GVD with respect to frequency is small, the chirp is said to be linear.

[6] see Appendix A for more details on group velocity dispersion, normal, and anomalous dispersion.

[7] GDD is equal to GVD × length of optical element and is measured in units of fs^2.

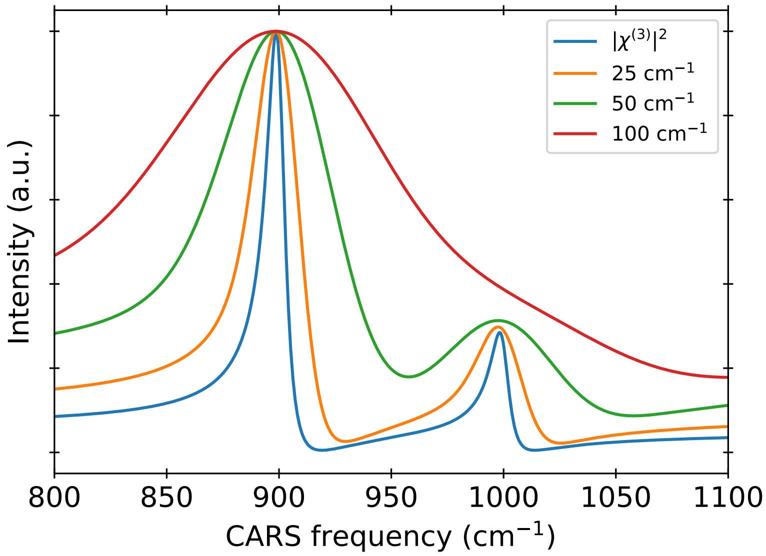

Figure 1.9: Simulation of spectral resolution in CARS spectroscopy. Two vibrational resonances are probed with a hypothetical system with varying capacities of spectral resolutions: 25 cm^{-1}, 50 cm^{-1}, and 100 cm^{-1}, measured as full width at half maximum (FWHM). The vibrational resonances are located at 900 cm^{-1} and 1000 cm^{-1}, have half-widths, Γ_R, of 5 cm^{-1}, and have $|\chi_R/\chi_{NR}|$ ratios of 0.2 and 0.1, respectively. The modulus-square of the susceptibility is also shown for reference.

better spectral resolution allows easy identification of vibrational resonances that are close to each other as illustrated in Fig. 1.9.

1.5 Supercontinuum-generating fibres

Our CARS microscope uses a photonic crystal fibre module for generating a supercontinuum for the Stokes beam. Supercontinuum-generating-fibres are wavelength-broadening devices that act as inexpensive alternative to standalone lasers systems.

Supercontinuum generation is achieved by focusing an intense, ultrashort pulse inside the supercontinuum generating fibre. When the pulses are focused to a few microns in diameter, they can reach powers as high as several GW/cm^2. As the pulse propagates through the fibre, spectral broadening occurs through a cascade of nonlinear processes such as *self-phase modulation*, *cross-phase modulation*, *four-wave mixing*, *modulation instability*, *soliton fission*, dispersive wave generation, and even Raman scattering itself [44]. The contribution of each nonlinear process to spectral broadening varies depending on the parameters of the input pulse. With weaker pulses, *Kerr effect*-based processes such as self-phase and cross-phase modulation become dominant [3, 41]. Figure 1.10(a,b) shows experimental and simulated results of supercontinuum generated by the photonic crystal fibre (PCF) of greatest interest to this work. This fibre has been commercialized by NKT Photonics as a 12-cm module called the FemtoWHITE CARS (Fig. 1.11) and will be the primary fibre discussed throughout this thesis.

The nonlinear Schrödinger equation has been used as a popular tool for understanding the spectral behavior of the supercontinuum in PCFs [44, 45]. A simple, but qualitative, method to determine the spectral behavior of the supercontinuum is

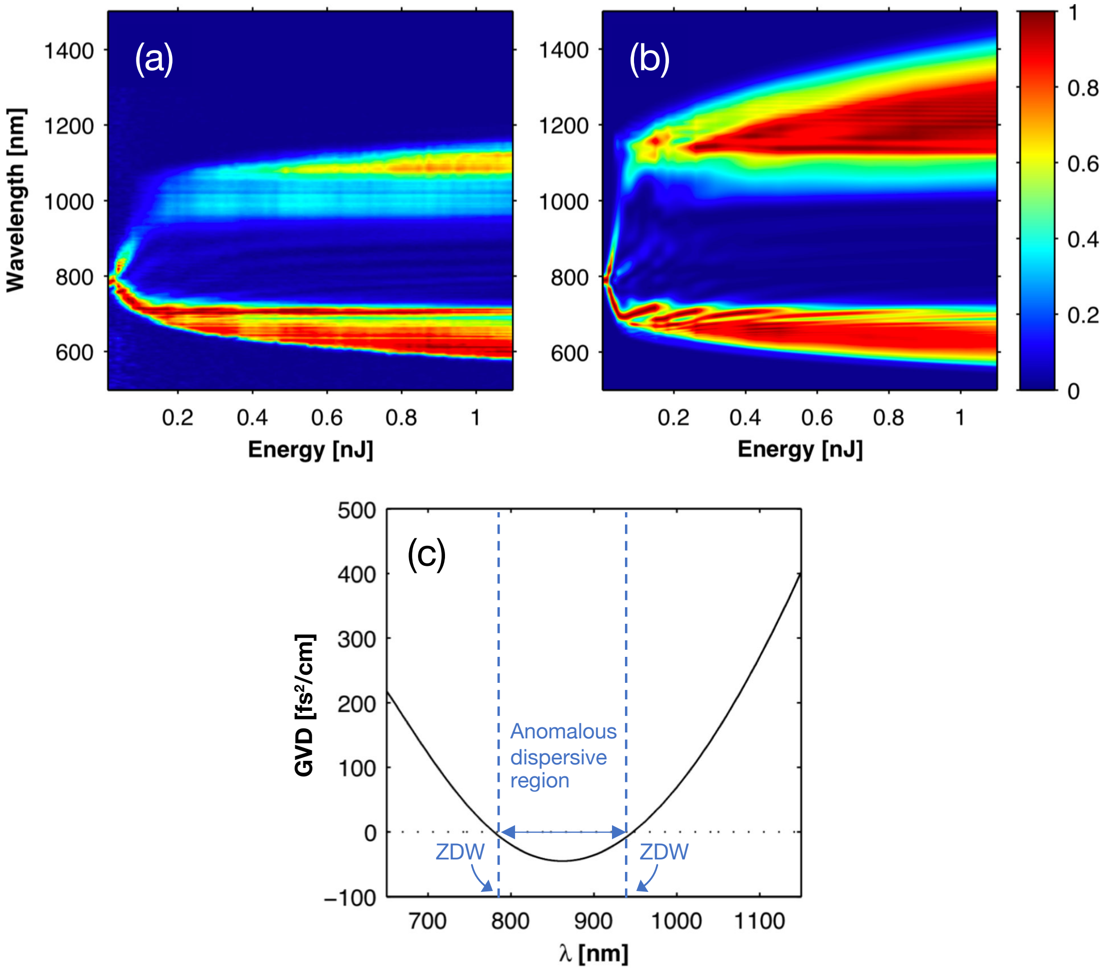

Figure 1.10: Supercontinuum generation in a photonic crystal fibre. (a) Experimental measurement of output spectra versus input pulse energy for a 40 fs *transform-limited* input pulse centred at 790 nm. (b) Theoretical simulation of the spectral evolution. (c) Dispersion properties of the photonic crystal fibre with zero dispersion wavelengths at 780 nm and 945 nm. Figure and caption modified and adapted from ref [45].

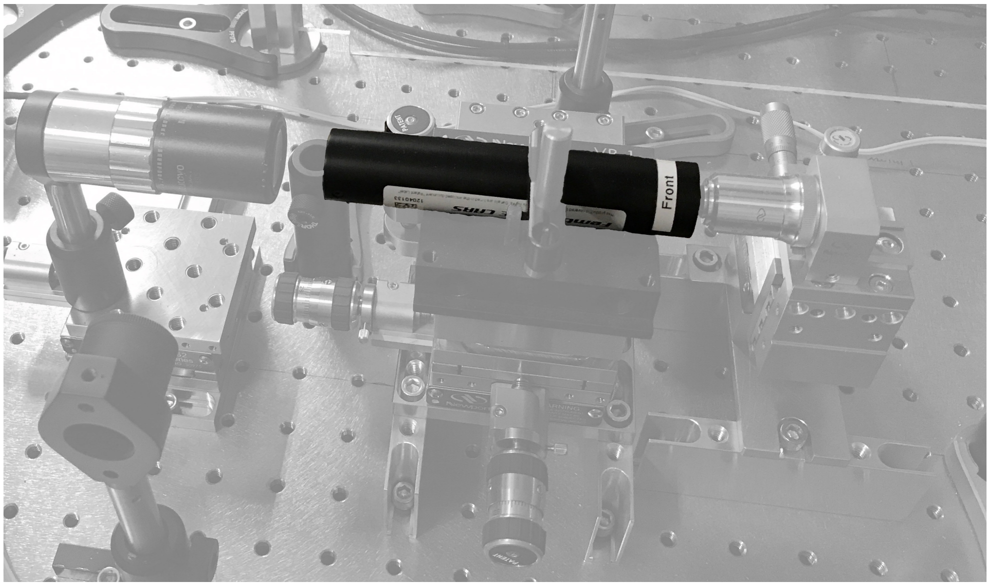

Figure 1.11: The FemtoWHITE CARS module, mounted on a fibre-coupling kit. the 1" diameter module contains a 12-cm length of an NL-1.4-775-945 photonic crystal fibre.

through studying the GVD curve (Fig. 1.10(c)). By pumping the fibre with sufficiently strong powers within the *anomalous dispersion region* (ADR), the pulse spectrally broadens beyond the *zero-dispersion wavelengths* (ZDWs) and leaves the ADR devoid of spectral power. However, pumping with weak powers allows the generation of supercontinuum within the ADR—a fact that is central to the technical advances I describe in the next chapter.

1.5.1 Supercontinuum within the ADR—The soliton

When a supercontinuum is generated within the ADR of the fibre, competing mechanisms from the Kerr effect and the negative GVD may result in the generation of pulses that do not experience dispersion—the pulse neither expands nor contracts as it propagates in the fibre.[8] This pulse that is unaffected by dispersion is able to retain its temporal and spectral shape and is called a *soliton*. In this thesis, solitons are mentioned occasionally in the context of supercontinuum generation, especially in Chapter 4 when discussing certain spectral features that impact the quality of CARS spectra.

---

[8] Consider $\lambda_1 < \lambda_2$. In a material with a normal dispersion curve $n(\lambda_1) > n(\lambda_2)$ while in a material with an anomalous dispersion curve $n(\lambda_1) < n(\lambda_2)$. Also see Appendix A for more details.

References

1. Raman, C. V. & Krishnan, K. S. A New Type of Secondary Radiation. *Nature* **121,** 501–502 (1928).
2. American Chemical Society. *C.V. Raman: The Raman Effect* 2018. https://www.acs.org/content/acs/en/education/whatischemistry/landmarks/ramaneffect.html (2018).
3. Hecht, E. *Optics* 5th (Pearson, 2016).
4. Cheng, J.-X. & Xie, X. S. *Coherent Raman Scattering Microscopy* (CRC Press, 2012).
5. McCreery Group. *Raman Materials* https://www.chem.ualberta.ca/%7B~%7Dmccreery/ramanmaterials.html (2018).
6. Maker, P. D. & Terhune, R. W. Study of Optical Effects Due to an Induced Polarization Third Order in the Electric Field Strength. *Physical Review* **137,** A801–A818 (1965).
7. Potma, E. O. & Mukamel, S. *Theory of Coherent Raman Scattering* 3–42 (2013).

8. Hartshorn, C. M. *et al.* Multicomponent chemical imaging of pharmaceutical solid dosage forms with broadband CARS microscopy. *Analytical Chemistry* **85,** 8102–8111 (2013).

9. Cheng, J.-X., Volkmer, A. & Xie, X. S. Theoretical and experimental characterization of coherent anti-Stokes Raman scattering microscopy. *Journal of the Optical Society of America B* **19,** 1363 (2002).

10. Evans, C. L. & Xie, X. S. Coherent Anti-Stokes Raman Scattering Microscopy: Chemical Imaging for Biology and Medicine. *Annual Review of Analytical Chemistry* **1,** 883–909 (2008).

11. Petrov, G. I. *et al.* Comparison of coherent and spontaneous Raman microspectroscopies for noninvasive detection of single bacterial endospores. *Proceedings of the National Academy of Sciences* **104,** 7776–7779 (2007).

12. Saar, B. G. *et al.* Video-Rate Molecular Imaging in Vivo with Stimulated Raman Scattering. *Science* **330,** 1368–1370 (2010).

13. Evans, C. L. *et al.* Chemical imaging of tissue in vivo with video-rate coherent anti-Stokes Raman scattering microscopy. *Proceedings of the National Academy of Sciences* **102,** 16807–16812 (2005).

14. Pegoraro, A. F., Slepkov, A. D., Ridsdale, A., Moffatt, D. J. & Stolow, A. Hyperspectral multimodal CARS microscopy in the fingerprint region. *Journal of Biophotonics* **7,** 49–58 (2014).

15. Porquez, J. G., Cole, R. A., Tabarangao, J. T. & Slepkov, A. D. Spectrally-broad coherent anti-Stokes Raman scattering hyper-microscopy utilizing a Stokes supercontinuum pumped at 800 nm. *Biomedical Optics Express* **7,** 4335 (2016).

16. Ogawa, M. *et al.* Label-free biochemical imaging of heart tissue with high-speed spontaneous Raman microscopy. *Biochemical and Biophysical Research Communications* **382,** 370–374 (2009).
17. Cheng, J.-X. & Xie, X. S. Coherent Anti-Stokes Raman Scattering Microscopy: Instrumentation, Theory, and Applications. *Journal of physics Chemical B* **108,** 827–840 (2004).
18. Camp Jr, C. H. & Cicerone, M. T. Chemically sensitive bioimaging with coherent Raman scattering. *Nature Photonics* **9,** 295–305 (2015).
19. Camp Jr, C. H. *et al.* High-speed coherent Raman fingerprint imaging of biological tissues. *Nature Photonics* **8,** 627–634 (2014).
20. Vartiainen, E. M., Rinia, H. A., Müller, M. & Bonn, M. Direct extraction of Raman line-shapes from congested CARS spectra. *Optics Express* **14,** 3622 (2006).
21. Camp Jr, C. H., Lee, Y. J. & Cicerone, M. T. Quantitative, comparable coherent anti-Stokes Raman scattering (CARS) spectroscopy: Correcting errors in phase retrieval. *Journal of Raman Spectroscopy* **47,** 408–415 (2016).
22. Liu, Y., Lee, Y. J. & Cicerone, M. T. Broadband CARS spectral phase retrieval using a time-domain Kramers–Kronig transform. *Optics Letters* **34,** 1363 (2009).
23. Duncan, M. D., Reintjes, J. & Manuccia, T. J. Scanning coherent anti-Stokes Raman microscope. *Optics Letters* **7,** 350 (1982).
24. Zumbusch, A., Holtom, G. R. & Xie, X. S. Three-Dimensional Vibrational Imaging by Coherent Anti-Stokes Raman Scattering. *Physical Review Letters* **82,** 4142–4145 (1999).

25. Cheng, J.-X., Volkmer, A., Book, L. D. & Xie, X. S. An Epi-Detected Coherent Anti-Stokes Raman Scattering (E-CARS) Microscope with High Spectral Resolution and High Sensitivity. *The Journal of Physical Chemistry B* **105,** 1277–1280 (2001).

26. Pegoraro, A. F. *et al.* All-fiber CARS microscopy of live cells. *Optics Express* **17,** 20700 (2009).

27. Barlow, A. M., Slepkov, A. D., Ridsdale, A., McGinn, P. J. & Stolow, A. Label-free hyperspectral nonlinear optical microscopy of the biofuel micro-algae Haematococcus Pluvialis. *Biomedical Optics Express* **5,** 3391 (2014).

28. Garrett, N. L., Lalatsa, A., Uchegbu, I., Schätzlein, A. & Moger, J. Exploring uptake mechanisms of oral nanomedicines using multimodal nonlinear optical microscopy. *Journal of Biophotonics* **5,** 458–468 (2012).

29. Tu, H. *et al.* Stain-free histopathology by programmable supercontinuum pulses. *Nature Photonics* **10,** 534–540 (2016).

30. Cheng, J.-X., Volkmer, A., Book, L. D. & Xie, X. S. Multiplex Coherent Anti-Stokes Raman Scattering Microspectroscopy and Study of Lipid Vesicles. *The Journal of Physical Chemistry B* **106,** 8493–8498 (2002).

31. Kee, T. W. & Cicerone, M. T. Simple approach to one-laser, broadband coherent anti-Stokes Raman scattering microscopy. *Optics Letters* **29,** 2701 (2004).

32. Hellerer, T., Enejder, A. M. & Zumbusch, A. Spectral focusing: High spectral resolution spectroscopy with broad-bandwidth laser pulses. *Applied Physics Letters* **85,** 25–27 (2004).

33. Pegoraro, A. F. *et al.* Optimally chirped multimodal CARS microscopy based on a single Ti:sapphire oscillator. *Optics express* **17,** 2984–2996 (2009).

34. Potma, E. O., Evans, C. L. & Xie, X. S. Heterodyne coherent anti-Stokes Raman scattering (CARS) imaging. *Optics Letters* **31,** 241 (2006).

35. Cheng, J.-X., Book, L. D. & Xie, X. S. Polarization coherent anti-Stokes Raman scattering microscopy. *Optics letters* **26,** 1341–3 (2001).

36. Ideguchi, T. *et al.* Coherent Raman spectro-imaging with laser frequency combs. *Nature* **502,** 355–358 (2013).

37. Krishnamachari, V. V. & Potma, E. O. Multi-dimensional differential imaging with FE-CARS microscopy. *Vibrational Spectroscopy* **50,** 10–14 (2009).

38. Bégin, S. *et al.* Coherent anti-Stokes Raman scattering hyperspectral tissue imaging with a wavelength-swept system. *Biomedical Optics Express* **2,** 1296 (2011).

39. Volkmer, A., Book, L. D. & Xie, X. S. Time-resolved coherent anti-Stokes Raman scattering microscopy: Imaging based on Raman free induction decay. *Applied Physics Letters* **80,** 1505–1507 (2002).

40. Rocha-Mendoza, I., Langbein, W., Watson, P. & Borri, P. Differential coherent anti-Stokes Raman scattering microscopy with linearly chirped femtosecond laser pulses. *Optics letters* **34,** 2258–2260 (2009).

41. Trebino, R. *Talks (Lectures)* `http://frog.gatech.edu/talks.html` (2018).

42. Rocha-Mendoza, I., Langbein, W. & Borri, P. Coherent anti-Stokes Raman microspectroscopy using spectral focusing with glass dispersion. *Applied Physics Letters* **93,** 201103 (2008).

43. Cole, R. A. & Slepkov, A. D. Interplay of pulse bandwidth and spectral resolution in spectral-focusing CARS microscopy. *Journal of the Optical Society of America B* **35,** 842 (2018).

44. Dudley, J. M., Genty, G. & Coen, S. Supercontinuum generation in photonic crystal fiber. *Reviews of Modern Physics* **78,** 1135–1184 (2006).

45. Hilligsøe, K. M. *et al.* Supercontinuum generation in a photonic crystal fiber with two zero dispersion wavelengths. *Optics Express* **12,** 1045 (2004).

Chapter 2

Broadband Spectral Focusing CARS With a Supercontinuum Stokes

2.1 Chapter preface

As described in the previous chapter, there are several experimental approaches for implementing CARS microscopy. Each approach is a trade-off between imaging speed and the quality (or density) of CARS spectra. Prior to my work at Trent, there was active work by Dr. Slepkov and others to improve the spectroscopy aspects of SF-CARS by extending the accessible spectral range to the fingerprint region below 1600 cm^{-1}. The “Econo-CARS” approach developed in Dr. Stolow’s lab—wherein a *Stokes supercontinuum* is generated from an inexpensive PCF module—was promising, but technical difficulties prevented the generation of a supercontinuum in the wavelength range most useful for accessing the fingerprint. This chapter describes how we found that the commercial PCF module could be pumped in ways that are contrary to the typical recommended guidelines ultimately yielding a Stokes supercontinuum that is less bright but far more useful for CARS spectroscopy in the fingerprint. I then demonstrate key attributes of our working *multimodal*-CARS system, and describe the implementation of a "Raman retrieval" algorithm that converts CARS spectra to more useful Raman-like spectra.

This chapter is based on work we published in 2016 in Biomedical Optics Express [1], and a poster presentation I gave at a clinical spectroscopy-oriented conference held in Montreal (SPEC 2016) [2].

2.2 Introduction

2.2.1 Limitations of most CARS microscopy systems

Detailed chemical mapping of samples requires microscopes that can perform fast and information-dense vibrational microscopy. Such microscopes can be used in the study of biology [3, 4]; inorganic materials [5]; drug analysis [6, 7], identification [8] and tracking [9]; and histology and histopathology [10, 11]. However, not all implementations of CARS microscopy can probe the entire vibrational frequency range from 500 $\mathrm{cm}^{-1} - 3500\ \mathrm{cm}^{-1}$. Most CARS microscopes are relegated to imaging at the CH/OH range above 2700 cm^{-1}. A few implementations, however, have successfully demonstrated wide scan range capabilities using broadband supercontinuum sources. These approaches include a multiplex CARS system [12], a supercontinuum equipped SF-CARS system [13], and a spectrally broad ultrafast laser equipped SF-CARS system [14]. A single-frequency (narrowband pump and Stokes) CARS system has not yet shown the capability of spectrally-wide CARS *hyperspectroscopy*. Although each of these systems has its strengths and weaknesses, an SF-CARS system has the advantage of being versatile (can quickly switch from an imaging-oriented or a spectroscopy-oriented system) and simple (through the use of a single standalone laser source). As discussed previously (see 1.4.4), even though SF-CARS is predominantly an "imaging-first" technique, it can perform relatively fast spectral acquisition.

2.2.2 Supercontinuum-based SF-CARS

SF-CARS has been implemented using three distinct experimental approaches: with two synchronized laser sources to generate the pump/probe and Stokes—an approach similar to single-frequency CARS but with chirp-matched pulses [15]; by using a single spectrally ultrabroad sub-25-fs laser source with intra-pulse filtering to split the pump/probe and Stokes [14, 16]; or by using a PCF to generate a supercontinuum from which some (or all) of the pump/probe/Stokes beams are derived [3, 10, 17, 18] (such as described here). Implementations of SF-CARS that use a single ultrabroad laser source have been successful in performing CARS hyperspectroscopy, although there are unique technical challenges and costs associated with unwanted dispersion in such a short pulse. On the other hand, SF-CARS systems using PCFs to generate the supercontinuum Stokes beam are among the most cost-effective solutions for CARS microscopy, despite often yielding spectral intensities and bandwidths that are insufficient for broadband CARS microscopy.

In order to access the fingergprint region, most current SF-CARS systems require either different sets of optics [14], different pump wavelengths [13], or even totally different sets of experimental setups (e.g., one setup is designed for the fingerprint frequencies and the other for the CH/OH frequencies) [16]. However, an approach, requiring only a single set of optics, that can perform broadband CARS hyperspectroscopy in a single-scan window, can be achieved using a supercontinuum-based SF-CARS, as shown in this chapter.

2.2.3 The problem with supercontinuum-based SF-CARS

The use of PCFs for SF-CARS is not straightforward, and it comes with consequences. Due to the spectral character of the supercontinuum generated by PCFs—being weak or non-existent in some wavelengths and strong in others—access to a broad range of vibrational frequencies can be limited. The PCF module most typically used for SF-CARS , the FemtoWHITE CARS[19], has been selected by some groups for its convenient form, spectral stability and strong supercontinuum generating characteristics beyond its 945 nm ZDW [20–24]. Previous work by Hilligsøe *et al.* established that this fibre can efficiency generate supercontinua beyond its two ZDWs (775 nm and 945 nm) when pumped with sub-70 fs *transform-limited* pulses [25]. However, between the two ZDWs, this fibre has not been shown to generate supercontinuum with enough spectral intensity to be useful for CARS (refer to Fig. 1.10). This means that when using a standard 800-nm ($\omega_P = 12500$ cm^{-1}) laser as the PCF seed, Stokes can only be generated at wavelengths above 945 nm ($\omega_S < 10600$ cm^{-1}). When the same 800 nm pulse is used as the CARS pump/probe, the lowest CARS frequency accessible is $\omega_P - \omega_S > 1900$ cm^{-1}.

2.2.4 Accessing the fingerprint region

Ultrafast laser systems have been designed to generate transform-limited pulses—the shortest possible pulse with the current spectral bandwidth of the laser. With dispersion, the length of the pulse increases, and along with it, spectral components separate more in time, at which point the pulse is no longer considered to be transform-limited. When lower frequency parts of the pulse lead, the pulse is said to be positively-chirped. Otherwise, when higher frequency parts lead, the pulse is negatively-chirped. For example, the pulses depicted in Figure 1.8f are positively chirped.

Literature recommendations for use of the FemtoWHITE CARS module suggest that for generating the most stable, quiet and broad supercontinuum, transform-limited pulses must be used [26, 27]. However, transform-limited pulses have higher pulse peak powers than dispersed pulses, and thus, the use of transform-limited pulses induces more nonlinearities in supercontinuum generation and may drive the supercontinuum outside the fibre's two ZDW. Thus, by using chirped pulses to pump the PCF, supercontinuum can be generated with spectral intensity within the two ZDWs. Furthermore, by using relatively longer seed pulses than are typically recommended, the supercontinuum generation process becomes advantageously less efficient. This means that more Stokes light can be generated before the cascade of nonlinearities pushes the supercontinuum beyond the 940 nm ZDW. The resulting Stokes supercontinuum can enable CARS hyperspectroscopy reaching frequencies as low as 630 cm^{-1} when generated by > 100 fs, 800 nm pulses, thus removing the need for wavelength tunable laser oscillators.

Relaxing requirements for transform-limited pulses and tunable laser oscillators for CARS microscopy significantly lowers the complexity and cost of what is already one of the least expensive and most agile approaches to implementing multimodal CARS hyperspectral microscopy, thus opening the technique to a new segment of nonlinear-optical microscopy laboratories.

2.3 Experiment

A schematic of the experimental setup is shown in Fig. 2.1. A Ti:Sapphire oscillator (Spectra-Physics Tsunami) generates an 800 nm beam with variable pulse duration from ≈ 70 fs up to 200 fs. A *half-wave plate* (HWP) and cube polarizer act as a variable-power beam splitter to separate the main beam into the pump/probe and Stokes beams. The pump beam is routed to a computer-controlled optical delay stage (Thorlabs DDS220) before re-combining with the Stokes. The other beam is coupled into a commercial PCF-based supercontinuum generation module (FemtoWHITE-CARS, NKT Photonics) using a Newport M-40× objective lens to generate the Stokes beam. The Stokes beam is collimated with a Mitutoyo M Plan NIR 50× long-working distance objective. The end-to-end PCF coupling efficiently is ≈ 55%. Both beams are combined using a Semrock LPF-937 filter oriented at 45 degrees incidence, making it an effective 840 nm long-pass filter (see Appendix B for more details regarding specific filter characteristics).

The pump and Stokes are co-polarized with the use of independent HWPs (Thorlabs AHWP05M-980 for the supercontinuum Stokes; Thorlabs WPH05M-808 for the pump) situated in between the fibre module and the beam-combiner. A broadband polarizer (Thorlabs LPVIS050) located before the microscope entrance further ensures co-polarization of both beams. The use of co-polarized pump and Stokes beams

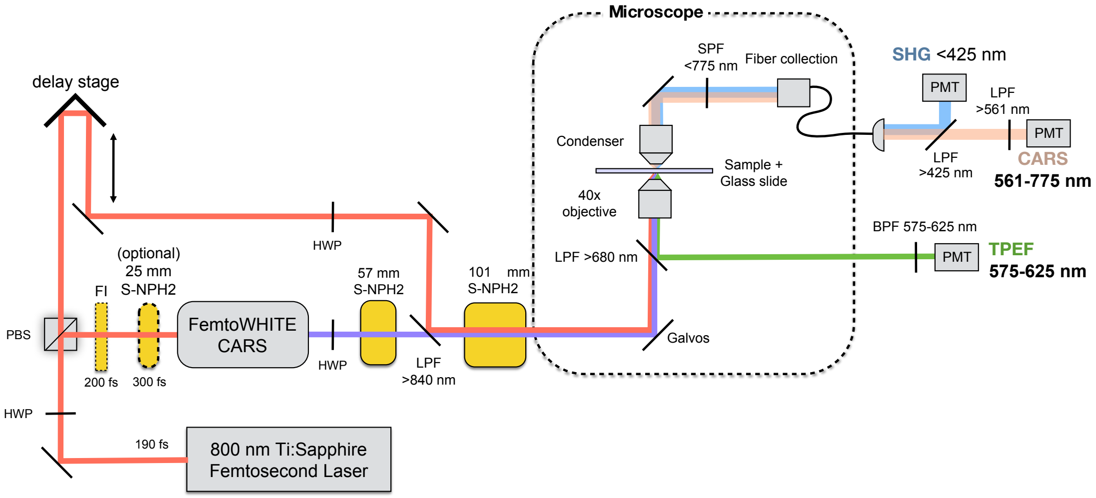

Figure 2.1: A simplified schematic of the multimodal CARS microscopy setup. A Ti:Sapphire oscillator generates 190 fs pulses at 800 nm, which splits into the pump and Stokes-generating beams. The Stokes-generating beam passes through a Faraday isolator (FI) before being coupled into the FemtoWHITE CARS (NKT Photonics) microstructured-fibre module that generates the supercontinuum Stokes. Blocks of high-dispersion S-NPH2 glass are used to disperse and match the chirps of the pump and Stokes pulses. The pump and Stokes beams are recombined using a long-pass filter (LPF) and routed to the laser-scanning microscope. Isotropically-generated TPEF is collected in the backward direction, reflected by a dichroic and detected by a PMT. Forward-generated SHG and CARS signals are isolated with a short-pass filter (SPF) and collected using a customized multimode-fibre assembly and routed off-board, where they are wavelength-separated en route to separate PMTs.

allow for the optimal generation of anti-Stokes signals (see Appendix C for a note on signal polarization).

2.3.1 Dispersion and chirp-matching

The pump and Stokes beams are dispersed by a total of 101 mm and 158 mm of S-NPH2 glass, respectively, before entering the microscope. Not including other dispersion in the optical setup, this added glass represents 30000 fs^2 of dispersion (GDD) in the pump, and between 28000 fs^2 and 43000 fs^2 of dispersion in the Stokes beam, which extends from 1090 nm ($\Omega_R = 3300$ cm^{-1}) to 840 nm ($\Omega_R = 600$ cm^{-1}). The lengths of these glass blocks are chosen to match the chirps of the pump and Stokes pulses, thereby enabling SF-CARS with an optimized spectral resolution of ≈ 25 cm^{-1} at the CH vibration region (≈ 2900 cm^{-1}). The pump is dispersed to a duration of ≈ 1 ps, with a chirp parameter, β, of approximately 120 cm^{-1}/ps. Likewise, the red-shifted portion of the supercontinuum Stokes is lengthened to more than 20 ps. The Stokes is predominantly linearly chirped with little higher-order dispersion effects resulting in an average linear chirp of 130 cm^{-1}/ps. Thus, the spectral resolution does not vary significantly along the CARS spectrum.

2.3.2 The microscope

The microscope is a modified Olympus IX73 inverted laser-scanning microscope equipped with an Olympus UAPON 40XW340 (a 40× water immersion objective), a Thorlabs galvo system (GVS002), an x-y computerized sample stage (MLS203-1), and a unique multimodal fibre collection system in the transmitted direction as described in ref [28]. TPEF signals are collected in a non-descanned *epi*-channel, i.e., the TPEF signal is collected in the backward direction without re-traversing the galvo mirror system (see Fig. 2.1). SHG and CARS signals are collected in the forward direction and are wavelength-separated by a dichroic filter, with each of the two signals going to separate detectors. Hamamatsu H10723-01 PMTs are used in all three channels although later upgraded for studies reported in the subsequent chapters. Alternatively, the SHG and CARS signals can be sent to a modular fibre-coupled

USB spectrometer (Black Comet CXR SR-50, StellarNet) for signal monitoring and calibration of vibrational frequency as a function of pump delay stage position.

2.3.3 Other experiment details

The Stokes spectra generated by the fibre module were recorded using an *optical spectrum analyzer* (OSA) (Hewlett Packard HP 70450A). Pulse durations and chirps were measured with a home-built scanning interferometric autocorrelator [29]. Data acquisition and microscope control were implemented using a custom LabView interface. Data analysis and image processing were conducted using LabView, Python, and ImageJ [30]. Detailed information on home-built data aquisition and microscopy software, as well as on the wiring of the microscope system (including data aquisition board and detectors) can be found in Appendix D and E.

2.4 Results and discussions

2.4.1 Generating the supercontinuum for the fingerprint

The FemtoWHITE CARS module houses a PCF, *NL-1.4-775-945*, with ZDWs at 775 nm and 945 nm (recall Fig. 1.10 for its dispersion properties). Originally, Hilligsöe *et al.* modeled the power-dependent supercontinuum spectra from the FemtoWHITE CARS using transform-limited 40 fs PCF pump pulses and studied it as a function of pulse energy rather than peak intensity [25]. With such short pulses and their associated large peak powers, cascaded nonlinearities provide efficient spectral broadening thus rapidly evolving the spectral weight of the supercontinuum beyond the two ZDWs and leaving the ADR largely devoid of spectral power. One consequence of efficient spectral broadening is that access to Stokes frequencies near that of the pump becomes limited, therefore also limiting the vibrational resonances that can be probed. Previous work by Pegoraro *et al.*, using the FemtoWHITE CARS, overcame this obstacle and demonstrated CARS microscopy at fingerprint frequencies (< 1800 cm^{-1}) by using weaker PCF pump powers to lessen the spectral broadening of the Stokes and concentrate its intensity at 1000 nm while concurrently shifting the pump wavelength above 900 nm—closer to the 945 ZDW [13]. While this approach works to some degree, the need to change the pump wavelength significantly away from 800 nm is problematic as it requires changing various routing and collection filters; the detection of anti-Stokes wavelengths above 820 nm where alkali PMTs are precipitously inefficient; and requires a broadly-tunable laser oscillator source. Furthermore, the need to reduce the PCF pump power meant a corresponding reduction in generated Stokes power available for imaging [13].

We find that by using longer pulses (or ones that are already chirped), a significant amount of Stokes power within the ADR can be generated. Using longer pulses means that the peak intensity in the fibre is reduced, thereby significantly reducing spectral broadening in the supercontinuum generation process while maintaining large PCF pump pulse intensities. This allows us to access vibrational resonances across the fingerprint, silent, and CH/OH regions in a single-scan window with a single microscope setup. This principle is demonstrated in Fig. 2.2 where it is shown that pumping the PCF with 190 fs, 800 nm pulses generate supercontinua close to the pump wavelength which are useful for accessing the fingerprint vibrational frequencies. A stable and strong *soliton*, seen as an intense power-dependent peak, is also found to be generated in the supercontinuum (see Fig. 2.2(c)). Introducing additional dispersion to

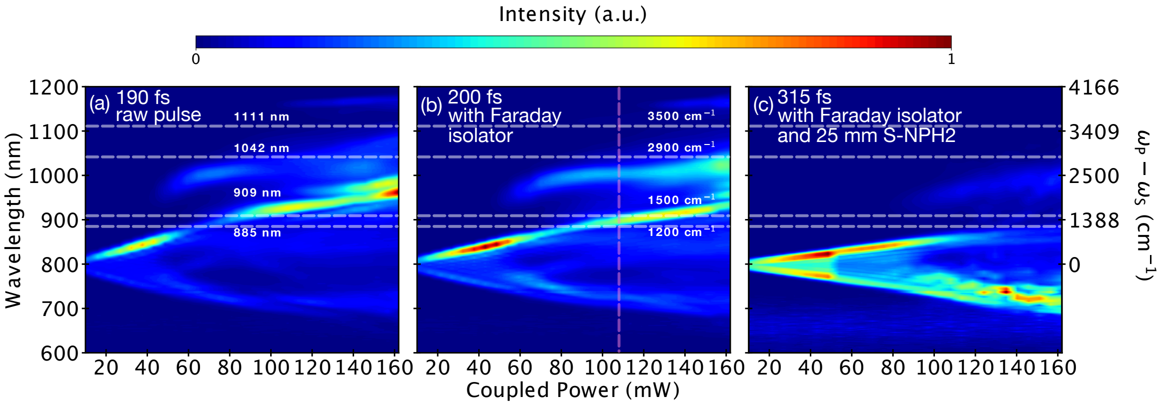

Figure 2.2: Power-dependent spectra of the FemtoWHITE-CARS plotted in wavelength (left scale) and the difference frequency (right scale), $\Omega_R = \omega_P - \omega_S$. Generated supercontinuum (a) from transform-limited 190 fs input pulses; (b) when the 190 fs input pulses are dispersed to 200 fs by a Faraday isolator; (c) when the input pulses are further dispersed to 315 fs with a 25 mm block of high-dispersion glass. The dashed horizontal lines are guides to the eye that correspond to Stokes wavelengths used to probe some relevant fingerprint and CH/OH vibrational frequencies. The dashed vertical line in (b) represents the slice of the Stokes spectrum (coupled power of 110 mW) used for the proceeding hyperspectral imaging experiments.

the PCF pump pulse generates supercontinua with even greater spectral intensity closer to the pump wavelength. In this case, as shown in Fig. 2.2(b), the use of a Faraday isolator is doubly-advantageous as it adds dispersion to the PCF pump pulse for improved Stokes generation while also eliminating the destabilizing laser feedback to the oscillator. Such feedback is a common nuisance when using PCF modules [31]. However, as mentioned earlier, previous studies suggest that for low-noise supercontinuum generation, the PCF must be pumped with short transform-limited pulses [26, 27]. In that case, the use of an isolator is invariably complicated by the added need for a pulse compressor [26]. As shown in Fig. 2.2(b), the added dispersion offered by the isolator actually provides a more useful range of supercontinuum wavelengths for probing a wider span of vibrational resonances, removing the need for a pulse compressor. For any given pulse energy, the spectrum of the generated supercontinuum ultimately depends on the peak power in the fibre and thus adding too much dispersion before the PCF leads to insufficient spectral broadening beyond the 945 nm ZDW. For example, adding an extra 25 mm of high-dispersion S-NPH2 glass before the PCF yields a supercontinuum with more power close to the pump wavelength of 800 nm, but with insufficient power above 885 nm to probe vibrational resonances above 1200 cm^{-1} as shown in Fig. 2.2(c).

2.4.2 Anti-Stokes calibration

In SF-CARS, the CARS spectrum is scanned by varying the overlap of the pump and Stokes pulses through the delay stage. The delay stage system must be calibrated to convert its absolute spatial position to the pump-Stokes difference frequency, which is also equivalent to the vibrational frequency being probed, $\Omega_R = \omega_P - \omega_S$. The calibration is done by routing the anti-Stokes signal to a spectrometer rather than to the PMT. An *astaxanthin*-rich sample (AstaReal L10) is used as the calibration standard in this chapter as it exhibits both strong FWM and CARS at low pump powers [3, 18], e.g., less than 5 mW. Alternatively, a coverslip can be used as a calibration standard but requires nearly two orders of magnitude more pump powers. Figure 2.3(a) shows the CARS spectrogram of astaxanthin as a function of pump delay stage position. The CARS signal of astaxanthin, both based on Fig. 2.3(a) and (c), shows strong peaks at 1000 cm^{-1}, 1150 cm^{-1}, and 1520 cm^{-1}; weaker intermediary peaks at 1190 cm^{-1}, 1275 cm^{-1}, 1350 cm^{-1}, and 1430 cm^{-1} [32]; and a trailing NRB across the broad spectral range with a strong broad signal, reflective

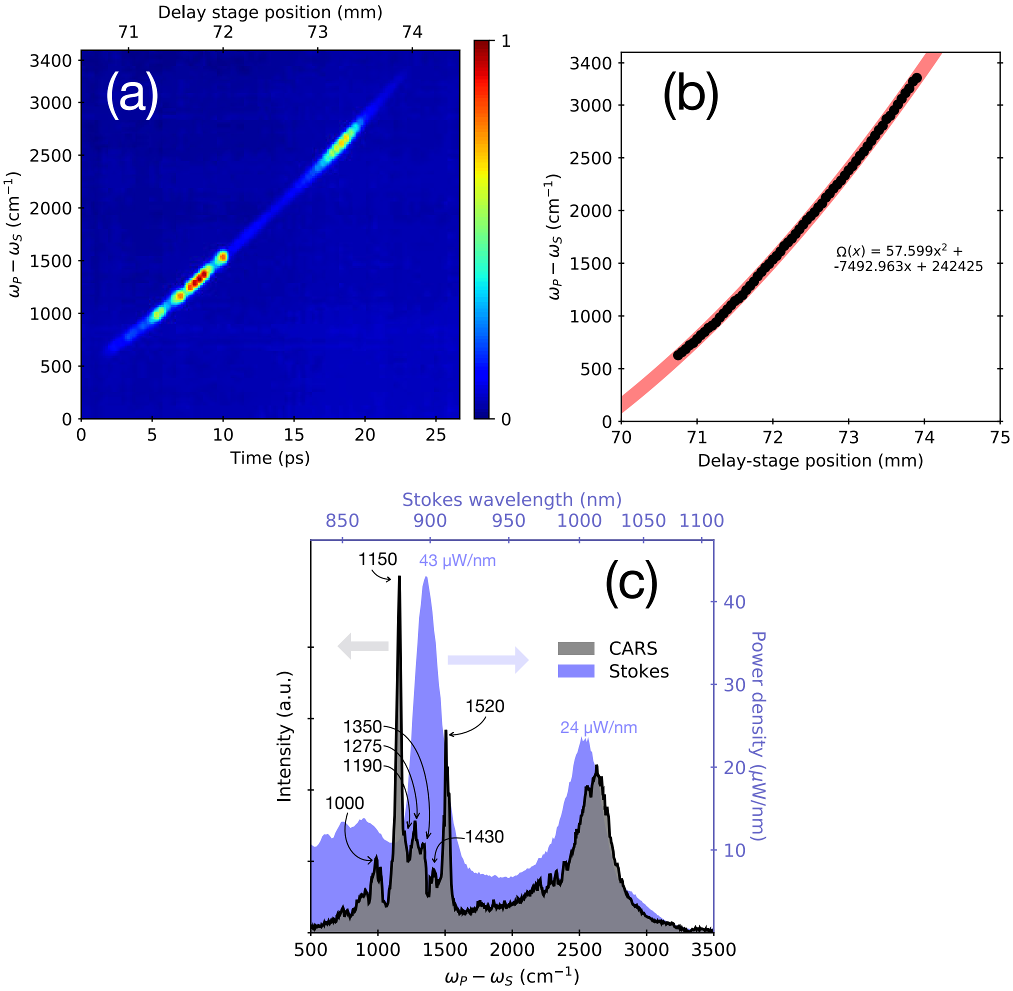

Figure 2.3: Anti-Stokes calibration spectrogram and the CARS spectrum of astaxanthin. (a) Spectrogram with a sampling spatial resolution of 50 μm (i.e., temporal resolution of 333 fs). The duration of the highly-chirped supercontinuum Stokes at the sample is approximately 25 ps. (b) Calibration-curve extracted from (a) fitted with a quadratic function where Ω is the pump-Stokes difference frequency and x is the delay stage position. (c) CARS spectrum of astaxanthin obtained through point scanning where 900 data points were obtained in 100 s, and the corresponding Stokes spectrum plotted as a function of both wavelength and the pump-Stokes difference frequency. Known astaxanthin peaks are shown at 1000 cm^{-1}, 1150 cm^{-1}, 1190 cm^{-1}, 1275 cm^{-1}, 1350 cm^{-1}, 1430 cm^{-1}, and 1520 cm^{-1} [3, 32]. The power densities of the Stokes at the 897 nm and 1001 nm peaks are estimated to be 43 μW/nm and 24 μW/nm, respectively. The pump power and the integrated Stokes power were measured to be 3.7 mW and 4.2 mW at the sample plane, respectively.

of the Stokes at $\omega_P - \omega_S > 2400$ cm^{-1} ($\lambda_S > 1000$ nm). As seen from the spectrogram the Stokes is sufficiently broad to access CARS frequencies from 630 cm^{-1} up to 3250 cm^{-1}. A calibration function can be generated by extracting points at maximum signal locations at each delay stage position and then fitted with a polynomial function (Fig. 2.3(b)). In this case, the curve is adequately fitted with a quadratic function which indicates that the Stokes has incurred some nonlinear chirp character (i.e. second-order dispersion effects). Nonlinear chirp effects become increasingly observable as pulse bandwidth is increased. In previous studies that used a narrower Stokes bandwidth, the chirp was assumed to be approximately linear [13].

2.4.3 CARS hyperspectroscopy

We demonstrate broadband CARS hyperspectroscopy on a sample containing a mixture of benzonitrile, dimethyl sulfoxide (DMSO), and strands of cellulose (cotton) fibres (Fig. 2.4); and grains of lily pollen (Fig. 2.5). The pump power was set to 100 mW and measured 74 mW at the sample plane—enough to probe strong vibrational modes in benzonitrile and DMSO across the vibrational spectrum (Fig. 2.4(a)). For the lily pollen, the pump power was set to 10 mW, weak enough to avoid sample degradation, and measured 7.4 mW at the sample plane. Benzonitrile has strong vibrational modes in the fingerprint at around 1000 cm^{-1}, 1200 cm^{-1}, and 1600 cm^{-1}, a single strong resonance at the silent-region at around 2230 cm^{-1}, and one at CH region at 3070 cm^{-1} [33]. DMSO has a strong resonance at 2910 cm^{-1} (C-H stretching) [34], however, two strong fingerprint modes of DMSO at 670 cm^{-1} (C–S symmetric stretching) and 700 cm^{-1} (C–S anti-symmetric stretching) were not detected, most

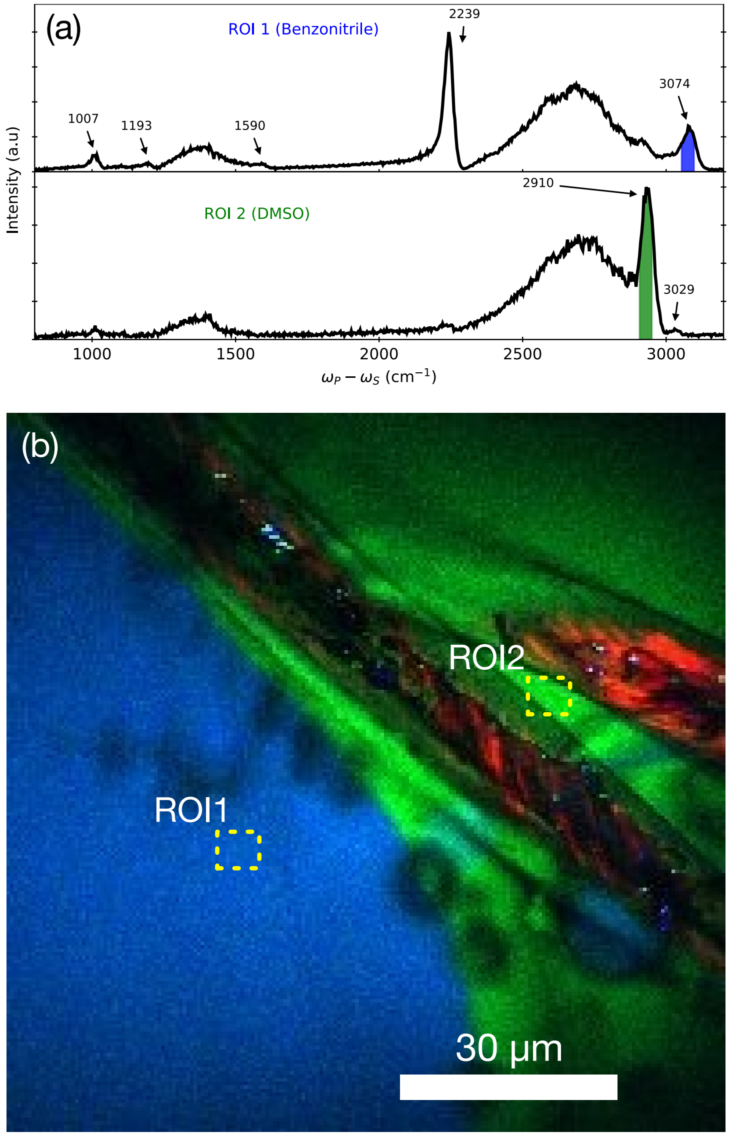

Figure 2.4: CARS hyperspectroscopy of a mixture of benzonitrile and dimethyl sulfoxide along with strands of cellulose fibres. (a) CARS spectra of benzonitrile and DMSO obtained from two 10 × 10-pixel regions of interest (ROIs) in (b). (b) A 200 × 200-pixel multimodal image of benzonitrile (CARS; blue contrast; 12 frames centred at 3070 cm^{-1}), DMSO (CARS; green contrast; 13 frames centred at 2910 cm^{-1}), and cellulose fibre (SHG; red contrast). Each image stack was taken at a duration of 0.8 seconds with a 13-μs pixel dwell time using a pump power of 74 mW measured at the sample plane. The input power in the PCF was maintained at 110 mW (200 fs PCF seed pulse duration) which generates supercontinuum with a power of 4.2 mW, as measured at the sample plane.

likely because of limited Stokes power at the requisite wavelengths. The results are summarized in Table 2.1.

Benzonitrile

Frequency (cm^{-1})	mode	detected
1000	C−C stretching	yes
1200	C−C deformation	yes
1600	C=C stretching	yes
2230	C≡N stretching	yes
3070	C–H stretching	yes

DMSO

Frequency (cm^{-1})	mode	detected
670	C−S symmetric stretching	no
700	C−S antisymmetric stretching	no
2910	C−H stretching	yes

Table 2.1: Summary of CARS results from the benzonitrile and DMSO sample mixture.

Benzonitrile and dimethyl sulfoxide

The 200 × 200-pixel CARS image of the sample mixture, Fig. 2.4(b) (processed using ImageJ), was generated by averaging 12 frames centred at 3070 cm^{-1} to identify benzonitrile (blue contrast); and 13 frames centred at 2910 cm^{-1} (green contrast) to identify DMSO. The cellulose fibre emitted a consistent SHG signal at 400 nm, and was used to generate the red-contrast in the multimodal image. Other prepared samples of similar cellulose fibres were subsequently found to emit CARS signals around 1100 cm^{-1}; however, in this particular sample, the CARS signal was overwhelmed by the strong NRB coming from the highly concentrated solvents. A higher resolution version of the image in Figure 2.4, formed by merging single frames acquired at 2230

$^{-1}$ and 2910 cm^{-1} with 5.3-μs pixel dwell time (2 seconds per image, 4 seconds total acquisition time) is shown in Appendix F.1.

Lily pollen

A 200 × 140-pixel CARS image of a grain of lily pollen is shown in Fig. 2.5. Strong CARS signals given off by carotenoid concentrations were found in the fingerprint region at 1154 cm^{-1} and 1533 cm^{-1}. 43 frames centred at 1154 cm^{-1} were averaged to show the carotenoid contrast in red. TPEF signals, detected in the epi-direction, were found to be originating from small chlorophyll-containing channels known as muri, and is shown in gray contrast. Interestingly, we also find strong TPEF signal from an unidentified substance that is co-localized with the (non-fluorescing) carotenoid CARS signal.

Hyperspectral smearing

The hyperspectral data, from which CARS images of Figs. 2.4 and 2.5 were derived, has a subtle artifact—the smearing of vibrational frequencies across an image. This smearing is caused by the spectral scanning methodology in our SF-CARS microscope and degrades the perceived spectral resolution. In most cases the effect of frequency smearing can be neglected, but when spectral resolution is of utmost importance, it must be minimized.

In SF-CARS, spectral scanning is done with a delay stage while image acquisition is done by scanning the pump and Stokes beams across the sample. Acquiring an image frame is always slower than spectral scanning, i.e., scanning the beams across the sample is slower than moving the delay stage. Obtaining rapid hyperspectral data

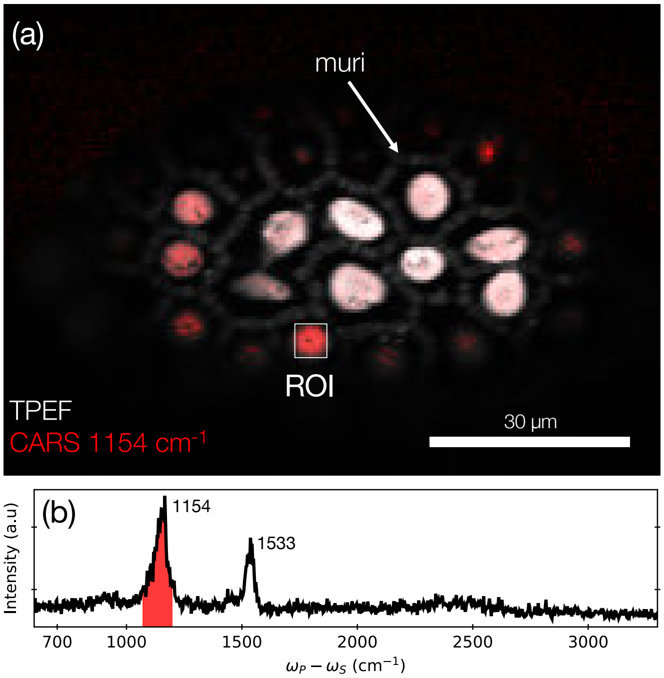

Figure 2.5: CARS hyperspectroscopy of a grain of lily pollen. (a) A 200 × 140-pixel (cropped) multimodal image of lily pollen containing carotenoids in the luminae (CARS; red contrast; 43 frames centred at 1154 cm^{-1}), and muri (TPEF; white contrast). (b) Raw CARS spectrum averaged over 10 × 10-pixel ROI in (c). The shaded spectral regions in (b) correspond to the image stacks averaged to produce the multimodal image. Each image stack was taken at a duration of 0.8 seconds with a 13-μs pixel dwell time using a pump power and 7.4 mW measured at the sample plane. The input power in the PCF was maintained at 110 mW (200 fs pulse duration) which generates supercontinuum with a power of 4.2 mW as measured at the sample plane.

through continuous image acquisition while spectral scanning is a typical feature of SF-CARS. However, it can lead to a "smearing" effect of vibrational frequencies in the hyperspectral data. Here, the top scan line of the image starts at a lower difference frequency, and the bottom scan line ends at a higher frequency. The extent of such smearing depends on factors such as the pulse lengths of both pump and Stokes beams, the speed of the delay stage, and the image acquisition speed—which includes pixel dwell time, resolution, and raster scan pattern. In this thesis, delay stage speeds used were as slow as 10 μm/s—corresponds to an average frequency scan of 4.3 cm^{-1}/s. This results in a smearing of 3.4 cm^{-1} from top to bottom of a frame. With a typical intrinsic spectral resolution of approximately 25 cm^{-1}, the addition of such smearing is very small, and thus does not motivate slower scanning speeds.

Comparison to other systems

By comparison to current state-of-the-art multiplex CARS approaches [12, 35], the hyperspectral acquisition capability (to span $\approx$ 2500 cm^{-1}) of our SF-CARS system is about four times slower. On the other hand, our imaging speeds are over 100 times faster. In comparison to the commonly used single-frequency (picosecond-pulse) CARS systems [36, 37], ours has a much slower imaging frame rate but has significantly better spectral acquisition capabilities (dense spectra and wide frequency span).

Our SF-CARS system can image live cells and molecular dynamics at two frames per second and can perform a 2500-cm^{-1}-wide hyperspectral image acquisition in under ten minutes (or single-pixel spectral acquisition in under two minutes). Thus, this system is most advantageous for research that requires both rapid imaging and rich label-free molecular fingerprinting where chemical/structural dynamics can be monitored on the second-to-minute timescales, such as live cell imaging and materials science applications.

Raman retrieval

Materials identification has been a challenge for CARS given that NRB signals affect the overall CARS spectral line shape. Consequently, retrieving Raman-like signals from CARS spectra may be deemed necessary to standardize materials identification in composite samples. Fortunately, so-called “phase retrieval” algorithms already exist such as the time-domain Kramers-Kronig transform [38, 39] and maximum entropy method [40]. These algorithms can be used to extract a Raman-like spectrum from raw CARS and reference NRB spectra. Most often, experimental implementation of these algorithms require collection of a reference NRB spectrum. Experimentally we obtain a NRB scan from samples that have no vibrational resonances in the concerned frequency range, such as the sample’s coverslip [39].

A retrieval algorithm based on the time-domain Kramers-Kronig transform, closely following the approach presented by Liu *et al.* [38] (see Appendix G.1), was used to extract a Raman-like spectrum from a raw CARS spectrum of nitrobenzene as shown in Fig. 2.6. The FWM spectrum was collected from the sample coverslip and used as the reference NRB. The retrieval algorithm effectively suppresses the NRB while adjusting the peak heights to provide a Raman-retrieved spectrum that closely resembles the spontaneous Raman spectrum. This clearly demonstrates that spectrally broad SF-CARS can be comparable to multiplex CARS [12] in the avenue of extracting Raman-like signals.

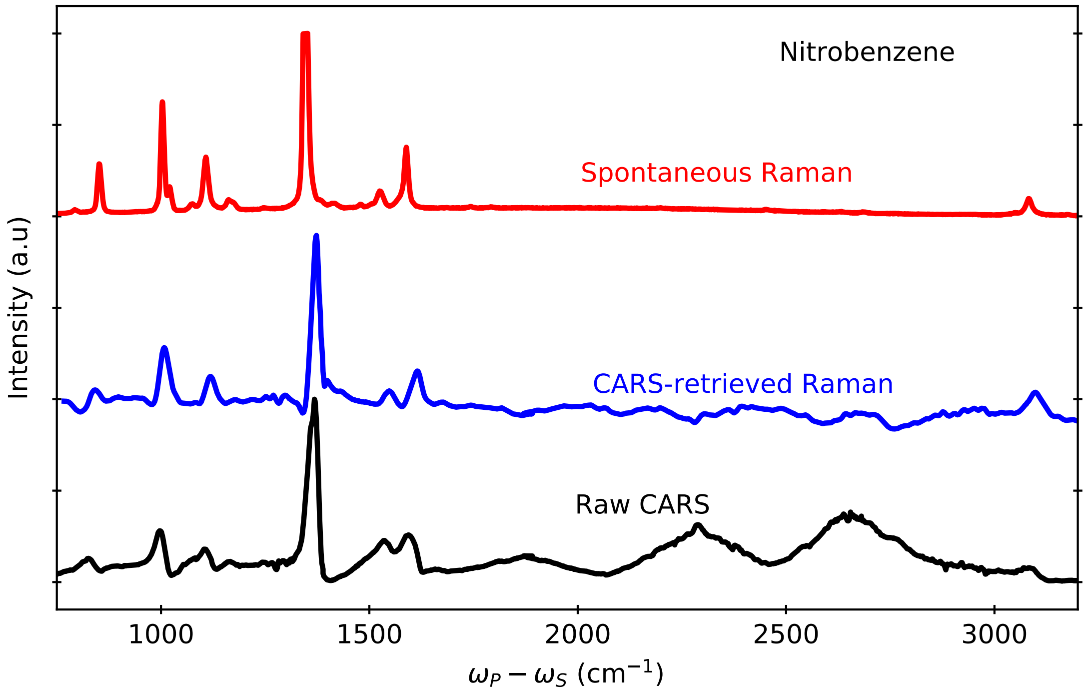

Figure 2.6: Demonstration of the Kramers-Kronig-based Raman-retrieval algorithm in a spectrally-broad SF-CARS system. The Raman-like spectrum (blue) was retrieved from the raw CARS signal (black) and a non-resonant background spectrum collected in the sample coverslip. A comparison to the spontaneous Raman spectrum obtained from a colleague's lab is shown as a reference (red).

2.5 Summary and conclusion

The work presented in this chapter demonstrates SF-based hyperspectral CARS microscopy spanning over 2500 cm^{-1} of the vibrational spectrum using a single 800 nm femtosecond laser, where the Stokes is generated by a commercially-available PCF. Despite being typically used to produce a supercontinuum outside of its two ZDWs, the spectral output of this PCF can be manipulated through power-tuning and pulse dispersion methods to yield spectra with significant power densities in the fibre's ADR near the pump wavelenth; therefore allowing better access to lower vibrational resonances deep in the fingerprint. This atypical use of the PCF opens up opportunities for constructing an economical and highly versatile single-laser coherent microscope system capable of broadband CARS microscopy and integrates well with existing nonlinear optical modalities such as TPEF and SHG. Overcoming the need to tune the pump wavelength away from 800 nm to access the fingerprint region, together with the ability to operate with lasers generating 100 fs to 200 fs pulses, significantly reduces the technical requirements of the experimental system, and thus opens the addition of hyperspectral CARS microscopy to many pre-existing nonlinear optical microscopy laboratories.

In this chapter, access to vibrational frequencies as low as 630 cm^{-1} has been demonstrated. In the next chapter, careful engineering of the supercontinuum generating pulse and a judicious choice of optics allows access to lower frequencies and a broader span of the vibrational spectrum. Furthermore, while the current work focused on the dispersion of the PCF pump pulse in a commercial PCF module with a 12-cm fibre, studying the possibility of using shorter lengths of the same fibre [25] to obtain higher spectral powers below 945 nm is a promising avenue for future research.

References

1. Porquez, J. G., Cole, R. A., Tabarangao, J. T. & Slepkov, A. D. Spectrally-broad coherent anti-Stokes Raman scattering hyper-microscopy utilizing a Stokes supercontinuum pumped at 800 nm. *Biomedical Optics Express* **7,** 4335 (2016).
2. Porquez, J. G., Cole, R. A., Tabarangao, J. T. & Slepkov, A. D. *Spectrally broad spectral-focussing-based coherent anti-Stokes Raman hyper-microscopy with a single 800-nm laser source* Montreal, Quebec, 2016.
3. Barlow, A. M., Slepkov, A. D., Ridsdale, A., McGinn, P. J. & Stolow, A. Label-free hyperspectral nonlinear optical microscopy of the biofuel micro-algae Haematococcus Pluvialis. *Biomedical Optics Express* **5,** 3391 (2014).
4. Zumbusch, A., Langbein, W. & Borri, P. Nonlinear vibrational microscopy applied to lipid biology. *Progress in Lipid Research* **52,** 615–632 (2013).
5. Burruss, R. C., Slepkov, A. D., Pegoraro, A. F. & Stolow, A. Unraveling the complexity of deep gas accumulations with three-dimensional multimodal CARS microscopy. *Geology* **40,** 1063–1066 (2012).
6. Hartshorn, C. M. *et al.* Multicomponent chemical imaging of pharmaceutical solid dosage forms with broadband CARS microscopy. *Analytical Chemistry* **85,** 8102–8111 (2013).

7. Fussell, A., Garbacik, E., Offerhaus, H., Kleinebudde, P. & Strachan, C. In situ dissolution analysis using coherent anti-Stokes Raman scattering (CARS) and hyperspectral CARS microscopy. *European Journal of Pharmaceutics and Biopharmaceutics* **85,** 1141–1147 (2013).
8. Porquez, J. G. & Slepkov, A. D. Application of spectral-focusing-CARS microscopy to pharmaceutical sample analysis. *AIP Advances* **8,** 095213 (2018).
9. Garrett, N. L., Lalatsa, A., Uchegbu, I., Schätzlein, A. & Moger, J. Exploring uptake mechanisms of oral nanomedicines using multimodal nonlinear optical microscopy. *Journal of Biophotonics* **5,** 458–468 (2012).
10. Tu, H. *et al.* Stain-free histopathology by programmable supercontinuum pulses. *Nature Photonics* **10,** 534–540 (2016).
11. Le, T. T., Huff, T. B. & Cheng, J.-X. Coherent anti-Stokes Raman scattering imaging of lipids in cancer metastasis. *BMC Cancer* **9,** 42 (2009).
12. Camp Jr, C. H. *et al.* High-speed coherent Raman fingerprint imaging of biological tissues. *Nature Photonics* **8,** 627–634 (2014).
13. Pegoraro, A. F., Slepkov, A. D., Ridsdale, A., Moffatt, D. J. & Stolow, A. Hyperspectral multimodal CARS microscopy in the fingerprint region. *Journal of Biophotonics* **7,** 49–58 (2014).
14. Pope, I., Langbein, W., Watson, P. & Borri, P. Simultaneous hyperspectral differential-CARS, TPF and SHG microscopy with a single 5 fs Ti:Sa laser. *Optics Express* **21,** 7096 (2013).

15. Hellerer, T., Enejder, A. M. & Zumbusch, A. Spectral focusing: High spectral resolution spectroscopy with broad-bandwidth laser pulses. *Applied Physics Letters* **85,** 25–27 (2004).

16. Chen, B.-C., Sung, J., Wu, X. & Lim, S.-H. Chemical imaging and microspectroscopy with spectral focusing coherent anti-Stokes Raman scattering. *Journal of Biomedical Optics* **16,** 021112 (2011).

17. Pegoraro, A. F. *et al.* Optimally chirped multimodal CARS microscopy based on a single Ti:sapphire oscillator. *Optics express* **17,** 2984–2996 (2009).

18. Slepkov, A. D. *et al.* In vivo hyperspectral CARS and FWM microscopy of carotenoid accumulation in H . Pluvialis . **8937,** 1–11 (2014).

19. NKT Photonics. *FemtoWHITE CARS* `http://www.nktphotonics.com/wp-content/uploads/sites/3/2015/03/femtoWHITE-CARS.pdf` (2017).

20. Pegoraro, A. F. *et al.* All-fiber CARS microscopy of live cells. *Optics Express* **17,** 20700 (2009).

21. Murugkar, S. *et al.* Coherent anti-Stokes Raman scattering microscopy using photonic crystal fiber with two closely lying zero dispersion wavelengths. *Optics express* **15,** 14028–14037 (2007).

22. Zeng, Y. *et al.* In vivo micro-vascular imaging and flow cytometry in zebrafish using two-photon excited endogenous fluorescence. *Biomedical Optics Express* **5,** 653 (2014).

23. Lin, J., Teh, S., Zheng, W., Wang, Z. & Huang, Z. Multimodal nonlinear optical microscopic imaging provides new insights into acetowhitening mechanisms

in live mammalian cells without labeling. *Biomedical Optics Express* **5,** 3116 (2014).

24. Li, B., Borri, P. & Langbein, W. Dual/differential coherent anti-Stokes Raman scattering module for multiphoton microscopes with a femtosecond Ti:sapphire oscillator. *Journal of Biomedical Optics* **18,** 066004 (2013).

25. Hilligsøe, K. M. *et al.* Supercontinuum generation in a photonic crystal fiber with two zero dispersion wavelengths. *Optics Express* **12,** 1045 (2004).

26. Pegoraro, A. F. *Developing single-laser sources for multimodal coherent anti-Stokes Raman scattering microscopy* Ph. D. Thesis (Queens University, 2011).

27. Naji, M., Murugkar, S. & Anis, H. Determining optimum operating conditions of the polarization-maintaining fiber with two far-lying zero dispersion wavelengths for CARS microscopy. *Optics Express* **22,** 10800 (2014).

28. Slepkov, A. D. *et al.* Forward-collected simultaneous fluorescence lifetime imaging and coherent anti-Stokes Raman scattering microscopy. *Journal of biomedical optics* **16,** 021103 (2011).

29. Diels, J.-C. M., Fontaine, J. J., McMichael, I. C. & Simoni, F. Control and measurement of ultrashort pulse shapes (in amplitude and phase) with femtosecond accuracy. *Applied Optics* **24,** 1270 (1985).

30. Schindelin, J. *et al. Fiji: An open-source platform for biological-image analysis* 2012. arXiv: `1081-8693`.

31. Newport. *Coherent anti-Stokes Raman scattering application note 36* `https://www.newport.com/medias/sys%7B%5C_%7Dmaster/images/images/hc0/h9a/8`

797076226078/Coherent-Anti-Stokes-%20Raman-Scattering-App-Note-36.pdf.

32. Kaczor, A., Turnau, K. & Baranska, M. In situ Raman imaging of astaxanthin in a single microalgal cell. *Analyst* **136,** 1109–1112 (2011).

33. Császár, A. G. & Fogarasi, G. Scaled quantum mechanical (SQM) force field and theoretical vibrational spectrum for benzonitrile. *Spectrochimica Acta Part A: Molecular Spectroscopy* **45,** 845–854 (1989).

34. Martens, W. N., Frost, R. L., Kristof, J. & Theo Kloprogge, J. Raman spectroscopy of dimethyl sulphoxide and deuterated dimethyl sulphoxide at 298 and 77 K. *Journal of Raman Spectroscopy* **33,** 84–91 (2002).

35. Camp Jr, C. H. & Cicerone, M. T. Chemically sensitive bioimaging with coherent Raman scattering. *Nature Photonics* **9,** 295–305 (2015).

36. Evans, C. L. *et al.* Chemical imaging of tissue in vivo with video-rate coherent anti-Stokes Raman scattering microscopy. *Proceedings of the National Academy of Sciences* **102,** 16807–16812 (2005).

37. Cheng, J.-X., Volkmer, A., Book, L. D. & Xie, X. S. An Epi-Detected Coherent Anti-Stokes Raman Scattering (E-CARS) Microscope with High Spectral Resolution and High Sensitivity. *The Journal of Physical Chemistry B* **105,** 1277–1280 (2001).

38. Liu, Y., Lee, Y. J. & Cicerone, M. T. Broadband CARS spectral phase retrieval using a time-domain Kramers–Kronig transform. *Optics Letters* **34,** 1363 (2009).

39. Camp Jr, C. H., Lee, Y. J. & Cicerone, M. T. Quantitative, comparable coherent anti-Stokes Raman scattering (CARS) spectroscopy: Correcting errors in phase retrieval. *Journal of Raman Spectroscopy* **47,** 408–415 (2016).

40. Vartiainen, E. M., Rinia, H. A., Müller, M. & Bonn, M. Direct extraction of Raman line-shapes from congested CARS spectra. *Optics Express* **14,** 3622 (2006).

Chapter 3

Spectral Surfing CARS

3.1 Chapter preface

In the previous chapter, I showed how our non-standard approach to pumping a commercial PCF module allows us to do SF-CARS microscopy in the fingerprint region of the spectrum. Unfortunately, we also found that the PCF module generates supercontinuum with large variability in brightness at different wavelengths. In some wavelengths, the supercontinuum contained little useful light for generating observable CARS signals. However, a key aspect of this spectral variability of the supercontinuum is its dependence on the power of the laser coupled into the PCF module. This chapter describes a creative way to use the power-dependence of the generated supercontinuum to yield brighter CARS signals, a technique we call "spectral surfing." I then show the benefits of spectral surfing through CARS hyperspectroscopy, and further show that this technique reduces a sample's exposure to potentially damaging laser light.

This chapter is based on work we published in Optics Letters [1], and talks we presented in optics-oriented conferences held in San Francisco (Photonics West 2017) and in Ottawa (Photonics North 2018), which was published in their respective proceedings [2, 3].

3.2 Introduction

3.2.1 The problems associated with PCF-based SF-CARS

PCF-based SF-CARS have the particular advantage of being one of the most economically feasible implementations of CARS microscopy. With the appropriate choice of PCF pump pulse characteristics, PCF-based SF-CARS can be capable of broadband vibrational hyperspectroscopy [4]—a feature that is missing in many (and probably all) modern commercially available CRS microscopes. Because of these aspects, we might be tempted to call PCF-based SF-CARS a gold standard for CARS microscopy, but major problems prevent our doing so. The most important problem is that PCFs generate noisy (high-frequency noise, >kHz) and unstable (low-frequency noise, ≈ Hz) supercontinua with regions of weak spectral brightness [5].

3.2.2 An approach to boosting the anti-Stokes signal in PCF-based SF-CARS

In PCF-based SF-CARS the supercontinuum can have highly variable brightness across its spectrum [4–7]. This spectral variety consequently affects the brightness of the anti-Stokes in those regions, as it varies linearly with Stokes intensity according to Eq. (1.9).

Likewise, because of the quadratic dependence of the anti-Stokes signal on the pump intensity, a method for increasing the brightness of the anti-Stokes is to increase the pump power. However, when the Stokes is virtually non-existent in some wavelength regions (Stokes starved condition), i.e., $I_S(\omega_S) \approx 0$, any realistic increase in the pump power will be insufficient for obtaining detectable signals. Furthermore, increasing the pump power may lead to undesirable consequences: For example, with pump powers already two to three orders of magnitude stronger than the Stokes, further raising the pump power may cause significant sample degradation which is a problem for most biological samples [8–12]. In a Stokes starved condition, increasing the Stokes power two or three-fold can significantly yield stronger anti-Stokes signals and thus, may lead to brighter CARS while also substantially minimizing sample damage.

3.2.3 Spectral surfing

The supercontinuum generated in PCF sources, especially those with closely lying ZDWs such as the FemtoWHITE CARS, are heavily dependent on PCF pump pulse characteristics such as peak power [5, 7]. For example, with short transform-limited PCF pump pulses (e.g., 40 fs at 790 nm) and with long, intense, pump pulses (e.g., 200 fs, 160 mW at 800 nm), the supercontinuum is rapidly driven past the ADR. However, with long but weak pulses (e.g., 200 fs, 50 mW at 800 nm) supercontinuum can be generated within the ADR. Thus, with flexibility in using longer pulses to pump the PCF, the location of spectral maximum in the supercontinuum can be varied as a function of PCF pump power [4, 13].

The dependence of the supercontinuum's spectral maximum on PCF pump power can be exploited for SF-CARS since, at a given delay-stage position, only a portion of the supercontinuum is overlapped with the pump pulse to generate the anti-Stokes.[1] Therefore, by concurrently optimizing the Stokes power at the wavelength most overlapped with the pump pulse during each step in a CARS scan, an overall improvement of CARS brightness across the spectral scan range can be achieved. We term such synchronization *"spectral surfing."*

Spectral surfing is conceptually similar to the soliton self-frequency shift approach to multiplex CARS by Andresen *et al.* [13]. In their work, they generate strong supercontinuum constrained within the ADR. In spectral surfing, the supercontinuum is dynamically-tuned and moves past the upper ZDW where broader Stokes can be used for SF-CARS. Furthermore, spectral surfing adapts seamlessly to the time-gated approach of SF-CARS, i.e., the use of a delay-stage, which otherwise would not be as useful for multiplex CARS as it uses a spectrometer to collect the anti-Stokes spectrum at once [14–16].

3.3 Experiment

The experiment setup was modified for spectral surfing as shown in Fig. 3.1. A motorized half-wave plate (Zaber X-RSW60C-E03-KX14A) followed by a Faraday isolator (Newport ISO-08-800-BB) is added before the PCF module. The HWP rotates the polarization of the PCF pump laser and is attenuated by a built-in polarizer in the Faraday isolator. Together, the HWP and the isolator act as a computer-controllable

---

[1] See Fig. 1.8(f). Not all portions of the Stokes supercontinuum is used in generating the anti-Stokes because the pump does not completely overlap the Stokes temporally.

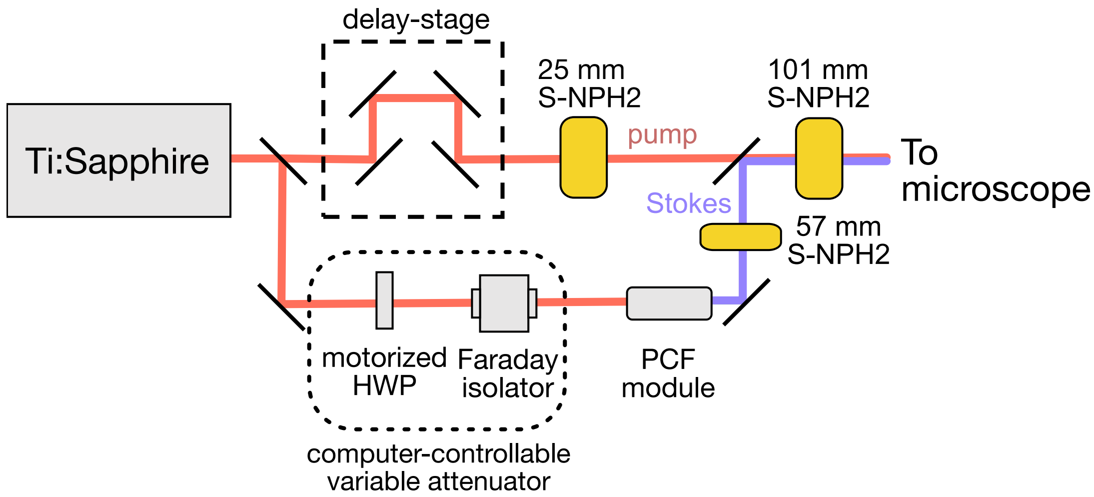

Figure 3.1: Schematic of the experimental layout for spectral-surfing. The output of a Ti:sapphire oscillator is split into pump and Stokes beams. A Stokes supercontinuum is generated in a PCF. The PCF pump power is actively controlled by the combination of a motorized HWP and isolator (computer-controllable beam attenuator). Blocks of SNPH-2 glass match the chirps of the two beams.

variable attenuator. The power-controlled PCF pump beam then passes through the PCF to generate the desired supercontinuum. The setup is further improved to provide more efficient transmission of the Stokes spectrum in the fingerprint by replacing the beam-combiner of the previous chapter (a 840 nm long pass combiner (Semrock LPF-937; see Appendix B for more details), with an 818 nm long pass combiner (Chroma T810LPXR). The CARS PMT is upgraded from a multialkali PMT (Hamamatsu 10723-01) to an extended red multialkali PMT (Hamamatsu 10723-20) to provide more efficient detection of the higher-wavelength anti-Stokes from the fingerprint region. A 25 mm of S-NPH2 high dispersion glass is added in the pump path to compensate for the dispersion added by the Faraday isolator which contains an 8-mm length of Terbium gallium garnet. This added glass yields a pump dispersion of 37000 fs^2. Table 3.1 shows the updated dispersion values in comparison to the non-spectral surfing setup described in Chapter 2. The pump powers used in collecting hyperspectral data was set to 50 mW (measuring ≈ 35 mW at the sample plane).

	Dispersion (fs^2)	
	Prior (Chap. 2)	Current (This chapter)
pump 800 nm	30000	37000
Stokes 840 nm	43000	44000
Stokes 940 nm	36000	37000
Stokes 1090 nm	28000	29000

Table 3.1: Dispersion calculations of the spectral surfing and the prior microscopy setup. In our previous setup, the pump was most chirp-matched with the Stokes at 1090 nm while in the work described in this chapter, the pump is most chirp-matched with the Stokes at 940 nm.

3.3.1 Implementing spectral surfing

To perform spectral surfing, we first take a spectral surfing calibration scan as shown in Fig. 3.2(a). The spectral surfing calibration scan is a set of supercontinuum spectra at different PCF pump powers and includes only relevant wavelengths, from 800 nm up to 1100 nm. From this figure, we can see that a particular PCF pump power generates (x-axis) a supercontinuum that can strongly stimulate a particular vibrational resonance (y-axis). Therefore, we can use this information to map the PCF pump power to the difference frequency (power-frequency map). By combining the power-frequency map with the delay stage calibration (position-frequency map), we can synchronize the computer-controllable beam attenuator to the delay stage which creates a position-power map.

Figure 3.2(b) shows our position-power mapping algorithm to implement spectral surfing. Here, the delay stage is continuously queried for the position and then

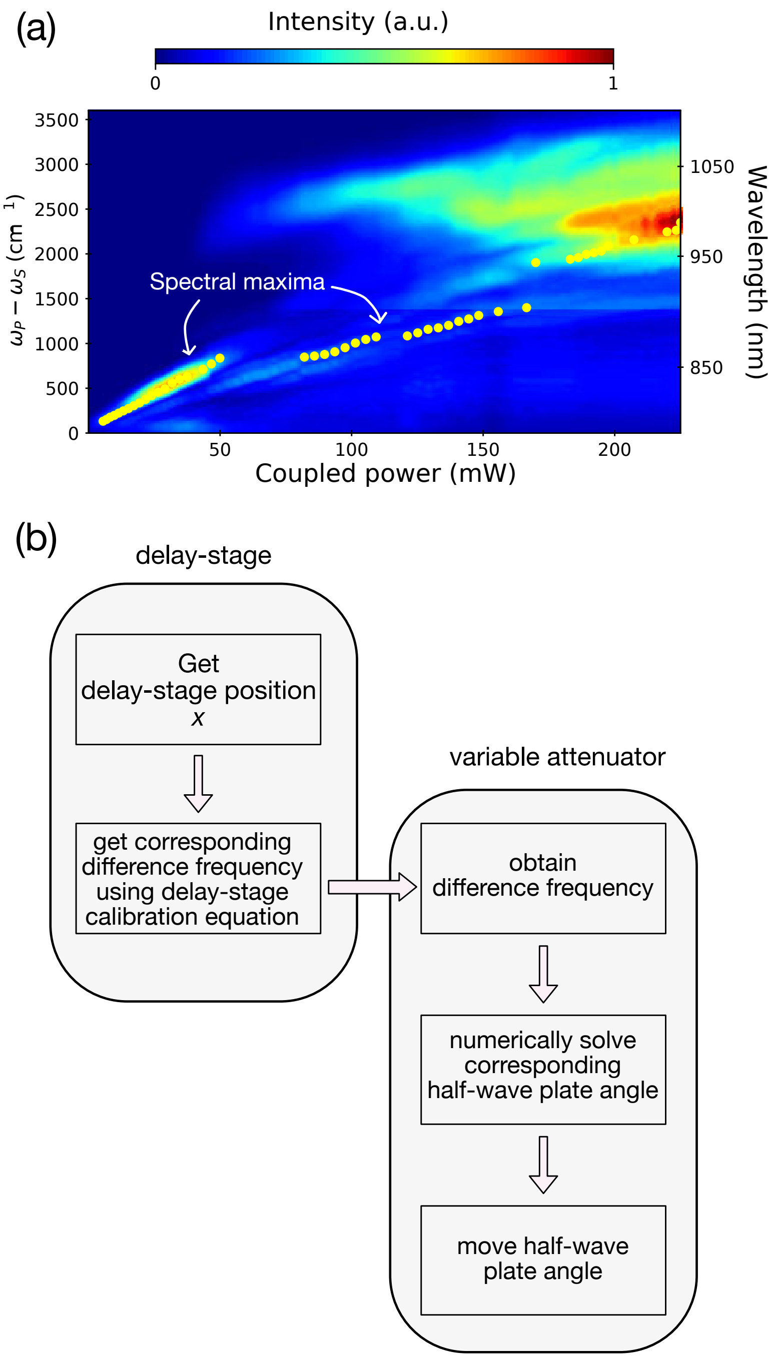

Figure 3.2: Spectral surfing calibration procedure. (a) Stokes spectrum versus PCF pump power. The yellow circles correspond to points of spectral maxima corresponding to an ideally unique difference-frequency, $\omega_P - \omega_S$. (b) Block algorithm for spectral surfing used to dynamically control the Stokes supercontinuum for CARS.

converted to difference-frequency through a delay stage calibration equation. The difference frequency is back-calculated as a PCF pump power (via Fig. 3.2(a), power-frequency map), which in our case, is equivalent to the HWP angle. We found that using linear interpolation to determine the PCF pump power (or HWP angle) in between data points (spectral maxima) yields satisfactory results for spectral surfing.

There may be cases in which the spectral surfing calibration procedure would not work properly mainly due to the supercontinuum generated by certain characteristics of PCF pump pulses. I suggest some methods to address this problem in Appendix H.

3.4 Results and discussions

3.4.1 A spectrally surfed Stokes supercontinuum

A visualization of the advantage of spectral surfing in supercontinuum generation is shown in Fig. 3.3. By using low PCF pump powers (37 mW), a Stokes supercontinuum can be generated that can strongly stimulate vibrational resonances from 600 cm^{-1} to 700 cm^{-1}. With higher PCF pump powers (220 mW) the supercontinuum strongly stimulates resonances in the CH/OH frequencies from 2000 cm^{-1} – 3500 cm^{-1}. With spectral surfing, however, a supercontinuum is generated with a higher overall effective intensity that can stimulate resonances from 400 cm^{-1} – 800 cm^{-1} in the fingerprint and 2000 cm^{-1} – 3500 cm^{-1} in the silent to CH/OH frequencies.

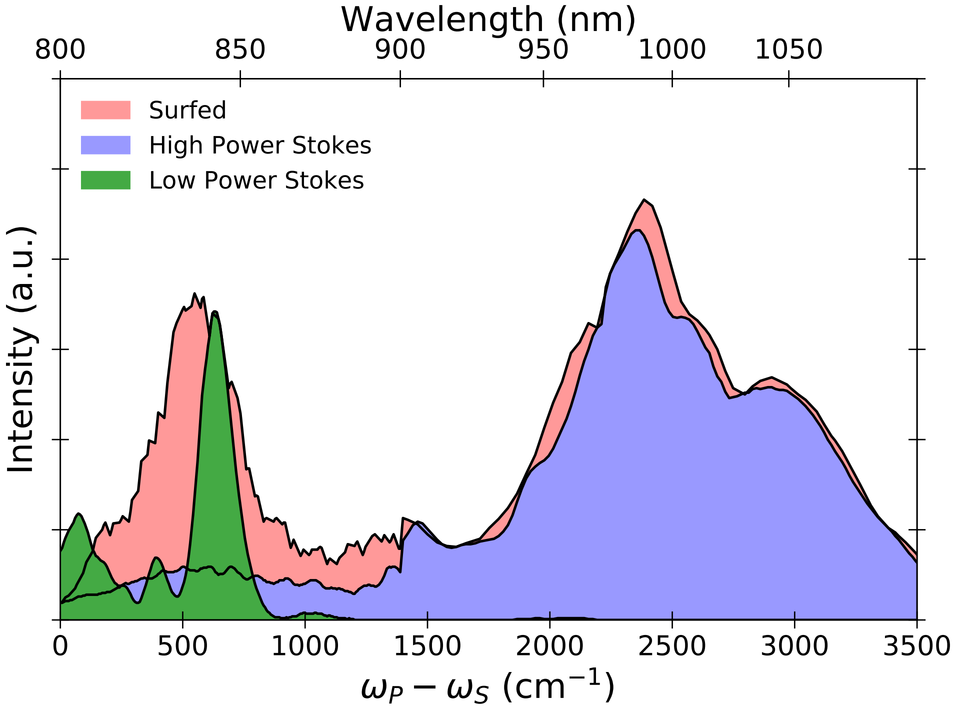

Figure 3.3: Stokes supercontinuum generated by “low” (37 mW, green) and “high” (220 mW, blue) PCF pump powers, and the overall trace of the power-tuning sequence representing the effective “surfed” spectrum (red). A video of the surfed supercontinuum can be found in a supplemental material of ref [1].

3.4.2 CARS hyperspectroscopy

We demonstrate the efficacy of spectral surfing vs. standard (or statically-powered PCF) CARS hyperspectroscopy using a sample mixture consisting of benzonitrile, DMSO, and a few strands of cellulose fibre as shown in Fig. 3.4. The use of a low PCF pump power generates Stokes that strongly stimulates the 670 cm^{-1} vibrational resonance of DMSO. The CARS image shows that DMSO is slightly concentrated around the cellulose fibre, but the strong non-resonant response of benzonitrile causes the poor contrast of DMSO. The supercontinuum generated with the low-powered condition is unable to efficiently stimulate lower and higher frequencies thus providing almost no contrast for chemically mapping benzonitrile. On the other hand, the use of a high PCF pump power generates Stokes that strongly stimulates higher vibrational resonances (> 2200 cm^{-1}) thus providing clear contrasts for benzonitrile at 2230 cm^{-1} and 3070 cm^{-1} and DMSO at 2910 cm^{-1}. The CARS image shows that DMSO clearly concentrates around the cellulose fibre. The difference in images obtained with the low and high powered condition is attributed to the strong influence of the NRB in the fingerprint region that results in decreased contrast. With spectral surfing, a dynamic supercontinuum is generated that can efficiently stimulate vibrational resonances across the spectrum. Bright CARS images of benzonitrile can be obtained from its 460 cm^{-1}, 2230 cm^{-1} and 3100 cm^{-1} resonances, and DMSO from its 670 cm^{-1} and 2910 cm^{-1} resonances. Thus, spectral surfing confers substantial advantage across a wide scan range over a statically-powered SF-CARS scan.

The hyperspectral data obtained with spectral surfing contains a wide range of frequencies which we can then use to generate chemical images with improved contrast. As shown in Fig. 3.4(a), the CARS image of DMSO (both low powered and

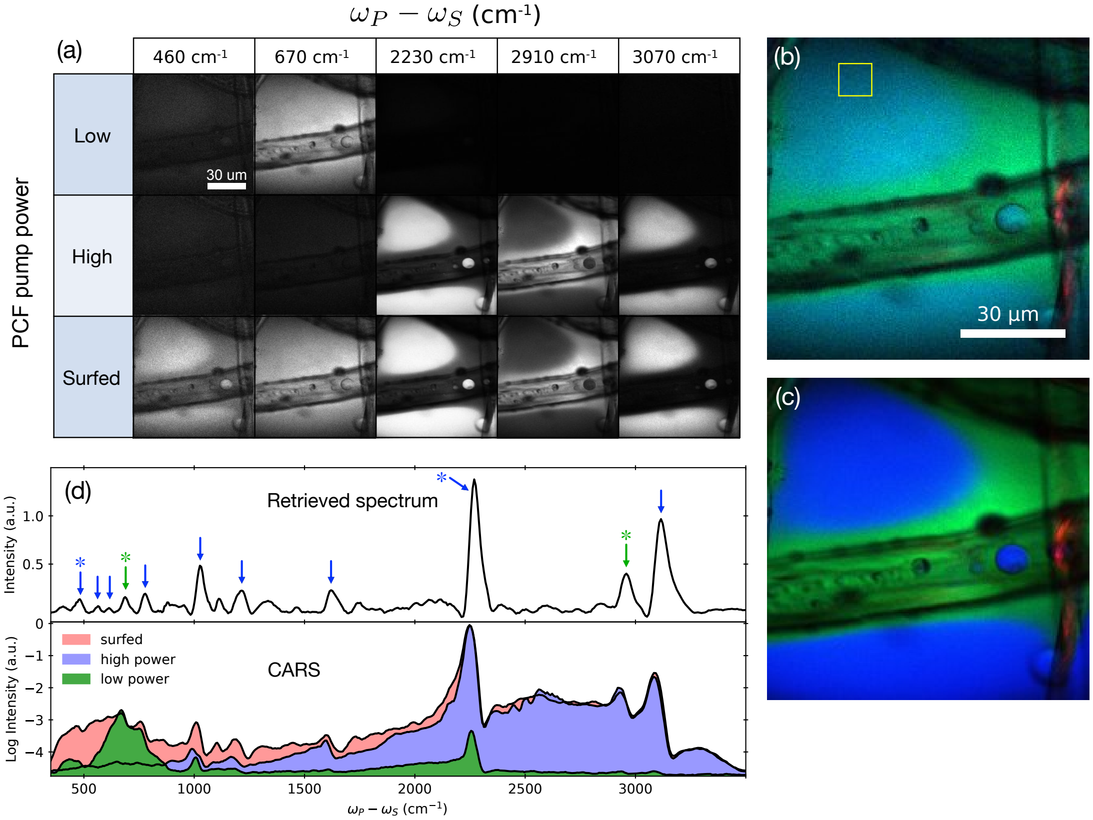

Figure 3.4: CARS hyperspectroscopy of benzonitrile and DMSO. CARS images and spectra under low-powered, high-powered and surfed conditions. (a) CARS images obtained at vibrational resonances corresponding to 460 cm^{-1}, 670 cm^{-1}, 2230 cm^{-1}, 2910 cm^{-1}, and 3070 cm^{-1} using low (37 mW) and high (220 mW) PCF pump powers, and with the spectrally surfed Stokes supercontinuum. For each column (frequency), the image display settings were normalized with respect to the surfed condition (bottom row). (b) Fingerprint multimodal CARS image of the benzonitrile, DMSO, and a cellulose fibre mixture obtained from the surfed hyperspectra of (a) with 460 cm^{-1} (blue, benzonitrile), 670 cm^{-1} (green, DMSO), and second-harmonic signal (red). (c) Silent-CH-based multimodal CARS image from the surfed 2230 cm^{-1} (blue, benzonitrile), 2910 cm^{-1} (green DMSO), and second-harmonic signal (red). (d) CARS spectra (rolling average of four spectral points, $\approx$ 20 cm^{-1}) obtained from the 20 $\times$ 20 pixel region of interest highlighted in (b), and the Raman-like retrieved spectra of the "surfed" condition. The arrows point to known peaks of benzonitrile (blue) and DMSO (red). The two lower-frequency arrows marked with asterisks designate the frequencies used to compose the image in (b) while two higher-frequency arrows were used to compose the image in (c). The pump powers used to collect the data was set to 50 mW (measuring $\approx$ 35 mW at the sample plane).

surfed) shows weak contrast at the 670 cm^{-1} resonance due to the strong non-resonant response from benzonitrile. However, merging the 670 cm^{-1} CARS image of DMSO with the 460 cm^{-1} CARS image of benzonitrile creates a contrasting chemical map (Fig. 3.4(b)) and is reflective of the chemical images obtained at the higher frequencies (Fig. 3.4(c)). In these images, the second-harmonic generation contrast from a cellulose fibre is also included and while not present in this particular sample, any two-photon excited fluorescence signals are also collected on a separate epi-detector. The CARS images shown in Fig. 3.4 are raw and unmodified; therefore, the chemical images can still be improved by processing the hyperspectral data through noise reduction and contrast enhancement techniques (see Appendix I). Image enhancement significantly improves the contrast of the CARS images obtained in the fingerprint frequencies and is consequently very similar to the CARS images obtained at higher frequencies (see Appendix I.3).

In these CARS scans, our use of fixed blocks of glass means that the chirps of the pump and Stokes pulses cannot be identically matched across the entire CARS spectrum. With the experimental conditions reported in Table 3.1, the chirps are most matched in the low-frequency region, and thus we find the spectral resolution (measured as the FWHM of the benzonitrile peaks) increasing steadily from 40 cm^{-1} deep in the fingerprint to 100 cm^{-1} at the OH frequencies. This implies a slight under-chirping of the Stokes at longer wavelengths or rather, having an over-chirped pump as discussed and shown in Table 3.1. A more judicious choice of glass block lengths and further optimization of laser conditions would significantly improve the spectral resolution of our system.

3.4.3 Reduced light exposure

In our static high-powered CARS scans, supercontinuum intensities can reach more than 100 mW just before it enters the microscope, and with the microscope having approximately a 70% transmission efficiency, the sample can be exposed to at least 70 mW of power from the supercontinuum alone. Not all spectral components of the supercontinuum, especially that of a broad supercontinuum generated with a high PCF pump power, are used to stimulate a vibrational resonance. Thus, doing wide frequency CARS scans with a high PCF pump power is not always efficient and may simply increase the risk of sample photodamage.

An advantage of spectral surfing is that it effectively reduces a sample's unnecessary exposure to intense laser light since it dynamically adjusts the PCF pump powers during a CARS scan. By ramping up the total Stokes (supercontinuum) power throughout a scan, lower net Stokes energy is incident on the sample compared to the typical static-Stokes approach. During the course of the CARS hyperspectral scan, a weaker, but more efficient, dose of Stokes supercontinuum is used in the fingerprint region. Upon reaching the CH/OH frequencies, a stronger supercontinuum is used, and the sample light exposure per unit time reaches the high power case. We can model the sample's (instantaneous) light exposure from the supercontinuum, $I_{\text{sample}}(t)$ (after filters) by the equation

$$I_{\text{sample}}(t) = \int I_S(\omega_S, t) d\omega_S \tag{3.1}$$

where the overall light exposure can be found by integrating Eq. (3.1) over time. Figure 3.5 shows the Stokes exposure of the sample with and without spectral surfing.

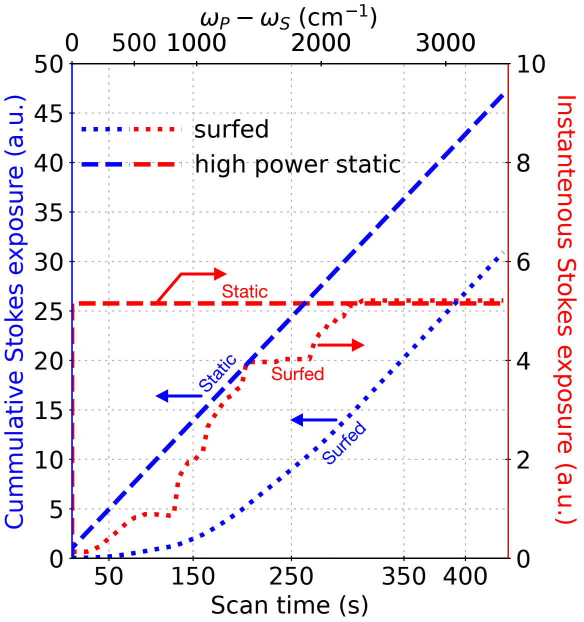

Figure 3.5: Sample exposure versus hyperspectral scan time. The blue curves are cumulative exposure, calculated by integrating the overall instantaneous spectral intensity of the Stokes supercontinuum (red curves) with respect to scan time.

With a standard high-power static CARS scan, the instantaneous light exposure is constant, and the overall light exposure grows linearly over time. Whereas for a surfed CARS scan, the instantaneous light exposure is dynamic and the overall light exposure becomes linear as the scan approaches frequencies around 1500 cm^{-1} where the PCF pump power is almost maximum.[2] With regards to light exposure, spectral-surfing becomes very advantageous when used for scanning in the fingerprint. As shown in Fig. 3.5, the cumulative light exposure with spectral surfing is significantly lower than the high-power static case—less than a third when scanning at frequencies below 1500 cm^{-1} and just to two-thirds when scanning over the 3500 cm^{-1} span.

3.5 Summary and conclusion

With the use of dispersed and power-tuned PCF pump pulses, a supercontinuum generating PCF module such as the FemtoWHITE CARS, which is mostly designed for silent-to-CH/OH CARS microscopy, can be used for broadband, fingerprint-to-CH/OH SF-CARS. The performance of such PCFs for use in CARS microscopy can be further enhanced by generating a dynamic Stokes supercontinuum to strongly probe a vibrational resonance—a technique which we call spectral surfing. With spectral surfing, the CARS signal and contrast are improved across the 350 cm^{-1} up to 3500 cm^{-1} frequency span. Furthermore, this method is compatible with available Raman retrieval algorithms that allow for quantitative hyperspectral analysis relevant

---

[2] A difference frequency, $\omega_P - \omega_S$, of 1500 cm^{-1} corresponds to a Stokes wavelength of 910 nm and is near the 945 nm ZDW of the FemtoWHITE CARS. With increasing PCF pump power, the spectral maximum of the Stokes supercontinuum reaches close to the 945 nm ZDW. Further increasing the PCF pump power results in an immediate spectral broadening as if the PCF is pumped with transform-limited pulses yielding a supercontinuum devoid of spectral power in the ADR.

in materials science and biomedical imaging. Finally, spectral surfing permits the use of weaker but optimal laser intensities—an attribute that is important for low-light dosage applications such as live cell microscopy. While we have demonstrated the application of spectral surfing within the context of SF-CARS microscopy, the technique may find future applications in related four-wave mixing techniques and other time-gated methods such as *optical coherent tomography.*

References

1. Porquez, J. G., Cole, R. A., Tabarangao, J. T. & Slepkov, A. D. Brighter CARS hypermicroscopy via "spectral surfing" of a Stokes supercontinuum. *Optics Letters* **42,** 2255 (2017).
2. Porquez, J. G., Korfanty, E. R. & Slepkov, A. D. Ultra-broadband coherent anti-Stokes Raman scattering microscopy with a dynamically power-tuned Stokes supercontinuum. *Proc. SPIE* **10069,** 1–10 (2017).
3. Porquez, J. G., Tabarangao, J. T., Cole, R. A. & Slepkov, A. *Brighter CARS hypermicroscopy via "spectral surfing"* in *2017 Photonics North, PN 2017* (2017).
4. Porquez, J. G., Cole, R. A., Tabarangao, J. T. & Slepkov, A. D. Spectrally-broad coherent anti-Stokes Raman scattering hyper-microscopy utilizing a Stokes supercontinuum pumped at 800 nm. *Biomedical Optics Express* **7,** 4335 (2016).
5. Dudley, J. M., Genty, G. & Coen, S. Supercontinuum generation in photonic crystal fiber. *Reviews of Modern Physics* **78,** 1135–1184 (2006).
6. Pegoraro, A. F., Slepkov, A. D., Ridsdale, A., Moffatt, D. J. & Stolow, A. Hyperspectral multimodal CARS microscopy in the fingerprint region. *Journal of Biophotonics* **7,** 49–58 (2014).

7. Hilligsøe, K. M. *et al.* Supercontinuum generation in a photonic crystal fiber with two zero dispersion wavelengths. *Optics Express* **12,** 1045 (2004).
8. König, K., So, P. T. C., Mantulin, W. W. & Gratton, E. Cellular response to near-infrared femtosecond laser pulses in two-photon microscopes. *Optics Letters* **22,** 135 (1997).
9. König, K., Becker, T. W., Fischer, P., Riemann, I. & Halbhuber, K.-J. Pulse-length dependence of cellular response to intense near-infrared laser pulses in multiphoton microscopes. *Optics Letters* **24,** 113 (1999).
10. Cui, M., Bachler, B. R. & Ogilvie, J. P. Comparing coherent and spontaneous Raman scattering under biological imaging conditions. *Optics letters* **34,** 773–775 (2009).
11. Galli, R. *et al.* Intrinsic Indicator of Photodamage during Label-Free Multiphoton Microscopy of Cells and Tissues. *PLoS ONE* **9** (ed Aegerter, C. M.) e110295 (2014).
12. Arkhipov, S. N., Saytashev, I. & Dantus, M. Intravital Imaging Study on Photodamage Produced by Femtosecond Near-infrared Laser Pulses in Vivo. *Photochemistry and Photobiology* **92,** 308–313 (2016).
13. Andresen, E. R., Birkedal, V., Thøgersen, J. & Keiding, S. R. Tunable light source for coherent anti-Stokes Raman scattering microspectroscopy based on the soliton self-frequency shift. *Optics Letters* **31,** 1328 (2006).
14. Camp Jr, C. H. *et al.* High-speed coherent Raman fingerprint imaging of biological tissues. *Nature Photonics* **8,** 627–634 (2014).

15. Cheng, J.-X., Volkmer, A., Book, L. D. & Xie, X. S. Multiplex Coherent Anti-Stokes Raman Scattering Microspectroscopy and Study of Lipid Vesicles. *The Journal of Physical Chemistry B* **106,** 8493–8498 (2002).

16. Knutsen, K. P., Johnson, J. C., Miller, A. E., Petersen, P. B. & Saykally, R. J. High spectral resolution multiplex CARS spectroscopy using chirped pulses. *Chemical Physics Letters* **387,** 436–441 (2004).

Chapter 4

Search for improved laser sources for SF-CARS

4.1 Chapter preface

In the previous chapter I described a technique called spectral surfing in which we use the power-dependence of the supercontinuum to yield brighter CARS signals. We demonstrated spectral surfing with a specific commercially-available PCF module called FemtoWHITE CARS. The FemtoWHITE CARS has its particular strengths, but other PCFs exist which might also prove useful for SF-CARS. This chapter compares the performance of this module with another, the FemtoWHITE 800, for use in SF-CARS through spectroscopy and imaging. I then investigate opportunities for spectral surfing of the FemtoWHITE 800, and study power-dependent polarization properties of the supercontinua generated by these modules to explain differences in their resulting CARS spectra. Finally, I give a discussion on the recommended use of each PCF module for SF-CARS microscopy.

This chapter is based on work we published in OSA Continuum [1], but with additional insights on the polarization behaviour of the fibres.

4.2 Introduction

The FemtoWHITE CARS PCF module has proven very useful for broadband hyperspectral SF-CARS microscopy [2–4]. The spectral shape of its supercontinuum can be manipulated by dispersion and dynamic power-tuning schemes, extending its performance beyond its commercial specifications for CH/OH-based CARS imaging.

Aside from the FemtoWHITE CARS, numerous other supercontinuum generating fibres exist that might show potential for brighter and broader frequency access for a PCF-based CARS microscope system. Unfortunately, most of these fibres are proprietary and unavailable commercially. Some of these fibres are custom-manufactured by research labs equipped with fibre fabrication facilities [5] or obtained through collaboration[1] [6]. One supercontinuum-generating fibre that is available commercially is the FemtoWHITE 800. This fibre was released by NKT Photonics contemporaneously with their FemtoWHITE CARS, and comes in the same module packaging, thus making the two ideal for comparisons. We have obtained a FemtoWHITE 800 module on loan from collaborators at the NRC, and next describe its operation in our SF-CARS system.

---

[1] We have also obtained several other microstructured fibres through a collaborator in Austria, though in bare, un-cased form. These are currently being studied by others in our lab.

4.2.1 Features of the FemtoWHITE 800 and the FemtoWHITE CARS

The FemtoWHITE 800 is a PCF module that is very similar to the FemtoWHITE CARS. The FemtoWHITE 800 is also designed for 800-nm pumping and is also manufactured in a 12-cm fused-edge module for easy fibre coupling. Within the module is a polarization-maintaining fibre, *NL-PM-750*, with a lower ZDW at 750 nm and an upper ZDW at 1260 nm (an ADR of 750 nm – 1260 nm). The use of this module for CARS predates that of the FemtoWHITE CARS, finding particular use in the multiplex CARS microscopy approach [7].

Due to the considerable differences in the GVD curves of the FemtoWHITE 800 and the FemtoWHITE CARS, the supercontinua generated by these fibres are very different. When pumped at 800 nm with strong enough powers (e.g., >100 mW, 150 fs pump duration), the FemtoWHITE 800 generates a relatively “flat” supercontinuum spanning 600 nm to 1200 nm [8, 9]—an advantage for CARS spectroscopy since it makes it easier to separate real resonance peaks from artifacts coming from a spectrally “wavy” Stokes supercontinuum.[2] Further increasing the PCF pump power largely increases the spectral intensity across the same supercontinuum, with minimal additional spectral broadening. Thus, maximizing the Stokes intensity can be done by maximizing the PCF seed power, although subject to noise considerations and the damage thresholds of the fibre module. That is, pumping with large powers (e.g., >300 mW, 150 fs pulses) may cause intensity fluctuations in the supercontinuum or damage the module. By comparison, The FemtoWHITE CARS, having closely-lying

---

[2] Since $I_{AS}(\omega_{AS}) \propto I_S(\omega_S)$, when $I_S(\omega_S)$ consists of peaks and troughs (or wavy), peaks in the anti-Stokes spectrum can be obscured by the Stokes.

ZDWs, can generate wavelengths within its ADR when weakly pumped, but when pumped with higher powers the supercontinuum quicly broadens beyond its ADR [10, 11] and the red-shifted portion of the supercontinuum becomes strongest near 1050 nm. The abundance of power at 1050 nm matches well with an 800 nm pump to provide strong anti-Stokes signals at the CH-stretch frequencies[7, 12–15], thus motivating its marketing as FemtoWHITE CARS.

Both the FemtoWHITE CARS and the FemtoWHITE 800 can be used to demonstrate broadband CARS hyperspectroscopy that can reach into the fingerprint frequencies. In the last chapter, I demonstrated that spectral surfing extends the spectral access of the FemtoWHITE CARS, reaching as low as 350 cm^{-1} [4]. On the other hand, Lee *et al.* used the FemtoWHITE 800 to demonstrate multiplex CARS spectroscopy capable of reaching $\approx$ 600 cm^{-1} [7]. However, using the FemtoWHITE 800 for broadband SF-CARS has not been previously demonstrated. Conversely, the use of FemtoWHITE CARS for broadband multiplex CARS has also not been demonstrated.

The comparison of the performance of both fibre modules, through hyperspectral imaging, may suggest which of these widely available fibres may be more suitable for use in broadband hyperspectral SF-CARS microscopy. Furthermore, the results in this work may prove useful for research groups planning to use the same or similar supercontinuum generating fibres either for vibrational imaging or another purpose altogether.

4.2.2 Previous works

The comparison of the FemtoWHITE CARS and the FemtoWHITE 800 for CARS microscopy is not entirely novel. Two previous studies were already done—an article by Naji *et al.* [16] and a conference proceeding by our group [8]. The study by Naji *et al.* [16] compared these fibres with the aim of reducing noise in supercontinuum generation manifesting at the pulse rate of the laser (usually tens of MHz), and then use the "noise-reduced" supercontinuum of the FemtoWHITE 800 for CARS imaging. Unless the supercontinuum generated is exceptionally noisy and weak, noise at this frequency does not seem to significantly interfere with the formation of CARS images since CARS imaging is typically done with microsecond pixel dwell times (sub-MHz). Pixels forming a CARS image are generated from hundreds of nonlinearly interacting pump pulses (see Table 4.1); thus, high-frequency noise from the supercontinuum is averaged out. Although Naji *et al.* demonstrated SF-CARS spectroscopy [16] (unclear which fibre module was used), CARS imaging was done using a wavelength-filtered Stokes—a vastly different approach to the more efficient Stokes use of SF-CARS. Therefore, they were unable to demonstrate SF-CARS hyperspectroscopy using either fibre module. Our previous work, on the other hand, focused on the preliminary underpinnings of spectral surfing [8]. We were not able to demonstrate hyperspectral SF-CARS imaging using the FemtoWHITE 800 as we focused on investigating the supercontinuum spectra as a function of PCF pump power from both fibre modules.

In this chapter, we compare the performance of both FemtoWHITE CARS and the FemtoWHITE 800 through non-resonant four-wave mixing in glass, CARS spectroscopy of benzonitrile, and CARS hyperspectroscopy of pharmaceutical drugs. Due to observed complexities in the CARS spectrum obtained using the FemtoWHITE

pixel dwell time (μs)	# of pulses
1	80
10	800
50	4000
100	8000
300	24000

Table 4.1: Nominal laser pulses used to generate CARS signals with an 80 MHz oscillator.

800, polarization studies were performed showing the generation of a time-delayed supercontinuum duplicate or "dual-solitons." Finally, we suggest optimized uses of each fibre module for SF-CARS and demonstrate SF-CARS hyperspectroscopy using both FemtoWHITE 800 and FemtoWHITE CARS.

4.3 Experiment

Comparing the performance of the two fibre modules requires the implementation of experiments having identical conditions, e.g., fibre coupling efficiency, PCF pump power, chirp-matching condition. However, this can only be attained to a certain degree. To achieve close to identical experimental conditions for both fibre modules, we have built a mounting setup adjacent to the FemtoWHITE CARS. Flip mirrors were used to alternately route the pump and the PCF pump beam between the FemtoWHITE CARS and the FemtoWHITE 800 as shown in Fig. 4.1. Routing the PCF pump beam to the FemtoWHITE 800, which has a longer path length than the FemtoWHITE CARS, also requires rerouting the pump beam to traverse a similarly long path. Similar objectives (Newport M-40×) were used to couple the PCF pump beams into the fibre modules, but different collimators were used—a Mitutoyo M

Plan NIR 50× [17] is used for the FemtoWHITE CARS, while a Newport M-20× [18] is used for the FemtoWHITE 800.

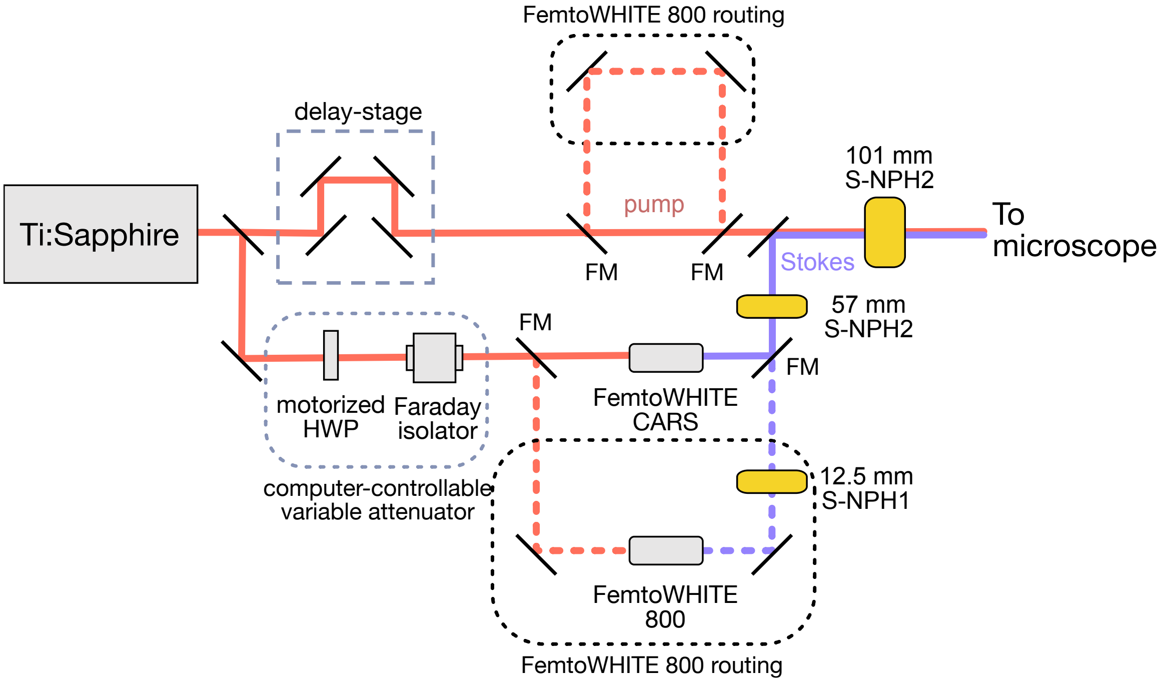

Figure 4.1: Fibre routing setup. Flip mirrors (FM) are used to route the pump and Stokes beams for use either in the FemtoWHITE CARS or the FemtoWHITE 800. Dashed lines represent alternate beam routes. The setup is a slight modification of the setup in Fig. 3.1.

The chirps of the Stokes generated by each fibre module were matched by placing appropriate lengths of high-dispersion glass after the fibres. When using the FemtoWHITE CARS, similar to my earlier work [2] (or in chapter 2), the Stokes supercontinuum generated by the FemtoWHITE CARS is chirped using a total of 158 mm of high-dispersion glass (Ohara, SNPH-2). When using the FemtoWHITE 800, the Stokes supercontinuum generated by the FemtoWHITE 800 is chirped using the same 158 mm of SNPH-2 but with additional 12.5 mm of high-dispersion glass (Ohara, SNPH-1). The added dispersion compensates for the FemtoWHITE 800's highly negative dispersion profile across its ADR [9]. The combined blocks of high-dispersion glass and the remaining optical elements effectively lengthens the duration of the red-shifted portion of the supercontinuum generated by both the FemtoWHITE CARS and the FemtoWHITE 800 to more than 20 ps at the sample location. The pump beam is chirped using a total of 101 mm of high-dispersion glass (Ohara, SNPH-2) regardless which fibre module is used.

The samples used in this work are a glass coverslip (to demonstrate non-resonant FWM and the effectiveness of spectral surfing on both fibre modules), benzonitrile (for CARS spectroscopy), and a Tylenol pill (for CARS hyperspectral imaging). The pump power was set to approximately 300 mW ($\approx$ 225 mW at the sample plane) when measuring the FWM spectrum from glass, and approximately 20 mW ($\approx$ 15 mW at the sample plane) for benzonitrile and Tylenol experiments. The PCF pump power used to generate the Stokes for spectral surfing was varied from 0 mW to 300 mW by a computer-controlled half-wave plate and polarizer pair acting as a variable attenuator for spectral surfing. Additionally, a CARS spectrogram of benzonitrile was obtained by using a spectrometer in place of a PMT. The hyperspectral image stacks were processed using software I coded in Python [19] (and have since made freely available), and with ImageJ [20]. Noise reduction was performed by applying an Anscombe transform and singular value decomposition on the hyperspectral image stack [21] (see Appendix I for more information on image processing).

The polarization spectrum of the Stokes supercontinuum is characterized in the microscope by rotating a polarizer (Thorlabs LPNIRE-100-B) placed after the sample location in 5° increments, where the resulting polarized Stokes is routed to a spectrometer (StellarNet BLACK Comet CXR SR-50).

4.4 Results and discussions

The performance of each fibre are examined by generating the anti-Stokes using three different methods: non-resonant four-wave mixing spectroscopy, CARS spectroscopy, and CARS hyperspectral imaging. The results from each of these methods collectively provide insight for the effective use of each fibre for broadband SF-CARS.

4.4.1 Measuring the performance of each fibre for SF-CARS through non-resonant four-wave mixing

We use non-resonant four-wave-mixing [22] to measure the efficiency of CARS excitation throughout the vibrational spectrum. Glass is chosen as the sample because it demonstrates a relatively uniform electronic hyperpolarizability, i.e., $\chi^{(3)} \approx \chi_{NR} \approx$ constant, and does not have strong vibrational resonances over the scan range. In terms of the CARS-relevant fields, we can write the four-wave mixing signal as (Eq. (1.9))

$$I_{AS}(2\omega_P - \omega_S) \propto |\chi^{(3)}|^2 I_P^2(\omega_P) I_S(\omega_S) \tag{4.1}$$

where $\chi^{(3)}$ is the third-order electronic susceptibility containing both vibrationally-resonant $\chi_R^{(3)}$ and non-resonant $\chi_{NR}^{(3)}$ contributions, and $I_P(\omega_P)$ and $I_S(\omega_S)$ are the pump and Stokes intensities (frequencies), respectively. The signal intensity depends linearly on the Stokes intensity; thus, with an essentially non-varying Gaussian pump, the FWM spectrum reflects the shape of the Stokes [22].

Non-resonant four-wave mixing with the FemtoWHITE CARS

Figure 4.2 shows the strength and shape of FWM spectroscopy in glass obtained from each of the fibre modules at three different PCF pumping conditions: 160 mW (moderate power), 300 mW (high power), and with spectral surfing. In line with results shown in Chapter 3, and as shown in Fig. 4.2(a), pumping the FemtoWHITE CARS with lower powers gives better access to lower fingerprint frequencies; pumping with higher powers gives access to silent-CH/OH frequencies; spectral surfing gives substantial access across the 500 cm^{-1} to 3500 cm^{-1} frequency range. Statically pumping the PCF cannot provide a sufficiently strong Stokes that can span the fingerprint-to-CH/OH region. Thus, the results confirm the advantage of using spectral surfing with the FemtoWHITE CARS.

Non-resonant four-wave mixing with the FemtoWHITE 800

The PCF pump power dependence of the FemtoWHITE 800 is fundamentally different from that of the FemtoWHITE CARS as shown in Figs. 4.2(b). Just as reported in previous works [8, 16], increasing the PCF pump power for the FemtoWHITE 800 generates supercontinuum with gradually increasing spectral strength across the vibrational spectrum. Unlike the FemtoWHITE CARS, there is little advantage in implementing spectral surfing with the FemtoWHITE 800. This is made clear in Fig. 4.2(d), where the ratio of the FWM signal under the surfed condition to that of the high power condition is essentially unity for frequencies above 500 cm^{-1}, in other

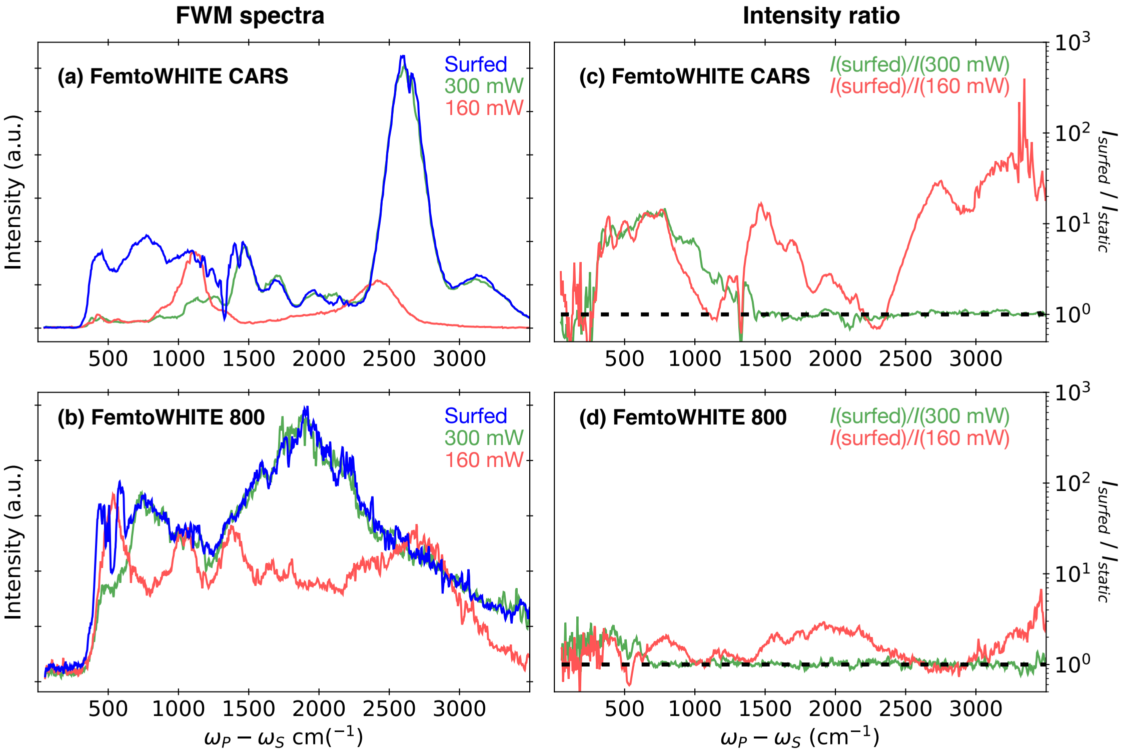

Figure 4.2: Non-resonant FWM from a glass coverslip at three different incident PCF pump power conditions: moderate power (160 mW), high power (300 mW) and swept (surfed). (a) FWM using the FemtoWHITE CARS and (b) using the FemtoWHITE 800. (c) Ratio of surfed-to-static FWM from FemtoWHITE CARS and (d) from FemtoWHITE 800. Unity ratio is shown as a dashed black line.

words, the FWM intensity is approximately equal for both the surfed and high power condition.

4.4.2 Measuring the performance of each fibre through CARS spectroscopy

Ultimately, the performance of each fibre module for SF-CARS applications must be measured through CARS spectroscopy with emphasis on the spectral quality of resonance peaks, e.g., spectral resolution and the capability of each fibre module to stimulate resonances across the vibrational spectrum. For this, benzonitrile was used as reference material as it contains strong multiple resonance peaks as low as 460 cm^{-1} in the fingerprint and up to 3070 cm^{-1} the CH/OH frequencies.

CARS spectra with the FemtoWHITE CARS

Figure 4.3(a) shows the CARS spectrum of benzonitrile using the FemtoWHITE CARS. With the high power condition (300 mW), a supercontinuum is generated where various resonances ranging from 1000 cm^{-1} to 3100 cm^{-1} are stimulated. With a moderate power condition (160 mW), the 1599 cm^{-1} resonance shows a strong peak while resonances as low as 460 cm^{-1} show as weaker peaks and are mostly buried by the non-resonant background. With spectral surfing, resonances across the spectrum are stimulated with greater strength resulting in clear, observable peaks from the deep fingerprint resonances at 460 cm^{-1} and 760 cm^{-1}. The spectral widths of the resonances at 1000 cm^{-1}, 2230 cm^{-1}, and 3070 cm^{-1} were found to be 35 cm^{-1}, 35 cm^{-1}, and 60 cm^{-1}, respectively. In comparison, spontaneous Raman peak widths for this sample, are approximately 9 cm^{-1}, 13 cm^{-1}, and 15 cm^{-1}. The large FWHM from CARS arises from the spectral reshaping due to the non-resonant FWM. Furthermore, differences in spectral resolution in each frequency region arise from non-uniform chirp matching and higher-order dispersion effects across the supercontinuum [23, 24].

CARS spectra with the FemtoWHITE 800

The supercontinuum generated by the FemtoWHITE 800, on the other hand, can easily cover a wide range of the vibrational spectrum without the need for spectral surfing as shown in two differently pumped configurations (Figs. 4.3(b,c))—a feature

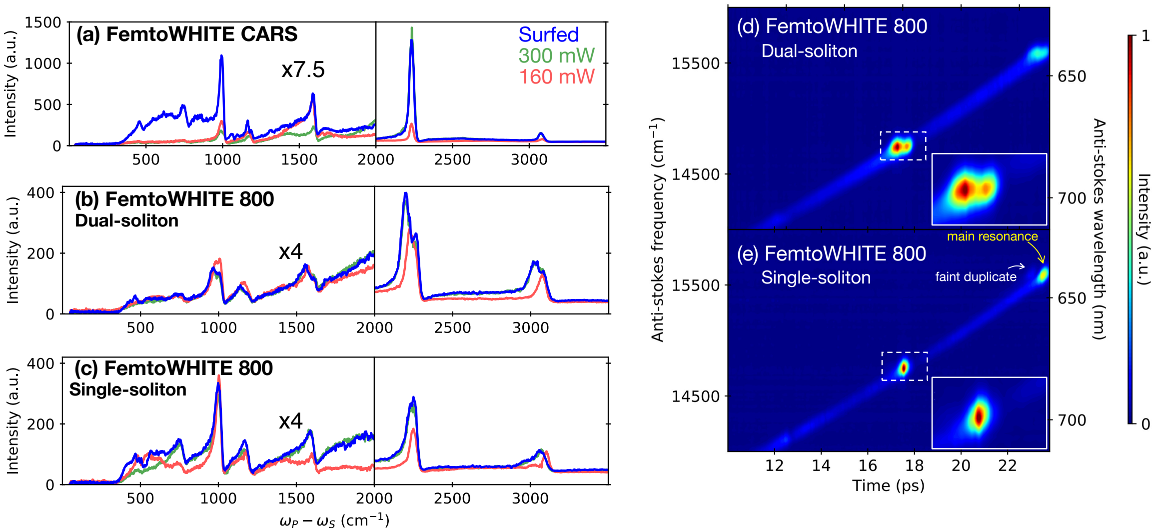

Figure 4.3: SF-CARS spectroscopy of benzonitrile with Stokes supercontinuum generated by the FemtoWHITE CARS and FemtoWHITE 800. (a) CARS spectrum obtained using the FemtoWHITE CARS, (b) the FemtoWHITE 800 with dual-soliton when pumped away from the fibre (slow) axis, and (c) the FemtoWHITE 800 with single-soliton when pumped along the (slow) polarization axis. In (a)-(c) three incident PCF pump power conditions are presented: 160 mW (red); 300 mW (green), and spectral surfing (blue). For clarity of display, the CARS spectra have different vertical scaling below and above 2000 cm^{-1}. While (a)–(c) are of the same units, the intensity scale cannot be used as a direct comparison between plots due to slight imperfections in the alignment of the optics. (d) When the FemtoWHITE 800 is pumped with polarization away from the slow axis of the fibre, the anti-Stokes spectrogram from benzonitrile shows the appearance of dual-solitons separated in time; emphasized at the 2230 cm^{-1} CARS resonance (anti-Stokes frequency of 14730 cm^{-1}). (e) When the FemtoWHITE 800 is pumped with a polarization along the slow axis of the fibre, the anti-Stokes spectrogram from benzonitrile shows that the dual-soliton shown in (d) is nearly extinguished. The inset shows the magnified 2230 cm^{-1} resonance. Both (d,e) are pumped with 300 mW of PCF power.

that has led to its adoption for multiplex-CARS applications [7, 14, 25–28]. Furthermore, the polarization-maintaining aspect of this fibre module enables the generation of a relatively stable supercontinuum [29]. However, careful thought must be given when pumping this fibre module for SF-CARS. As shown in Fig. 4.3(b), a noticeable degradation in the CARS spectrum can be observed as compared to the CARS spectrum in Fig. 4.3(c). For example, the 2230 cm^{-1} and the 3070 cm^{-1} resonances of benzonitrile appear wider and wayward peak-doubling is observed. The CARS spectrum of Fig. 4.3(b) was obtained when the polarization of the PCF pump was set at an angle that is between the two main polarization axes of the fibre while the CARS spectrum in Fig. 4.3(c) was obtained when the PCF pump polarization was set parallel to the slow axis of the fibre. From these results, it would appear that the polarization-maintaining aspect of this fibre can be detrimental for SF-CARS when the fibre is pumped in between its two main polarization axes. Furthermore, we found that the appearance of peak doubling becomes more prominent with increased PCF pump powers. I explain the source of this artifact next.

4.4.3 The dual-soliton from the FemtoWHITE 800

Using a CARS spectrogram, I investigate the cause of peak doubling in the SF-CARS spectrum generated with the FemtoWHITE 800. The spectrogram converts to the corresponding CARS spectrum when integrated over its frequency axis. As shown in Fig. 4.3(d), the CARS spectrogram shows clear doubling of the 2230 cm^{-1} ($\omega_{AS} = 14730$ cm^{-1}) resonance of benzonitrile. This doubling is presumably caused by a weaker supercontinuum duplicate that is separated by approximately 400 fs (≈ 35 cm^{-1} in frequency) with respect to the main supercontinuum. Recent work has referred to the supercontinuum doubling in highly-birefringent polarization-maintaining PCFs as "dual-soliton generation" [30–32]. Dual-soliton generation in the FemtoWHITE 800 is similar to what was observed by Chen *et al.* [31, 32], albeit with a different PCF designed for 1060 nm pumping. Chen *et al.* used the presence of the dual-solitons, separated in time by more than a picosecond, to perform a background subtraction method for multiplex CARS applications. The solitons generated by FemtoWHITE 800 in our current experimental conditions are not as distinctly separated ($\approx$ 400 fs, 130 μm path length difference) to be applicable for background subtraction methods such as in dual-soliton CARS [31] or differential CARS [33–35]. Due to its close separation, the advantages of having dual-soliton spectra that exist for multiplex-CARS becomes a hindrance for SF-CARS since it "degrades" the observed CARS spectrum. In order for the FemtoWHITE 800 to be useful for SF-CARS, the generation of the secondary soliton should be minimized or eliminated.

4.4.4 Minimizing dual-soliton generation in the FemtoWHITE 800

We find that dual-solitons are generated when the FemtoWHITE 800 is pumped with a beam polarized at an angle in between the two main polarization axes of the fibre. However, by pumping the FemtoWHITE 800 with a beam polarized along the slow axis as shown in Fig. 4.3(e) (single-soliton condition), the generation of the secondary soliton is almost eliminated. In comparison to 4.3(d), the FWM curve in 4.3(e) is noticeably thinner although an anti-Stokes duplicate can still be found at the 15570 cm^{-1} frequency ($\omega_P - \omega_S$ = 3070 cm^{-1}). The remnant secondary soliton may most likely be caused by unintentional birefringence that exists within the fibre due to manufacturing imperfections. As shown in Fig. 4.3(c), the CARS spectrum of benzonitrile is improved under the single-soliton condition and most of the double-peaks seen in Fig. 4.3(b) are eliminated. Another way to minimize the generation of the secondary soliton is through the use of weaker PCF pump powers, as shown in the CARS spectrum Fig. 4.3(c). Nonetheless, a comparison with the CARS spectrum obtained with the FemtoWHITE CARS under spectral surfing conditions suggests that using the FemtoWHITE CARS yields a brighter and better-resolved CARS spectrum across the entire fingerprint-to-CH vibrational frequency range.

4.5 Polarization spectra of supercontinuum generated from the FemtoWHITE CARS and FemtoWHITE 800

4.5.1 Polarization spectra of the FemtoWHITE CARS

By investigating the supercontinuum polarization spectra of both fibre modules, we found additional insights with regards to the unwanted effects of the dual-solitons. In this section, I first discuss the polarization spectra of supercontinua generated by the FemtoWHITE CARS and then that of the polarization-maintaining FemtoWHITE 800.

Figure 4.4 shows the intensity and polarization spectra of the FemtoWHITE CARS for low (35 mW incident) and moderate (220 mW incident) PCF pump powers. With a low PCF pump power, a strong soliton is generated at 815 nm – 830 nm which contains that vast majority of the spectral power while a weaker secondary soliton is

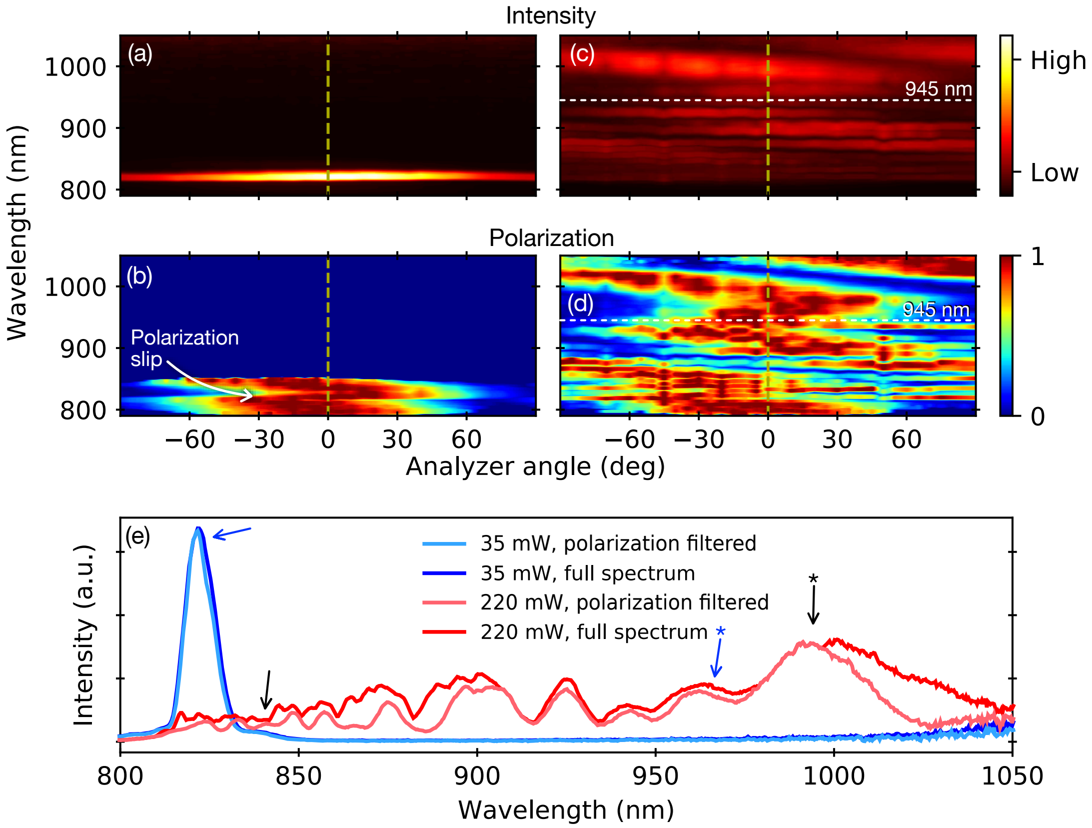

Figure 4.4: Polarization-dependent spectral intensity of the supercontinuum output from the FemtoWHITE CARS with low and moderate PCF pump powers. (a) The raw spectral-intensity polarization map of the supercontinuum with a low incident PCF pump power (35 mW). (b) Supercontinuum polarization intensity map obtained by normalizing (a) at each wavelength to highlight the polarization state. (c) The raw spectral-intensity polarization map of the supercontinuum with a moderate incident PCF pump power (220 mW). (d) Supercontinuum polarization intensity map obtained by normalizing (c) at each wavelength to highlight the polarization state. (e) The raw and polarized supercontinuum from FemtoWHITE CARS at the two power conditions. The polarization angle is set to 0°, as denoted along the dashed lines in (a)–(d). Arrows, without asterisks, indicate the location of the two solitons generated with a low PCF pump condition while those with asterisks indicate the location of the same but “evolved” solitons generated with a moderate PCF pump condition.

generated at 840 nm – 850 nm (Fig. 4.4(a,e)). Note that these solitons are not the same "dual-solitons" as discussed earlier from the FemtoWHITE 800. Instead, these are limited supercontinua generated within the ADR of the fibre. The polarization spectrum (Fig. 4.4(b)), constructed by normalizing the spectrum at each wavelength (i.e., along the horizontal axis), shows that the solitons are co-polarized but are separated by a polarization slip. The cause of the polarization slip is not yet known. With a moderate PCF pump power, the soliton that was once generated with the weaker pump condition have moved to the vicinity of the 945 nm ZDW while retaining their polarization character (Fig. 4.4(b,d)). As shown in Fig. 4.4(e), the previously weak soliton has become stronger in intensity while, conversely, the previously strong soliton has become weaker in intensity. Below the 945-nm ZDW, weak solitons are generated displaying chaotic polarization behavior (Fig. 4.4(d)). Therefore it seems that with higher PCF pump powers, the FemtoWHITE CARS generates unstable solitons below 945 nm and a relatively more "stable" supercontinuum beyond its 945 ZDW.

The moderately pumped FemtoWHITE CARS basically generates an unpolarized Stokes supercontinuum. Because the FemtoWHITE CARS is non-birefringent, the supercontinuum does not separate into orthogonal components as it propagates along the length of the fibre. However, the use of an unpolarized Stokes supercontinuum for SF-CARS spectroscopy, coupled with highly birefringent optical elements in the microscope system, may split the supercontinuum into time-delayed orthogonal components and thus result in an unwanted degradation in obtained CARS spectra—an effect similar to that caused by dual-solitons. Therefore, the use of a broadband polarizer located just after the FemtoWHITE CARS to polarize the supercontinuum should effectively eliminate the problem of having split-supercontinua, improving the spectral resolution of an SF-CARS scan. The effects of using a polarizer on the spectrum of the Stokes is shown in Fig. 4.4(e). When pumping the FemtoWHITE CARS with higher powers, a broadband polarizer oriented at zero degrees[3] causes significant spectral attenuation and reshaping of the supercontinuum. Despite this attenuation, as demonstrated in the next sections, the polarized supercontinuum remains sufficiently bright for CARS and FWM applications across a wide frequency range.

4.5.2 Polarization spectra of the FemtoWHITE 800

Figure 4.5 shows the intensity and polarization spectra of the polarization-maintaining FemtoWHITE 800 for low (35 mW) and moderate (220 mW) PCF pump powers. By comparison to the FemtoWHITE CARS, the supercontinuum generated by the FemtoWHITE 800 is mostly polarized (closely follows Malus' Law). With a low incident PCF pump power, the supercontinuum, while not extensive, is uniformly polarized as shown in Figs. 4.5(a,b). With a moderate PCF pump power, the spectrum is mostly uniformly polarized although a sharp polarization slip is observed at 820 nm – 830 nm (Fig. 4.5(d)) and higher wavelengths tend to show a slight shifting away from the initial polarization state. Because of the polarization shift, the higher wavelengths of the supercontinuum are susceptible to the large birefringence of the fibre module and are thus separated in time leading to the creation of the aforementioned dual-solitons. This then results to a perceived peak doubling in higher frequencies at the CH/OH region as shown in the generally single-solitonic CARS spectrum and spectrogram of

---

[3] The choice of reference angle for the polarizer is arbitrary. For simplicity, we choose 0° as the angle that matches the peak intensity, as shown in Figures 4.4 and 4.5.

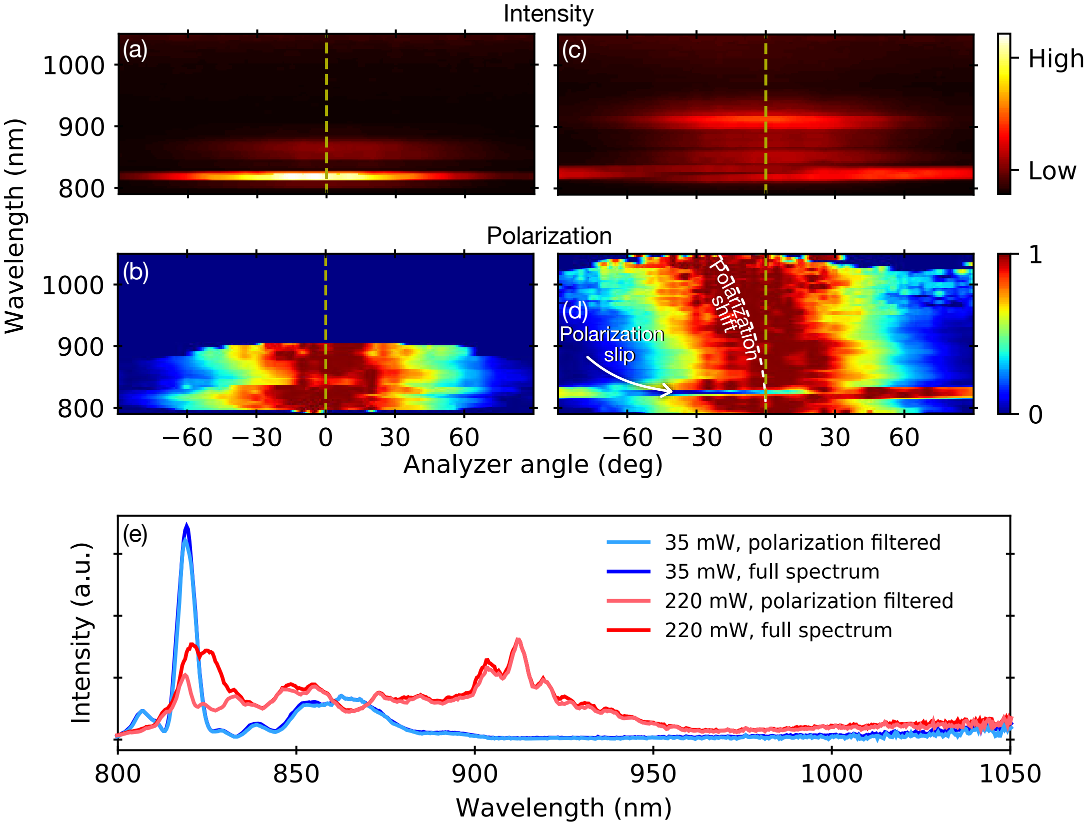

Figure 4.5: Polarization-dependent spectral intensity of the supercontinuum output from the FemtoWHITE 800 with low and moderate PCF pump powers. (a) The raw spectral-intensity polarization map of the supercontinuum with a low incident PCF pump power (35 mW). (b) Supercontinuum polarization intensity map obtained by normalizing (a) at each wavelength to highlight the polarization state. (c) The raw spectral-intensity polarization map of the supercontinuum with a moderate incident PCF pump power (220 mW). (d) Supercontinuum polarization intensity map obtained by normalizing (c) at each wavelength to highlight the polarization state. (e) The raw and polarized supercontinuum spectra from FemtoWHITE 800 at the two power conditions. The polarization angle is set to 0°, as denoted along the dashed lines in (a)–(d).

benzonitrile (3070 cm^{-1} resonance, Fig. 4.3(c,e)). In addition, the polarization of the supercontinuum is found to be relatively constant across the spectrum and once further polarized, there is minimal spectral attenuation except at the region of the polarization-slip (Fig. 4.5(e)). This region corresponds to the (largely inaccessible) CARS frequency range of 300 cm^{-1} – 450 cm^{-1}, and is thus mostly inconsequential.

Pumping the FemtoWHITE 800 along its main polarization axis, not only assures that the output supercontinuum is uniformly polarized, but also prevents the formation of closely-timed dual-solitons. However, with large enough PCF pump powers, higher wavelength portions of the supercontinuum become affected by the large birefringence of the fibre module. When doing an SF-CARS scan at the higher CH/OH frequencies, pumping the FemtoWHITE 800 with weaker powers can minimize the polarization shifting of the generated supercontinuum and allow more accurate SF-CARS spectroscopy, as demonstrated in the low-powered use of the FemtoWHITE 800 (Fig. 4.3(c)). Perhaps the future addition of high-quality PCF pump polarizer and improved polarization alignment may eliminate the polarization shifting in the FemtoWHITE 800.

4.6 CARS hyperspectral imaging

CARS hyperspectral imaging on an over-the-counter Tylenol tablet is used to demonstrate the qualitative performance of the two fibre modules. With the suggested operation of the fibres established through FWM spectroscopy, the FemtoWHITE CARS is operated with spectral surfing while the FemtoWHITE 800 is operated using a static 300 mW PCF pump (and polarized along the slow axis). Each 500 × 500 hyperspectral image stack of Tylenol, composed of 960 spectral points and collected with a 2 μs pixel dwell time, was acquired for a total of 16 minutes. As shown in Fig. 4.6 two main components of Tylenol were identified which correspond to acetaminophen [36] (most likely the monoclinic form, as will be discussed further in the next chapter) and a carbohydrate excipient (likely sucrose) [37]. Fingerprint-based CARS images were generated from the 790 cm^{-1} resonance of acetaminophen and the 850 cm^{-1} resonance of sucrose while a CH-based CARS image was generated using a 2920 cm^{-1} resonance found in acetaminophen and 3050 cm^{-1} for the excipient.[4]

4.6.1 CARS spectra

As shown in Figs. 4.6(g,h), the CARS spectra based on the FemtoWHITE CARS show sharp chemical resonances in the fingerprint while also providing qualitatively better spectral resolution than the FemtoWHITE 800. The differences in spectral resolution are most pronounced near 1500 cm^{-1} where three acetaminophen resonances peaks are easily resolved with the FemtoWHITE CARS while a single broad resonance is identified with the FemtoWHITE 800. It is unclear if the reduced spectral resolution we get with the FemtoWHITE 800 is an intrinsic problem with the module, or simply indicates inferior chirp-matching that can be subsequently optimized. In terms of CARS spectral strength, the FemtoWHITE CARS generates supercontinuum that can strongly stimulate sub-900 cm^{-1} resonances with signals comparable in strength to those from the 2000 cm^{-1} – 3000 cm^{-1} region. The FemtoWHITE 800 on the other hand, has CARS intensities that strongly stimulate frequencies around

---

[4] In Chapter 5, “Application of SF-CARS to pharmaceutical samples,” the excipient (sucrose) is reported at a frequency of 3085 cm^{-1} which was based on a retrieved Raman-like spectrum. Here, the 3050 cm^{-1} of the excipient is based on the raw CARS spectrum. Retrieving Raman-like spectra may cause peak shifts that depends on magnitude of the the non-resonant background.

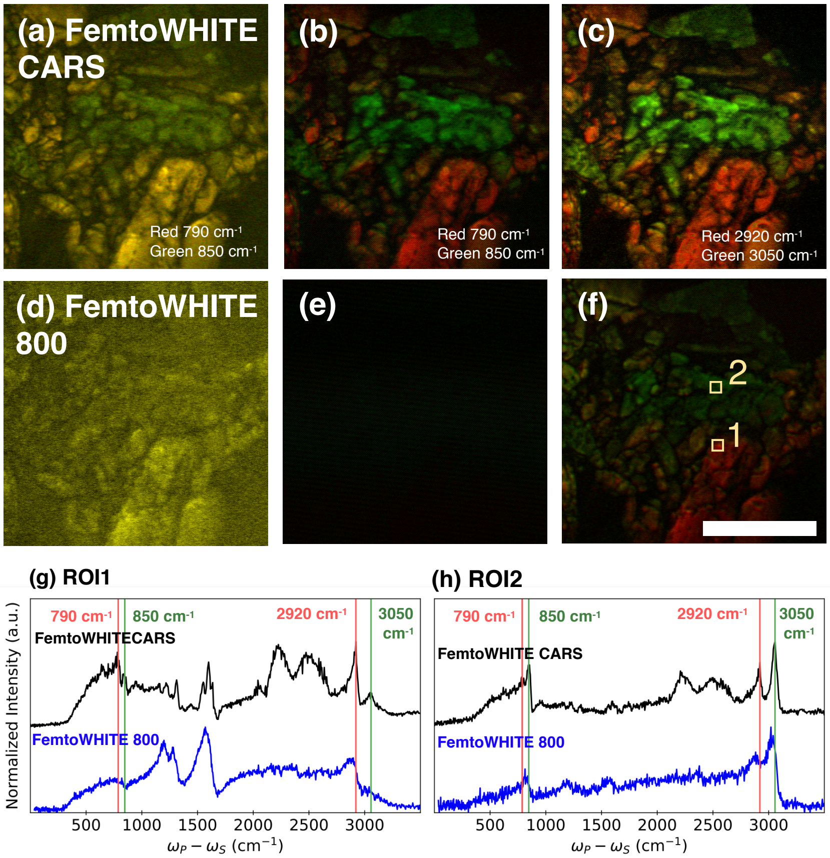

Figure 4.6: Hyperspectral CARS imaging of Tylenol. (a) Colour-merged CARS image obtained using the FemtoWHITE CARS showing the 790 cm^{-1} (red) and 850 cm^{-1} (green) resonances of Tylenol. (b) Contrast-enhanced image derived from (a). (c) Contrast-enhanced CARS image showing the 2920 cm^{-1} (red) and 3050 cm^{-1} (green). The lower panels (d-f) show the corresponding (d) Color-merged CARS image, and (e,f) contrast-enhanced CARS images obtained using the FemtoWHITE 800 showing the (d,e) 790 cm^{-1} and 850 cm^{-1}, and (f) 2920 cm^{-1} and 3050 cm^{-1} resonances from Tylenol. (g) Raw CARS spectra using each of the two PCFs at regions of interest 1 and (h) 2, as denoted by squares in (f). The leftmost pair of red and green vertical lines in (g) and (h) represent the frequencies 790 cm^{-1}, and 850 cm^{-1}; the rightmost pair represents 2920 cm^{-1} and 3050 cm^{-1}, all of which are used to obtain the CARS images (a-f). Images (a) and (d) show raw (unprocessed) CARS signal intensities, while images (b-c, e-f) are contrast-enhanced (see Appendix I). The color-merged images (a,d) were normalized in with respect to its individual color channel (divided by max value), while the contrast-enhanced images (b,c,e,f) are normalized with respect to image (c), and are thus directly comparable. The scale bar represents 25 μm.

3000 cm^{-1} and gradually decrease down to $\approx$ 350 cm^{-1}, although excluding the particularly strong resonances between 1200 cm^{-1}–1700 cm^{-1}. From the standpoint of CARS spectroscopy, the spectrally-surfed FemtoWHITE CARS outperforms the FemtoWHITE 800 in the sub-900 cm^{-1} region as shown by comparison of Figs. 4.6(g) and 4.6(h).

4.6.2 Composite CARS images

Although strong resonances in the CH/OH frequencies can be used to observe chemical contrast, obtaining contrast from weak resonances deep in the fingerprint show the most notable performance difference between the fibre modules, as shown in the color-merged Figs. 4.6(a,d) and the contrast-enhanced Figs. 4.6(b,e). With the FemtoWHITE CARS, we can construct contrasting chemical images based on the 790 cm^{-1} and 850 cm^{-1} resonance of acetaminophen and sucrose, respectively (Fig. 4.6(a,b)). With the FemtoWHITE 800, however, we were not able to create images that display enough contrast between chemical components as shown in Fig. 4.6(d,e).

This difference in contrast between the chemical images obtained between the fibre modules can be inferred from the CARS spectra of each compound (Fig. 4.6(g,h)) which were obtained by selecting two regions-of-interests (ROIs) in the sample as labeled in Fig. 4.6(f). With the FemtoWHITE CARS, the sharp resonance peaks of acetaminophen at 790 cm^{-1} and sucrose at 850 cm^{-1} are clearly distinguishable. Both 790 cm^{-1} and 850 cm^{-1} resonance peaks show differing intensity values such that even with the presence of a strong NRB, are distinct from each other (Fig. 4.6(a)). By exploiting the dispersive line shape of CARS peaks we can implement contrast-enhancement protocols (see Appendix I) to generate a chemical image with greater detail (Fig. 4.6(b)). With the FemtoWHITE 800, no sharp resonances can be found in the sub-900 cm^{-1} frequencies aside from the ≈ 850 cm^{-1} resonance of sucrose that has a relatively low signal-to-noise ratio. Thus, the main source of contrast comes from the NRB resulting in a monotonic CARS image (Fig. 4.6(d)). As expected, applying a contrast-enhancement procedure would not yield a useful chemical map (Fig. (4.6(e)). The low performance of the FemtoWHITE 800, in this case, may be attributed to the combined effect of sub-optimal spectral resolution which causes the NRB to overwhelm resonant signals [38], and the generation of weaker Stokes due to its relatively flat and broad supercontinuum. Increasing the sample concentration and the pump power may improve the spectral quality observed with the FemtoWHITE 800, but at the risk of inducing sample photodamage.

With regards to the CH-based CARS images (Figs. (4.6(c,f)), we obtained similar contrasts with either fibre module, however, with poorer spectral resolution and weaker signal intensity with the FemtoWHITE 800. Overall, pumping the FemtoWHITE 800 with modest powers (> 160 mw) works well for hyperspectral SF-CARS imaging in the CH/OH and silent regions, though somewhat less well in the fingerprint region compared with a spectrally-surfed FemtoWHITE CARS.

4.7 Summary and conclusion

We have compared two commercially-available PCF modules, the FemtoWHITE CARS and the FemtoWHITE 800, in view of SF-CARS. Ultimately, both PCF modules can be used in high-quality broadband SF-CARS hyperspectroscopy. The FemtoWHITE 800 is more convenient to use than the FemtoWHITE CARS as the supercontinuum it generates is known to be relatively stable and quickly broadens while able to span the fingerprint-to-OH frequencies and thus does not require the implementation of supercontinuum boosting techniques such as spectral-surfing. The polarization-maintaining property of the FemtoWHITE 800 allows it to generate a stable supercontinuum although it comes at a cost as it also facilitates the generation of closely-timed dual-solitons that may result in ambiguous SF-CARS spectra. The FemtoWHITE CARS, on the other hand, is already manufactured for easy use in CH/OH SF-CARS hyperspectroscopy. It, however, requires supercontinuum boosting techniques such as spectral surfing to enable enhanced SF-CARS hyperspectroscopy in the fingerprint frequencies. The FemtoWHITE CARS does not contain a polarization maintaining fibre; therefore, it does not suffer from the generation of dual-solitons as that of the FemtoWHITE 800. Because the FemtoWHITE CARS is not a polarization-maintaining fibre, the supercontinuum it generates suffers from significant intensity loss when polarized. Thus, a polarization-maintaining version of the FemtoWHITE CARS, paired with a high-quality PCF pump polarizer to minimize the possibility of generating supercontinuum duplicates and with a post-module polarizer to eliminate remaining duplicates, may yield stronger and more stable supercontinuum for broadband SF-CARS hyperspectroscopy.

References

1. Porquez, J. G., Cole, R. A. & Slepkov, A. D. Comparison of two photonic crystal fibers for supercontinuum-Stokes spectral-focusing-CARS hyperspectroscopy. *OSA Continuum* **1,** 1385 (2018).

2. Porquez, J. G., Cole, R. A., Tabarangao, J. T. & Slepkov, A. D. Spectrally-broad coherent anti-Stokes Raman scattering hyper-microscopy utilizing a Stokes supercontinuum pumped at 800 nm. *Biomedical Optics Express* **7,** 4335 (2016).

3. Porquez, J. G. & Slepkov, A. D. Application of spectral-focusing-CARS microscopy to pharmaceutical sample analysis. *AIP Advances* **8,** 095213 (2018).

4. Porquez, J. G., Cole, R. A., Tabarangao, J. T. & Slepkov, A. D. Brighter CARS hypermicroscopy via "spectral surfing" of a Stokes supercontinuum. *Optics Letters* **42,** 2255 (2017).

5. Liu, Y. *et al.* Suppressing Short-Term Polarization Noise and Related Spectral Decoherence in All-Normal Dispersion Fiber Supercontinuum Generation. *Journal of Lightwave Technology* **33,** 1814–1820 (2015).

6. Klarskov, P., Isomäki, A., Hansen, K. P. & Andersen, P. E. Supercontinuum generation for coherent anti-Stokes Raman scattering microscopy with photonic crystal fibers. *Optics Express* **19,** 26672 (2011).

7. Lee, Y. J., Liu, Y. & Cicerone, M. T. Characterization of three-color CARS in a two-pulse broadband CARS spectrum. *Optics Letters* **32,** 3370–3372 (2007).
8. Porquez, J. G., Korfanty, E. R. & Slepkov, A. D. Ultra-broadband coherent anti-Stokes Raman scattering microscopy with a dynamically power-tuned Stokes supercontinuum. *Proc. SPIE* **10069,** 1–10 (2017).
9. NKT Photonics. *FemtoWHITE 800* `https://www.nktphotonics.com/wp-content/uploads/sites/3/2015/03/femtoWHITE-800.pdf` (2018).
10. Hilligsøe, K. M. *et al.* Supercontinuum generation in a photonic crystal fiber with two zero dispersion wavelengths. *Optics Express* **12,** 1045 (2004).
11. NKT Photonics. *FemtoWHITE CARS* `http://www.nktphotonics.com/wp-content/uploads/sites/3/2015/03/femtoWHITE-CARS.pdf` (2017).
12. Hartshorn, C. M. *et al.* Multicomponent chemical imaging of pharmaceutical solid dosage forms with broadband CARS microscopy. *Analytical Chemistry* **85,** 8102–8111 (2013).
13. Kano, H. & Hamaguchi, H.-o. Ultrabroadband (>2500cm^{-1}) multiplex coherent anti-Stokes Raman scattering microspectroscopy using a supercontinuum generated from a photonic crystal fiber. *Applied Physics Letters* **86,** 121113 (2005).
14. Rehbinder, J., Pohling, C., Buckup, T. & Motzkus, M. Multiplex coherent anti-Stokes Raman microspectroscopy with tailored Stokes spectrum. *Optics letters* **35,** 3721–3 (2010).
15. Groß, P., Kleinschmidt, L., Beer, S., Cleff, C. & Fallnich, C. Single-laser light source for CARS microscopy based on soliton self-frequency shift in a microstructured fiber. *Applied Physics B: Lasers and Optics* **101,** 167–172 (2010).

16. Naji, M., Murugkar, S. & Anis, H. Determining optimum operating conditions of the polarization-maintaining fiber with two far-lying zero dispersion wavelengths for CARS microscopy. *Optics Express* **22,** 10800 (2014).

17. Edmund Optics. *50X Mitutoyo Plan Apo Infinity Corrected Long WD Objective* `https://www.edmundoptics.com/p/50x-mitutoyo-plan-apo-infinity-corrected-long-wd-objective/6626/` (2019).

18. Newport. *M-40x* `https://www.newport.com/p/M-40X` (2019).

19. Porquez, J. G. *CRASHyperspectralAnalysis* `https://github.com/JeremyPorquez/CRASHyperspectralAnalysis` (2018).

20. Schindelin, J. *et al. Fiji: An open-source platform for biological-image analysis* 2012. arXiv: `1081-8693`.

21. Camp Jr, C. H., Lee, Y. J. & Cicerone, M. T. Quantitative, comparable coherent anti-Stokes Raman scattering (CARS) spectroscopy: Correcting errors in phase retrieval. *Journal of Raman Spectroscopy* **47,** 408–415 (2016).

22. Wang, Y., Lin, C.-Y., Nikolaenko, A., Raghunathan, V. & Potma, E. O. Four-wave mixing microscopy of nanostructures. *Advances in Optics and Photonics* **3,** 1 (2011).

23. Cole, R. A. & Slepkov, A. D. Interplay of pulse bandwidth and spectral resolution in spectral-focusing CARS microscopy. *Journal of the Optical Society of America B* **35,** 842 (2018).

24. Mohseni, M., Polzer, C. & Hellerer, T. Resolution of spectral focusing in coherent Raman imaging. *Optics Express* **26,** 10230 (2018).

25. Kano, H. & Hamaguchi, H.-o. Dispersion-compensated supercontinuum generation for ultrabroadband multiplex coherent anti-Stokes Raman scattering spectroscopy. *Journal of Raman Spectroscopy* **37,** 411–415 (2006).

26. Kano, H. Molecular vibrational imaging of a human cell by multiplex coherent anti-Stokes Raman scattering microspectroscopy using a supercontinuum light source. *Journal of Raman Spectroscopy* **39,** 1649–1652 (2008).

27. Ryu, I. S., Camp Jr, C. H., Jin, Y., Cicerone, M. T. & Lee, Y. J. Beam scanning for rapid coherent Raman hyperspectral imaging. *Optics Letters* **40,** 5826 (2015).

28. Lee, J. H., Cho, E. H., Shin, S.-M. M., Oh, M.-k. K. & Ko, D.-K. K. Comparative study of breast normal and cancer cells using coherent anti-stokes raman scattering microspectroscopy imaging. *Applied Physics Express* **5,** 082401 (2012).

29. Ortigosa-Blanch, A. *et al.* Highly birefringent photonic crystal fibers. *Optics Letters* **25,** 1325 (2000).

30. Arteaga-Sierra, F. R. *et al.* Supercontinuum optimization for dual-soliton based light sources using genetic algorithms in a grid platform. *Optics express* **22,** 23686–93 (2014).

31. Chen, K., Wu, T., Wei, H. & Li, Y. Dual-soliton Stokes-based background-free coherent anti-Stokes Raman scattering spectroscopy and microscopy. *Optics Letters* **41,** 2628 (2016).

32. Wu, T. *et al.* Flexible dual-soliton manipulation for coherent anti-Stokes Raman scattering spectroscopy. *Optics Express* **26,** 22001 (2018).

33. Rocha-Mendoza, I., Langbein, W., Watson, P. & Borri, P. Differential coherent anti-Stokes Raman scattering microscopy with linearly chirped femtosecond laser pulses. *Optics letters* **34,** 2258–2260 (2009).

34. Pope, I., Langbein, W., Watson, P. & Borri, P. Simultaneous hyperspectral differential-CARS, TPF and SHG microscopy with a single 5 fs Ti:Sa laser. *Optics Express* **21,** 7096 (2013).

35. Li, B., Borri, P. & Langbein, W. Dual/differential coherent anti-Stokes Raman scattering module for multiphoton microscopes with a femtosecond Ti:sapphire oscillator. *Journal of Biomedical Optics* **18,** 066004 (2013).

36. Kauffman, J. F., Batykefer, L. M. & Tuschel, D. D. Raman detected differential scanning calorimetry of polymorphic transformations in acetaminophen. *Journal of Pharmaceutical and Biomedical Analysis* **48,** 1310–1315 (2008).

37. De Veij, M. *et al.* Reference database of Raman spectra of pharmaceutical excipients. *Journal of Raman Spectroscopy* **40,** 297–307 (2009).

38. Cui, M., Bachler, B. R. & Ogilvie, J. P. Comparing coherent and spontaneous Raman scattering under biological imaging conditions. *Optics letters* **34,** 773–775 (2009).

Chapter 5

Application of SF-CARS to pharmaceutical samples

5.1 Chapter preface

Chapters two and three describe my work towards the development and study of our PCF-based CARS microscope. I have shown that we can extend our microscope's spectral access while improving signal strength through non-standard and creative approaches in pumping our PCF. In chapter four, I have discussed the use of two different PCF modules for SF-CARS and show how to minimize possible complexities that may arise in the resulting CARS spectrum. The three previous chapters thus detail the experimental development of an advanced PCF-based CARS microscopy system. Much of the development of CARS microscopy is motivated by potential applications in biomedicine. Our lab, however, is interested in exploring non-biomedical applications, with a particular interest in materials science. This chapter describes exploratory applications of our microscope system through the imaging and spectroscopy of pharmaceutical drugs. In some ways, this work is a demonstration of the current advantages and limitations of our technique. One minor aspect of technique development included in this chapter involves the addition of detection of CARS signals in the backwards direction. This is an important (if somewhat rare) capability for CARS imaging and characterization of optically-thick samples, and one that we had not previously implemented.

This chapter is based on work we published in AIP Advances [1], a poster presentation at a conference held in Switzerland (Advanced Photonics 2018)[2], and a conference held in San Jose, California (CLEO 2018) [3]. The work does not strictly follow chronologically from the previous chapter, as the research presented in this chapter established pharmaceutical samples as interesting test samples for our microscope system. We subsequently used such samples when continuing to develop our experimental platform, which is why they are included in the previous chapter (see Figure 4.6).

5.2 Introduction

5.2.1 The potential of SF-CARS for pharmaceutical imaging

There is a nascent application of CARS microscopy to pharmaceutical drug analysis, an application that has been dominated by traditional analysis techniques based on spontaneous Raman scattering [4]. Raman spectroscopy offers a high degree of accuracy and sensitivity in pharmaceutical drug identification; however, acquisition times are considerably long and performing chemical mapping typically takes a few hours merely yielding images with low spatial resolution [5]. Furthermore, the technique suffers from strong unwanted fluorescence from drug samples and thus may require the use of less standard laser wavelengths [6]. Nontheless, Raman spectroscopy performs exceptionally well when only a few spectra are needed for analysis. An example of such an application is the spot analysis of high-purity bulk sample analysis for forensic applications [7, 8]. CARS microscopy, on the other hand, can acquire images at high speeds with sharp spatial resolutions. Thus, chemical compounds are seen well-separated in heterogeneous samples. Since CARS is a non-linear optical process, requiring three beams to interact intensely at a small spot, its strict focal-excitation confers advantages in 3D chemical imaging. Furthermore, since the anti-stokes signal is well-separated in colour from fluorescence, the latter is not parasitic like it is with spontaneous Raman techniques, but can even be used as a concurrent imaging modality. Therefore, CARS microscopy can be used as an efficient chemical imaging technique alternative to Raman for pharmaceutical drug analysis [5].

5.3 Experimental Upgrades

For this work, I updated our setup by changing the backwards-channel (i.e. “epi-”) detector from a multialkali PMT (Hamamatsu H10723-01) optimized for collecting light at 300 nm – 600 nm, to a GaAs cathode PMT (Hamamatsu H7422-50), efficient at 500 nm – 850 nm, resulting in the enhanced detection of anti-Stokes at fingerprint frequencies. Routing of epi-signals was improved by using a more appropriate dichroic beamsplitter (Semrock FF776, see Appendix B for more details) that is placed before the microscope objective which allows the transmission of anti-Stokes corresponding

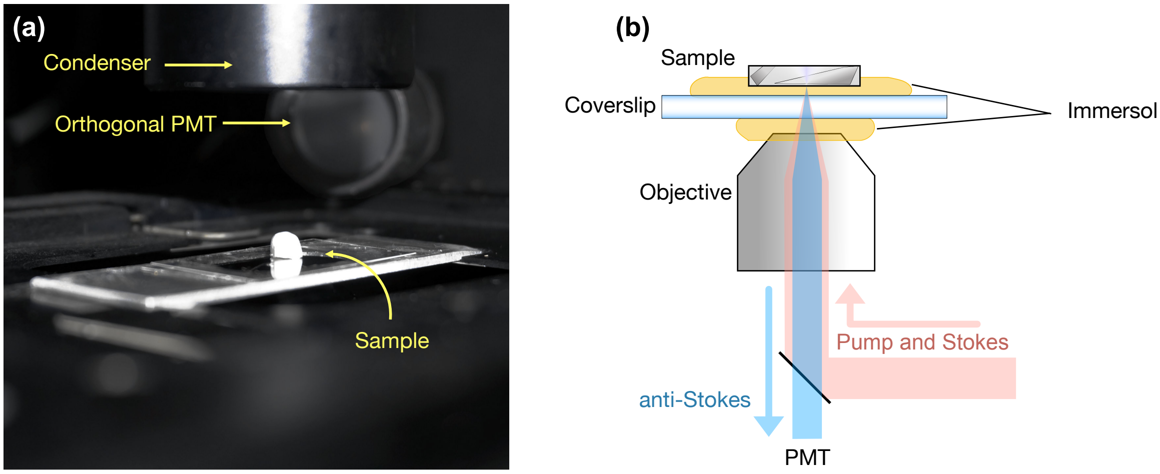

Figure 5.1: Additional microscopy information. (a) Setup showing the placement of the PMT used in detecting scattered laser light. (b) Setup showing the use of Immersol and the generation and detection of the epi-anti-Stokes.

to the deep fingerprint frequencies (50% Reflection at $\lambda_{AS} < 780$ nm, corresponds to frequencies > 320 cm^{-1}). A PMT was added (Hamamatsu H10721-01) to detect laser light scattered by the sample (Fig. 5.1(a)) and provides a transmission-like image. The detection of scattered light in this manner appears to be novel. It is relatively cheap and easy to implement and it offers great convenience to the experimentalist as it provides topographic information during an experiment when no other signals (such as SHG, CARS or TPEF) can be observed, thus allowing the experimentalist to easily find areas of interest that may be otherwise shrouded in darkness.

The spectral surfing algorithm has also been upgraded by adding cubic-interpolation fits, whereas before we used linear fits. The improved algorithm results in smoother HWP movements, improved experimental repeatability, and generally improves spectral surfing. Additionally, laser powers used for the experiments were lowered to less than 15 mW for the pump/probe and a maximum of 20 mW for the Stokes; both as measured at the sample plane. The pump power used here is significantly weaker compared to our previous works, e.g., >100 mW [9] and >50 mW [10].

5.3.1 Samples

Common over-the-counter tablets, 500 mg para-acetylaminophenol (an analgesic, commonly known as acetaminophen or paracetamol), 200 mg generic ibuprofen (a nonsteroidal anti-inflammatory drug), and 5 mg cetirizine HCl (an anti-histamine), were purchased from a local pharmacy. A tablet of acetaminophen and ibuprofen were pulverized, mixed, and re-compressed in a pellet press in order to prepare a flat surface that contains chemical components in the drug mixture suitable for quick CARS imaging. Acetaminophen and ibuprofen, in powder and compressed form, have similar textures and whitish colors; thus making each drug challenging to identify using standard microscopy techniques. The sample mixture is then mounted on a microscope coverslip, alternately with and without a drop of Immersol W 2010® (Zeiss). The Immersol acts as a non-dissolving index-matching medium (an advantage over the use of water) and sandwiches the coverslip (Fig. 5.1(b)) thereby improving the spatial resolution of our microscopy experiments. The Immersol did not show significant interaction or diffusion with the sample, and its signature 820 cm^{-1} vibrational resonance was not observed at the scanning depths within the sample. Additionally, a cetirizine sample was prepared by cutting a tablet in half. The cetirizine sample, in dry and unprocessed form without the use of Immersol, was then directly placed on a coverslip for 3D hyperspectral CARS microscopy as shown in Fig. 5.1(a).

5.4 Results and discussions

5.4.1 Hyperspectra of the drug mixture

A mixture of acetaminophen and ibuprofen along with their *excipients* (i.e., non-medical adjuncts) are indistinguishable when observed under normal (white) light illumination. However, CARS imaging based on characteristic peak signatures from these pharmaceutical drugs can help discriminate between each drug. Fig. 5.2 shows CARS images obtained from the hyperspectral data of the drug mixture, acquired in under 15 minutes with a scan speed of ≈ 5 cm^{-1}/s (5 μm/s delay stage speed over a span of 4350 μm). The spectral information, both raw CARS and Raman-retrieved, shows the intermixing of chemical compounds at the 1 to 2 μm scale; yet chemical maps can be generated by spectral unmixing, i.e., by subtracting CARS images at different frequencies.

A sucrose excipient is identified based on a strong 850 cm^{-1} peak [11] (shown in red in Fig. 5.2(a)). Acetaminophen and ibuprofen were individually identified based on their vibrational spectra around 1500 cm^{-1} – 1700 cm^{-1}. Acetaminophen contains at least three strong carbonyl vibrational modes in this region [12, 14], and thus manifesting as three peaks; ibuprofen contains only one strong C=C vibration at 1608 cm^{-1} [13, 15–17]. Acetaminophen provides strong contrast at 1620 cm^{-1} (green in Fig. 5.2(b)) while ibuprofen provides contrast based on its asymmetric CH stretching at $\approx$ 2870 cm^{-1} (cyan in Fig. 5.2(d)) [13].

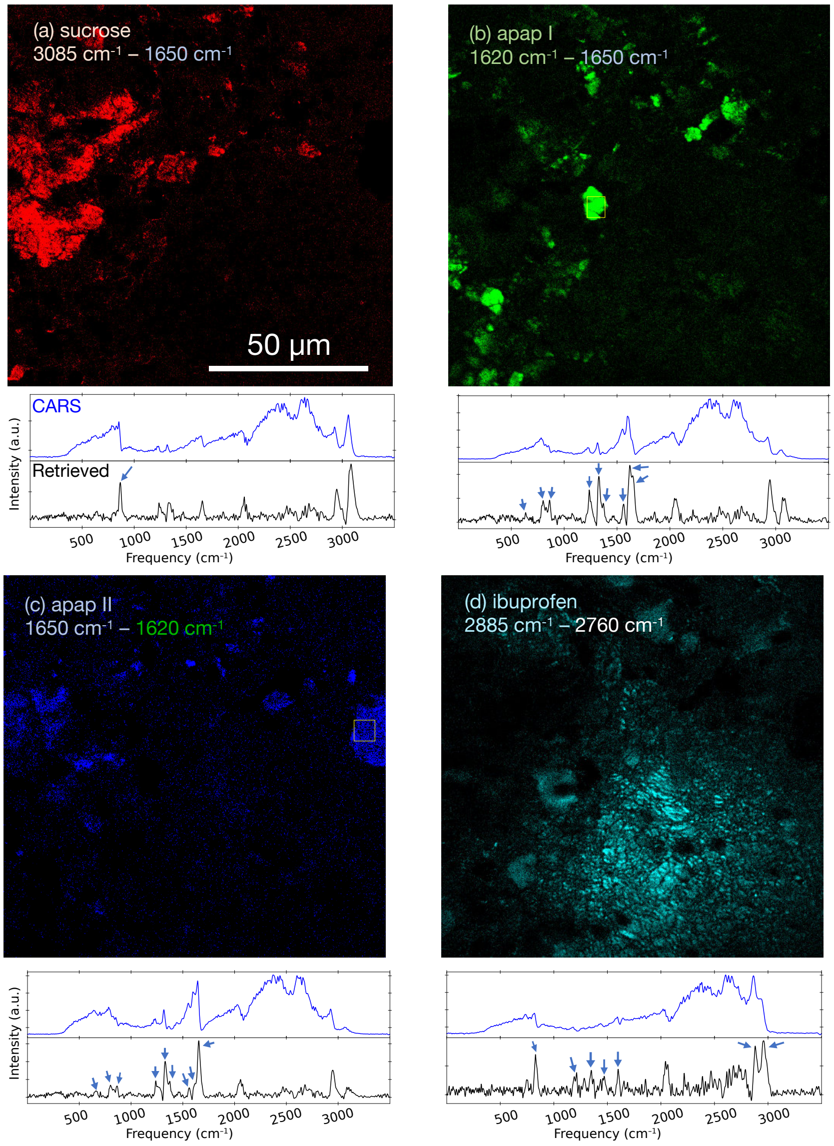

Figure 5.2: Hyperspectral image of the acetaminophen-ibuprofen reconstituted mixture. 120 μm × 120 μm CARS images of (a) sucrose (red), (b) acetaminophen (type I; green), (c) acetaminophen (type II; blue) and (d) ibuprofen (cyan); with corresponding CARS (blue line) and retrieved Raman-like spectra (black line) based on each respective regions of interest (yellow box). Arrows in the spectrum of (a-d) denote known resonances in these samples [11–13]. Color-contrast of the panels were improved by subtracting images at the frequencies labeled on top of the panels. The hyperspectral image consists of 500 × 500 pixels and 444 spectral data points scanned from 0 cm^{-1} up to 3500 cm^{-1} with a pixel dwell time of ≈ 5.7 μs, and a total stack acquisition time of 15 minutes.

5.4.2 Acetaminophen polymorphs

Interestingly, a compound with similar CARS response to acetaminophen (peak at 1620 cm^{-1}) was also found showing additionally strong contrast at 1650 cm^{-1} (blue in Fig. 5.2(c)). Spectral analysis of these two compounds suggests that they are known acetaminophen *polymorphs*—having the same chemical composition but different crystal structure. The former has closely spaced peaks in the 1500 cm^{-1} – 1700 cm^{-1} region (Fig. 5.3(a)) with a strong characteristic 1234 cm^{-1} peak (Fig. 5.3(b)) arising from aromatic C–O and C–N vibrations [12, 14]. This suggests that the species with the strong 1620 cm^{-1} contrast is more likely to be the monoclinic polymorph (type I) [12]. The latter has slightly more separated peaks in the 1500 cm^{-1} – 1700 cm^{-1} region with a stronger 1650 cm^{-1} peak (Fig. 5.3(a)), suggesting that it is likely to be the orthorhombic polymorph (type II) [12]. The apparent peaks in the silent region (2000 cm^{-1} – 2600 cm^{-1}) as shown in all the Raman-retrieved spectra in Fig. 5.2 do not match known vibrations in these samples and are attributable to the highly undulating supercontinuum at this region and artifacts associated with imperfectly-obtained non-resonant background scans used in the Raman retrieval process. With the identified chemical compounds, a composite CARS image is generated as shown in Fig. 5.4.

Despite the limitations in spectral resolution (≈ 25 cm^{-1}) and spectral noise of the microscope system, the results provide strong potential for dynamic chemical polymorph imaging with simple SF-CARS hyperspectroscopy. This is particularly useful in samples like acetaminophen where the orthorhombic polymorph is preferred over the monoclinic polymorph due to its high compression stability for tablet production [18].

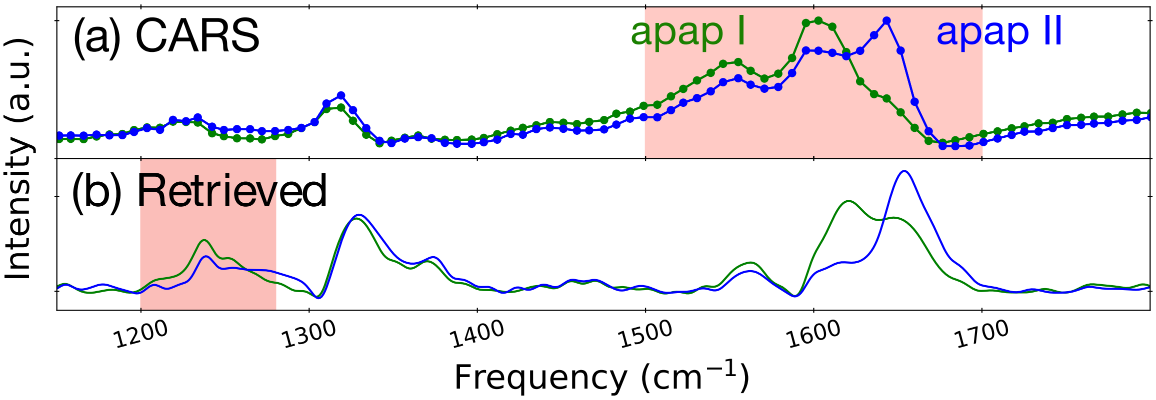

Figure 5.3: Raw and retrieved CARS spectra of acetaminophen. (a) Raw CARS spectra from Figs. 5.2(b,c), normalized to the 1620 cm^{-1} and 1650 cm^{-1} peaks, respectively, with the 1500 cm^{-1} to 1700 cm^{-1} region highlighted. (b) Retrieved Raman-like spectra from the CARS spectra of Figs. 5.2(b,c) highlighting the slight intensity difference at 1234 cm^{-1}.

5.4.3 3D CARS with cetirizine

Cetirizine is an antihistamine that is typically taken orally in small doses. In tablet form, most of the mass of cetirizine functions as bulking material. For example, a 500 mg tablet would only contain 5 mg of the active ingredient while the rest is excipient. In contrast to the heterogeneous and abundant distribution of acetaminophen and ibuprofen in tablets, observing a pulverized or powdered form of a cetirizine tablet would yield little to no CARS signals of the active ingredient because cetirizine can only be found as a thin coating on the tablets surface as shown in the cross-section CARS image in Fig. 5.5(a). The cetirizine coating measures 5.3 ± 0.9 μm thick. The inner bulk of the tablet shows a strong resonance at 2920 cm^{-1} attributed to the C-H stretch vibration from the collective mixture of carbohydrate excipients. The excipients did not show any remarkable peaks at frequencies below 2000 cm^{-1}

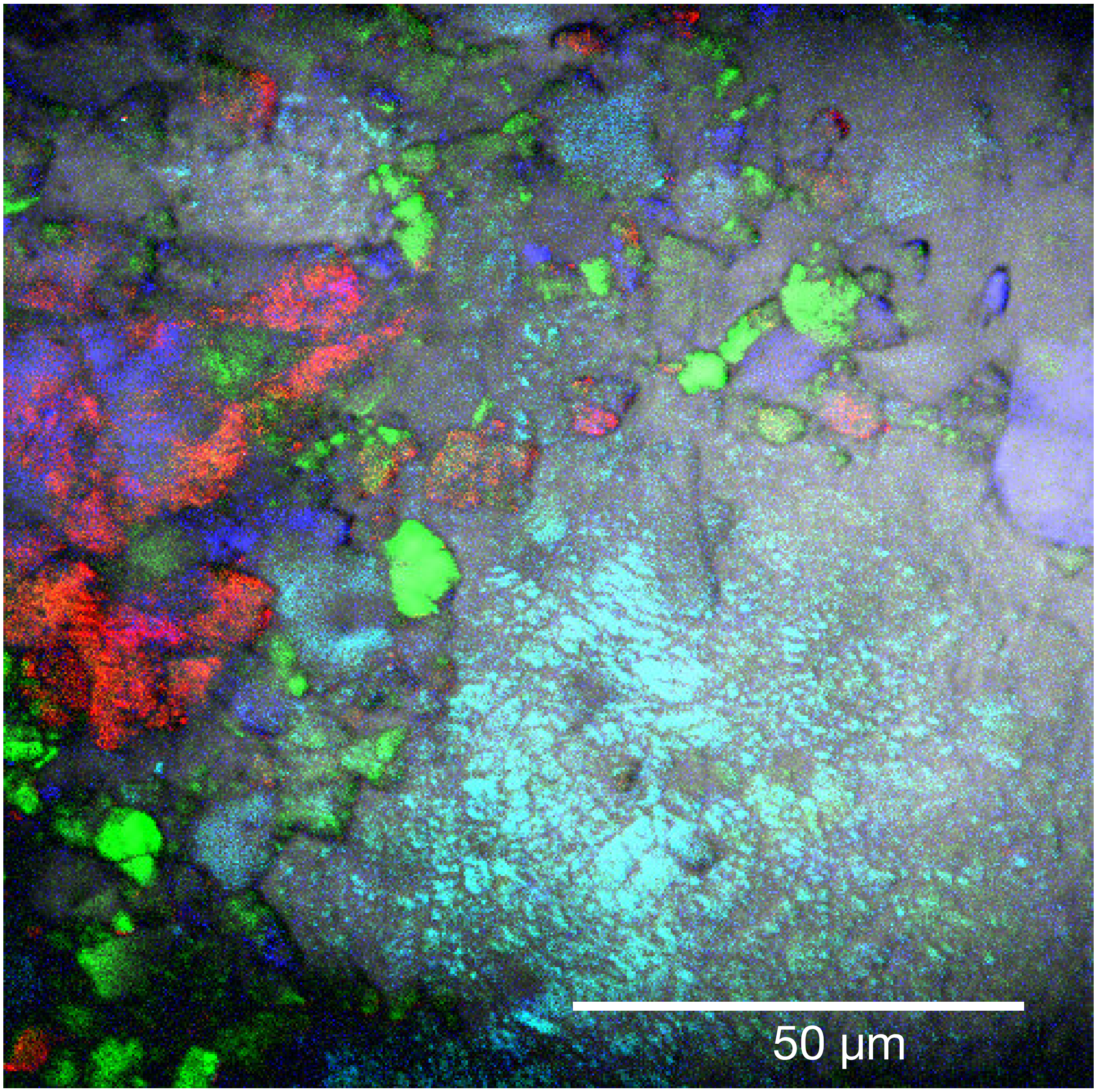

Figure 5.4: Composite image from 120 μm x 120 μm CARS images of sucrose (red), acetaminophen type I (green), acetaminophen type II (blue), ibuprofen (cyan), and overlaid with the scattered laser light channel (gray).

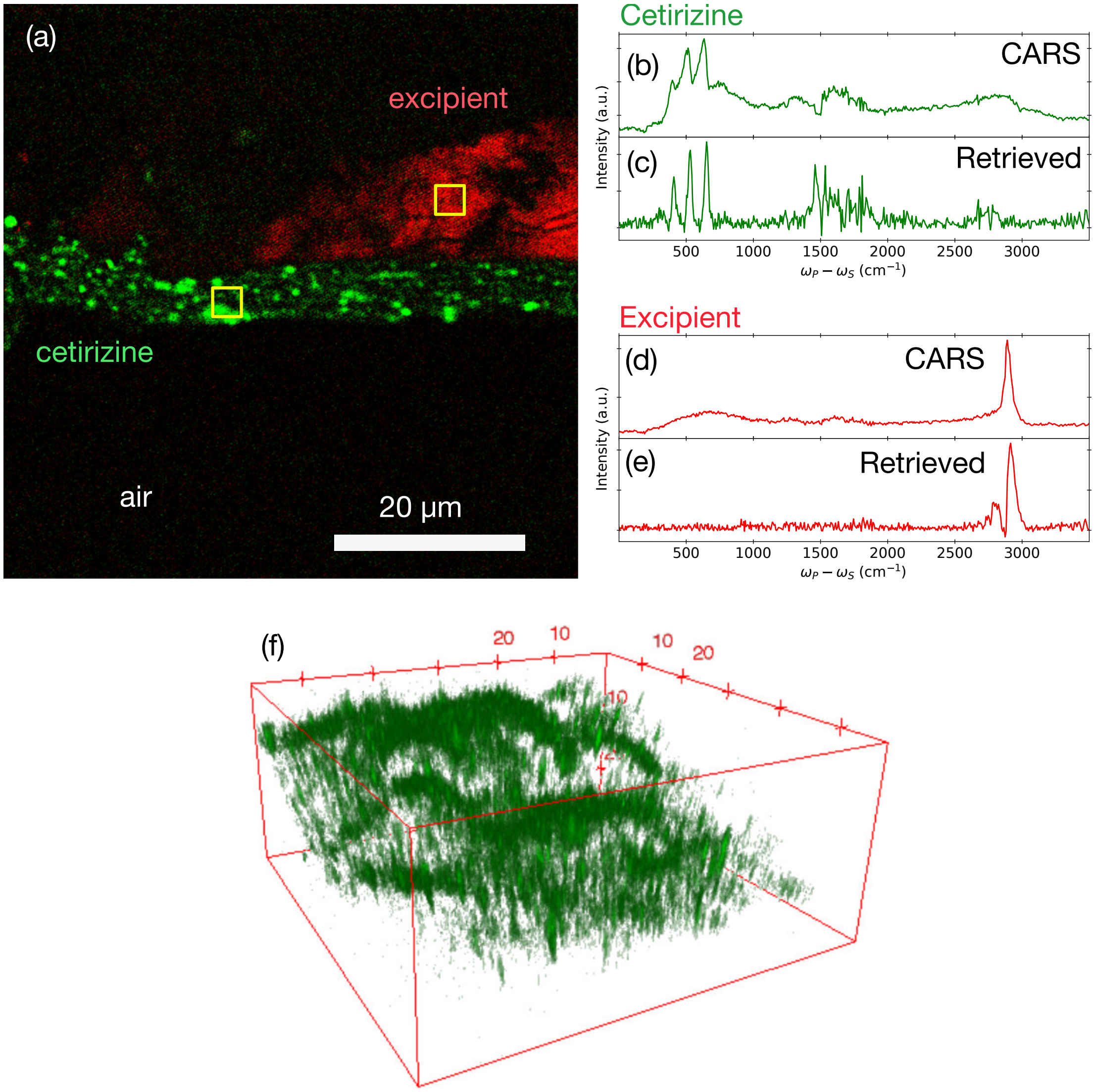

Figure 5.5: 3D CARS imaging of a cetirizine tablet. (a) A cross-section CARS image in the cut plane. Cetirizine (650 cm^{-1}, green contrast) is measured to be 5.3 ± 0.9 μm thick encapsulating the excipient (2915 cm^{-1}, red contrast). The hyperspectral image consists of 500 × 500 pixels and 525 spectral points, scanned with a 2.9 μs pixel dwell time, and collected in ≈ 9 minutes. (b,d) Raw CARS and (c,e) retrieved Raman-like spectrum of cetirizine and the excipient in regions of interest marked in (a). (f) 3D image (60 μm × 60 μm × 25 μm) of cetirizine (650 cm^{-1}) with 109 z-stacks (230 nm increments) and acquired in ≈ 4 minutes. The thickness of cetirizine in this region is measured to be 3.8 ± 0.6 μm. The pump power used for imaging was 8 mW. Multimedia view: https://doi.org/10.1063/1.5027273.1.

most likely due to low chemical concentrations and the weak pump powers ($<$8 mW) required for this application in order to avoid sample photo-degradation.

3-D SF-CARS microscopy of a whole, unprocessed caplet form of cetirizine is shown in Fig. 5.5(f). The experiment was designed to probe a volume of 60 μm × 60 μm × 25 μm at the 650 cm^{-1} resonance of cetirizine and at the 2920 cm^{-1} resonance of the excipient. Attempts were made to image through the cetirizine layer to the inner tablet bulk, but in all efforts, only a thin layer of cetirizine was measurable, and a negligible signal from the inner excipient bulk was detected. Excessive scattering and radiation trapping are presumed as the primary causes, and this obstacle was not overcome even with the application of index-matching oil. With further analysis, the cetirizine layer based on the 3-D CARS scan was measured to be 3.8 ± 0.6 μm thick, which is more than a micron thinner than that obtained with a cross-sectional cut-tablet scan of 5.3 ± 0.9 μm. The current setup can probe only 3.8 μm deep into such dense samples, and the sub-surface CARS signal is significantly weakened due to a combination of factors such as scattering and laser penetration depth, epi-detection geometry, use of low laser powers, and possible absorption of anti-Stokes signal in the surface layer. The use of longer wavelengths to increase penetration depth and further optimizations of the microscopy setup (e.g., use of longer working distance, high N.A. objectives, beam optimizations) can possibly enhance the 3D imaging capabilities for highly scattering powder samples such as pharmaceuticals.

5.5 Summary and conclusion

SF-CARS microscopy using a spectrally-surfed PCF Stokes supercontinuum has been applied to chemical mapping and 3-D imaging of chemically unprocessed pharmaceutical drug tablets using laser powers that are relevant for pharmaceutical analysis. The results show that SF-CARS can provide spectral information similar to that of multiplex-CARS and may provide imaging speeds similar to those of single-frequency CARS and stimulated Raman scattering [18]. Active pharmaceutical ingredients can be easily identified due to their inherent high concentration present in the drug preparations—a condition that is favorable to CARS microscopy. Chemical polymorphs are distinguishable in acetaminophen samples, enabled by broad hyper-spectral acquisition and adequate spectral resolution, and pharmaceutical excipients can be easily identified based on their concentration and dominant CH vibrational response.

Continued development of this technique should focus on improving the spectral quality to enable straight-forward comparison with Raman spectra and to focus on deeper imaging in tablets and large materials, perhaps by moving to longer pump wavelengths—as is becoming more common in other CARS microscopes [19, 20]. Furthermore, rapid chemical imaging in three-dimensions should allow for improved evaluation of chemical-constituent particle sizes, thereby enabling potential forensic applications such as in tracking the manufacturing origin of a particular drug (pharmaceutical or illicit). Such abilities are likely to find applications in counterfeit and black-market drug identification.

References

1. Porquez, J. G. & Slepkov, A. D. Application of spectral-focusing-CARS microscopy to pharmaceutical sample analysis. *AIP Advances* **8,** 095213 (2018).

2. Porquez, J. G. & Slepkov, A. D. *Spectral-surfing CARS hypermicroscopy of pharmaceutical samples with commercial supercontinuum generating photonic crystal fibres* in *Advanced Photonics 2018 (BGPP, IPR, NP, NOMA, Sensors, Networks, SPPCom, SOF)* (Optical Society of America, 2018), JTu5A.67. http://www.osapublishing.org/abstract.cfm?URI=BGPPM-2018-JTu5A.67.

3. Porquez, J. G. & Slepkov, A. D. *Broadband spectral focusing CARS of pharmaceutical drugs* in *Conference on Lasers and Electro-Optics* (OSA, Washington, D.C., 2018), AF2M.1. https://www.osapublishing.org/abstract.cfm?URI=CLEO%7B%5C_%7DAT-2018-AF2M.1.

4. Butler, H. J. *et al.* Using Raman spectroscopy to characterize biological materials. *Nature Protocols* **11,** 664–687 (2016).

5. Hartshorn, C. M. *et al.* Multicomponent chemical imaging of pharmaceutical solid dosage forms with broadband CARS microscopy. *Analytical Chemistry* **85,** 8102–8111 (2013).

6. Asher, S. A. & Johnson, C. R. Raman spectroscopy of a coal liquid shows that fluorescence interference is minimized with ultraviolet excitation. *Science,* 311–313 (1984).

7. Izake, E. L. Forensic and homeland security applications of modern portable Raman spectroscopy. *Forensic Science International* **202,** 1–8 (2010).

8. Katainen, E. *et al.* Quantification of the Amphetamine Content in Seized Street Samples by Raman Spectroscopy. **52,** 88–92 (2007).

9. Porquez, J. G., Cole, R. A., Tabarangao, J. T. & Slepkov, A. D. *Spectrally broad spectral-focussing-based coherent anti-Stokes Raman hyper-microscopy with a single 800-nm laser source* Montreal, Quebec, 2016.

10. Porquez, J. G., Cole, R. A., Tabarangao, J. T. & Slepkov, A. D. Brighter CARS hypermicroscopy via "spectral surfing" of a Stokes supercontinuum. *Optics Letters* **42,** 2255 (2017).

11. De Veij, M. *et al.* Reference database of Raman spectra of pharmaceutical excipients. *Journal of Raman Spectroscopy* **40,** 297–307 (2009).

12. Kauffman, J. F., Batykefer, L. M. & Tuschel, D. D. Raman detected differential scanning calorimetry of polymorphic transformations in acetaminophen. *Journal of Pharmaceutical and Biomedical Analysis* **48,** 1310–1315 (2008).

13. Jubert, A., Legarto, M. L., Massa, N. E., Tévez, L. L. & Okulik, N. B. Vibrational and theoretical studies of non-steroidal anti-inflammatory drugs Ibuprofen [2-(4-isobutylphenyl)propionic acid]; Naproxen [6-methoxy-α-methyl-2-naphthalene acetic acid] and Tolmetin acids [1-methyl-5-(4-methylbenzoyl)-1H-pyrrole-2-acetic acid]. *Journal of Molecular Structure* **783,** 34–51 (2006).

14. Kachrimanis, K., Braun, D. E. & Griesser, U. J. Quantitative analysis of paracetamol polymorphs in powder mixtures by FT-Raman spectroscopy and PLS regression. *Journal of Pharmaceutical and Biomedical Analysis* **43,** 407–412 (2007).

15. Rossi, B. *et al.* Vibrational properties of ibuprofen-cyclodextrin inclusion complexes investigated by Raman scattering and numerical simulation. *Journal of Raman Spectroscopy* **40,** 453–458 (2009).

16. De Beer, T. R. M., Baeyens, W. R. G., Ouyang, J., Vervaet, C. & Remon, J. P. Raman spectroscopy as a process analytical technology tool for the understanding and the quantitative in-line monitoring of the homogenization process of a pharmaceutical suspension. *The Analyst* **131,** 1137 (2006).

17. Hédoux, A., Guinet, Y., Derollez, P., Dudognon, E. & Correia, N. T. Raman spectroscopy of racemic ibuprofen: Evidence of molecular disorder in phase II. *International Journal of Pharmaceutics* **421,** 45–52 (2011).

18. Di Martino, P., Guyot-Hermann, A. M., Conflant, P., Drache, M. & Guyot, J. C. A new pure paracetamol for direct compression: The orthorhombic form. *International Journal of Pharmaceutics* **128,** 1–8 (1996).

19. Tu, H. *et al.* Stain-free histopathology by programmable supercontinuum pulses. *Nature Photonics* **10,** 534–540 (2016).

20. Chen, K., Wu, T., Wei, H. & Li, Y. Dual-soliton Stokes-based background-free coherent anti-Stokes Raman scattering spectroscopy and microscopy. *Optics Letters* **41,** 2628 (2016).

Chapter 6

Thesis summary

I have developed a world-class multimodal CARS microscopy platform based on spectral focusing of a PCF-derived supercontinuum Stokes source. Before this work, similar systems were mostly only able to probe the silent-to-CH/OH vibrational resonances, and only had limited access to the fingerprint region by using a wholly different pump wavelength. Through the collective efforts in Dr. Slepkov's lab, we can now easily probe the vast chemically relevant vibrational spectrum from 350 cm^{-1} up to 3500 cm^{-1}, without needing to tune the pump wavelength away from 800 nm, making our microscope one of the most simple to use, highly capable CARS hyper-spectroscopy systems in the world. Importantly, the cost of building our microscope system is relatively cheaper than other CARS microscopes since it only uses a single pulsed laser source, making the system much more accessible to a wide variety of groups that need such characterization equipment.

The PCF module I mainly used in this thesis, the FemtoWHITE CARS, was primarily designed for implementing CARS microscopy in the CH/OH frequencies. By tailoring the fibre's pump pulse through dispersion, which results in weaker pulse peak powers, we are able to generate supercontinuum useful for CARS in the fingerprint frequencies. Furthermore, by applying a novel dynamic supercontinuum generation scheme, we were able to generate brighter supercontinuum for spectral focusing CARS across a wider range of frequencies. These modifications have allowed us to use the FemtoWHITE CARS beyond its commercial specifications and have used it for CARS microscopy at fingerprint frequencies as low as 350 cm^{-1}. With improved access to a wide range of frequencies, we have demonstrated CARS hyperspectroscopy of pharmaceutical drugs, liquid chemicals, and biological samples.

The use of such supercontinuum generation enhancing schemes may not only be limited to the FemtoWHITE CARS. The use of a polarization-maintaining fibre version of the FemtoWHITE CARS, paired with spectral surfing or even the use of a new fibre altogether, with or without the need of supercontinuum boosting techniques, may perhaps generate stronger and more stable supercontinuum for broadband, fingerprint-to-CH/OH CARS hyperspectroscopy. This thesis establishes a baseline of comparison for future technical advances in such source development, while suggesting certain opportunities for improvement of spectral characteristics both of new broadband sources and of CARS hyperspectroscopy data.

Appendix A

Dispersion

This section contains material that may be useful in introducing the concept of dispersion of light.

From the introduction, it was shown that ultrashort pulses can be modelled using a Gaussian field which can be written as [1]

$$E(t) \propto E_0 e^{-\alpha t^2} e^{i(\omega t + \beta t^2)} \tag{A.1}$$

where E_0 is the amplitude of the electric field, α is a parameter that represents the temporal width of the field,[1] ω is the frequency, and β is known as the linear chirp parameter (or the frequency-time slope of the pulses as shown in Fig. 1.8(f) and can be written in units of cm^{-1}/fs). Equation A.1 is a condensed form of the more general equation of the field

$$E(t) \propto E_0 e^{i(kz - \omega' t)} \tag{A.2}$$

---

[1] In terms of FWHM, $\alpha = \frac{4ln2}{\text{FWHM}^2}$.

where k is the wavenumber and z is the displacement. Here, ω contains higher order frequency components such as βt.

The rate of change of the frequency with respect to wavenumber, i.e., $\frac{d\omega}{dk}$, is known as the group velocity, v_G. For monochromatic light propagating through a vacuum, the group velocity is simply equal to the speed of light, i.e., $v_G = c$. In a dispersive medium with a refractive index, n, the group velocity slows down by a factor of n, i.e., $v_G = c/n$. For ultrashort light pulses[2] propagating through a vacuum, each frequency component of light travels at a speed of $v_G = c$. However, when propagating through a dispersive medium, the index of refraction becomes a function of the frequency, i.e., $n = n(\omega)$, and each frequency component propagates with speed $v(\omega) = c/n(\omega)$, and thus, colours of light separate in space.

The derivative of the group velocity, i.e., $\frac{d^2\omega}{dk^2}$, is called the group velocity dispersion (GVD). The GVD essentially describes the rate the group velocity separates with respect to the refractive index.[3]

A.1 Normal and Anomalous Dispersion

Figure A.1 shows the a materials refractive index as a function of frequency. Normal dispersion regions are regions where n increases with frequency while anomalous dispersive regions are regions where n decreases with frequency.

---

[2] Ultrashort light pulses inherent possess a range of colour components or frequencies.

[3] Since $k = nk_0$, where k_0 is the wavenumber in vacuum.

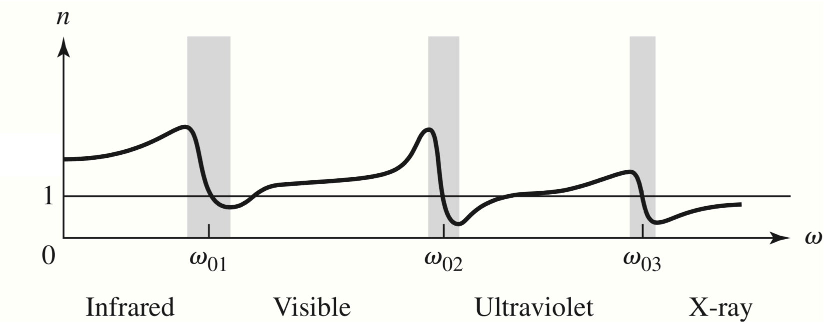

Figure A.1: Normal vs anomalous dispersion. Figure and caption modified and adapted from ref [2].

Appendix B

Optical filters

This section contains essential optical filters used in the microscope system. The filters described here are ones that we use to give our CARS microscope access to fingerprint frequencies. Most filters we use are 1” diameter filters and 25 mm × 35 mm filters (fitted inside the microscope). Most of the filters were obtained through Semrock, Thorlabs, and Chroma. Both Semrock and Chroma supplies high-quality edge-pass (short-pass or long-pass) filters while Thorlabs supply good quality band-pass filters.

Semrock FF01-937/LP : Beam combiner

The Semrock FF01-937/LP was used in an early version of the microscope system as a beam combiner. When the filter is oriented at 45°, it effectively becomes an 840 nm long pass filter.

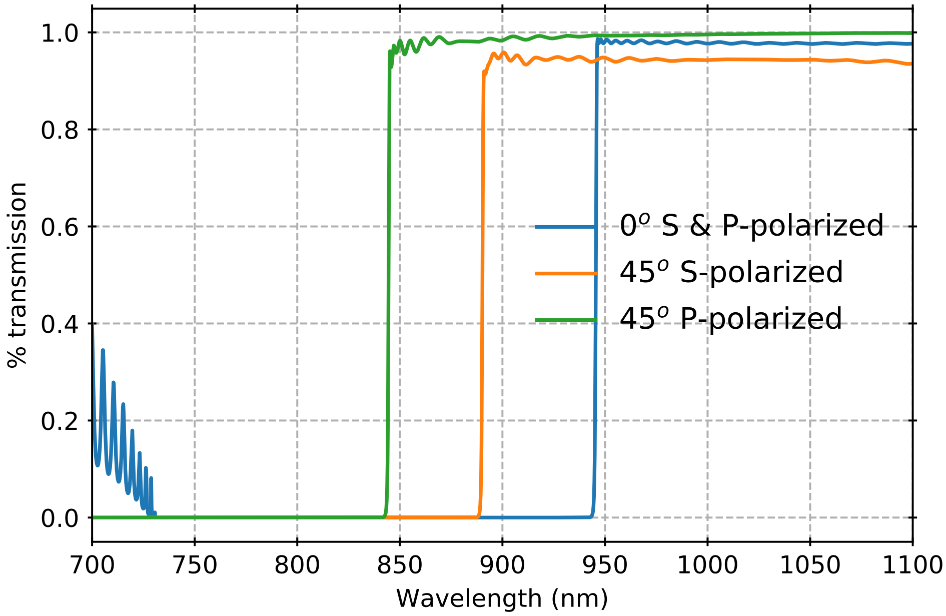

Figure B.1: Transmission property of FF-01-937/LP. The data can be generated using the MyLightTool after selecting the filter part number : FF01-937/LP-25 from the website, https://www.semrock.com/.

Chroma T810lpxr : Beam combiner

The Chroma T810lpxr is used to replace the Semrock FF01-937/LP beam combiner for the latest version of the microscope system. It is effectively an 818 nm long pass filter therefore allowing > 818 nm (>275 cm^{-1}) of the supercontinuum to be transmitted and be used as Stokes.

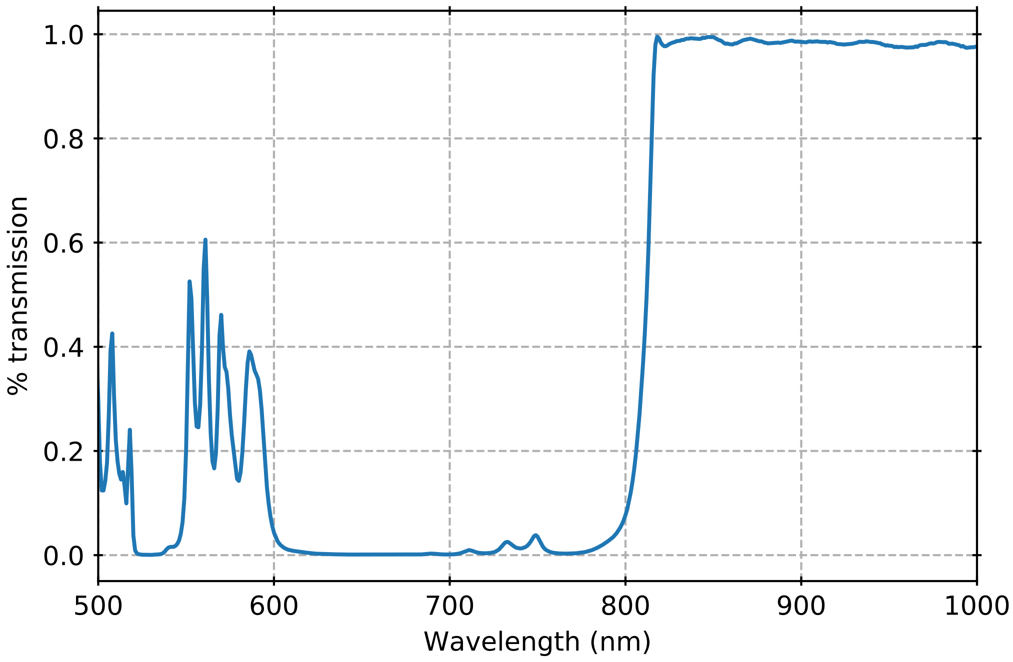

Figure B.2: Transmission property of the Chroma T810lpxr oriented at 45°. The data can be generated from https://www.chroma.com/products/parts/t810lpxr.

Semrock SP01-785RU : Foward-detection filter

The Semrock SP01-785RU filter is used as a transmission filter positioned in the forward-direction (placed after the microscope condenser, before the PMT routing optical fibers) which allows < 778 nm (> 350 cm^{-1}) of forward-generated anti-Stokes to be transmitted and detected by a PMT. However, additional filters, such as the Thorlabs FESH0950, are needed alongside the SP01-785RU to eliminate transmission fringes coming from the supercontinuum Stokes at wavelengths > 950 nm.

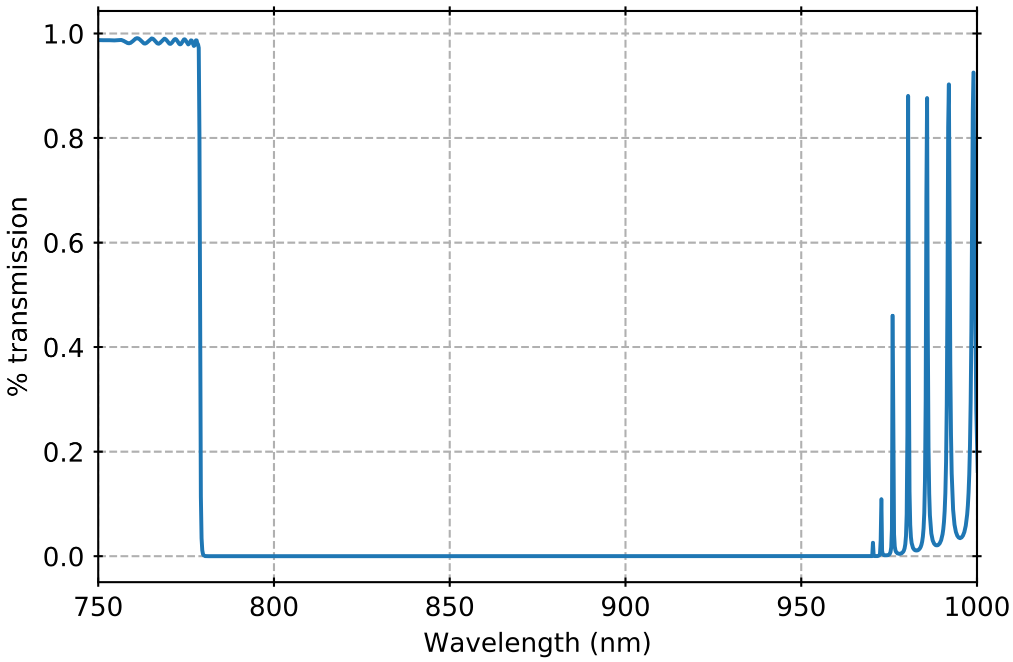

Figure B.3: Transmission property of the Semrock SP01-785RU. The data can be generated using the MyLightTool after selecting the filter part number : SP01-785RU from the website, https://www.semrock.com/.

Semrock FF776 : Epi-detection filter

The Semrock FF776 filter is used as a dichroic filter positioned in the epi-direction (placed before the objective) which allows < 790 nm (> 160 cm^{-1}) of epi-generated anti-Stokes to be reflected and detected by a PMT.

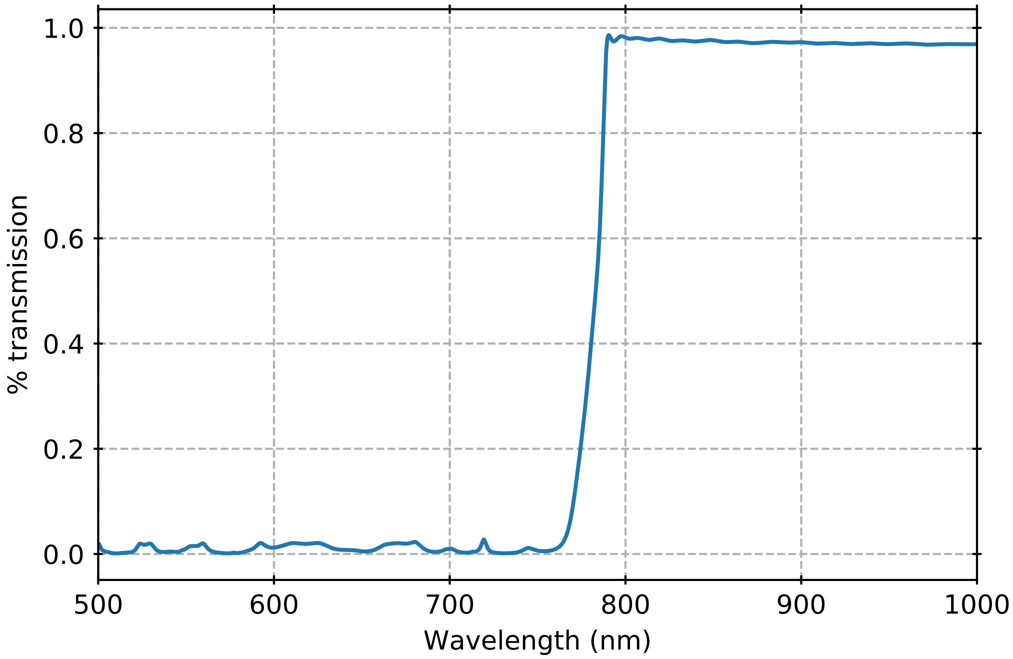

Figure B.4: Transmission property of the Semrock FF776 oriented at 45°. The data can be generated using the MyLightTool after selecting the filter part number : FF776-Di01-25x36 from the website, https://www.semrock.com/.

Thorlabs FESH0950 : Forward-detection cleanup filter

The Thorlabs FESH0950 filter is used as a filter to remove unwanted supercontinuum leakage in the forward direction. The filter allows transmission of wavelengths < 950 nm.

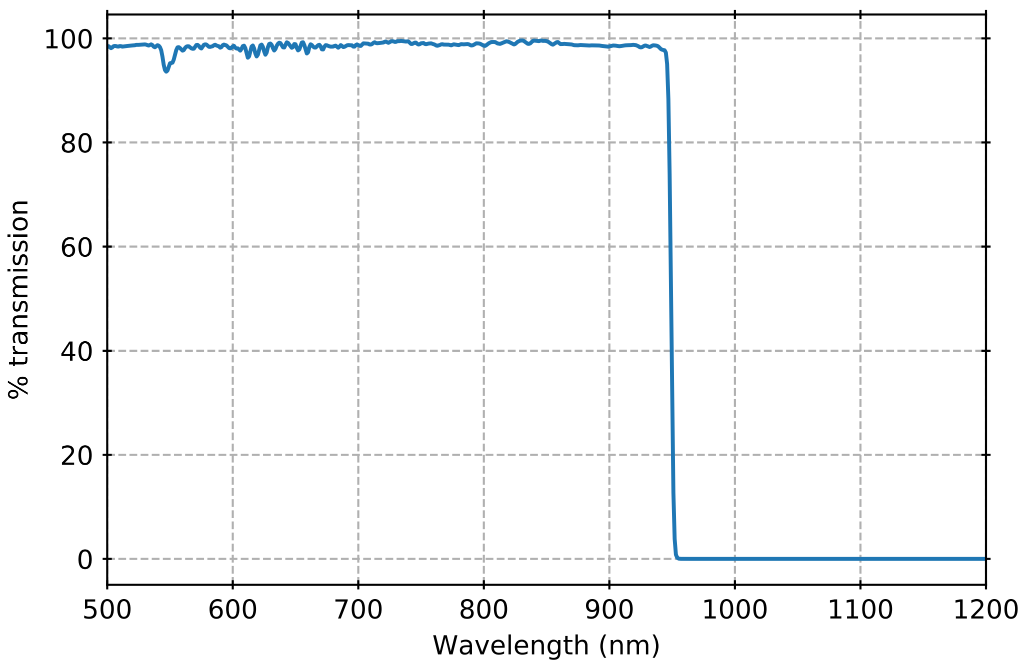

Figure B.5: Transmission property of the Thorlabs FESH0950. The data can be accessed by selecting the transmission data from the Thorlabs website.

Appendix C

Pump/Stokes polarization and CARS intensity

The anti-Stokes intensity can be written as $I_{AS} \propto |\chi_{1111}|^2 I_P^2 I_S (cos^2\phi + \frac{9}{16} sin^2\phi)$ where ϕ is the angle between the pump and Stokes beams and ρ is the depolarization ratio [3]. Use of co-polarized beams ($\phi = 0$) will generate an anti-Stokes, $I_{AS} \propto |\chi_{1111}|^2 I_P^2 I_S$, while use of orthogonal pump and Stokes beams will generate (a weaker) anti-Stokes, $I_{AS} \propto \rho^2 |\chi_{1111}|^2 I_P^2 I_S$ since $\rho < 1$.

Appendix D

Other setup details

D.1 PMT and shutter control

Four PMTs (Hamamatsu H10720 / H10723) are connected and controlled by a USB multichannel device (MCCDAQ USB-3101). The multichannel device can supply a voltage range from -10 V up to +10 V, however is limited to 1.0 V to prevent overloading the PMT. Supplying the PMT with 0.7 V gives optimal SNR; above 0.7 V, the noise is amplified leading to signal degradation. Additionally, the multichannel device is also used to control the pump and Stokes shutters by supplying 0 V (False) or +5 V (True). See Figs. D.1 and D.2 for more details.

D.2 Galvos and PMT readout

The galvos are responsible for deflecting both the pump and Stokes beams along two axes. They are controlled by a high-speed multifunction input/ouput (IO) device (National Instruments, PCI 6110), which sends a software-generated raster scan

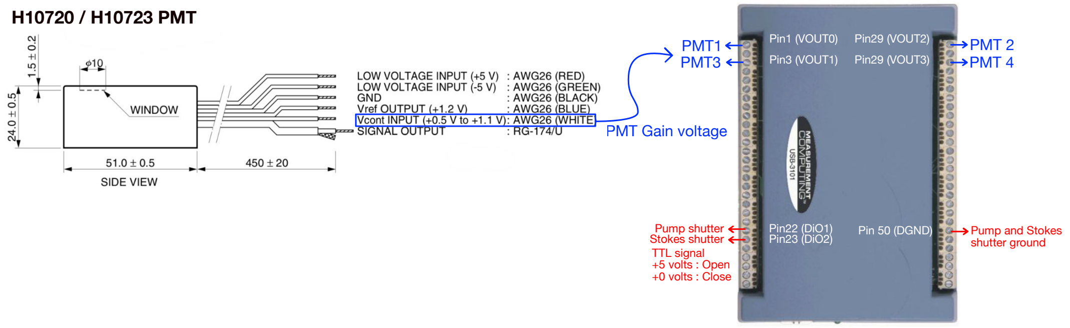

Figure D.1: Connection of the PMTs and shutters to USB multichannel device (MCC-DAQ USB-3101). Figures adapted and modified from Hamamatsu and Measurement Computing.

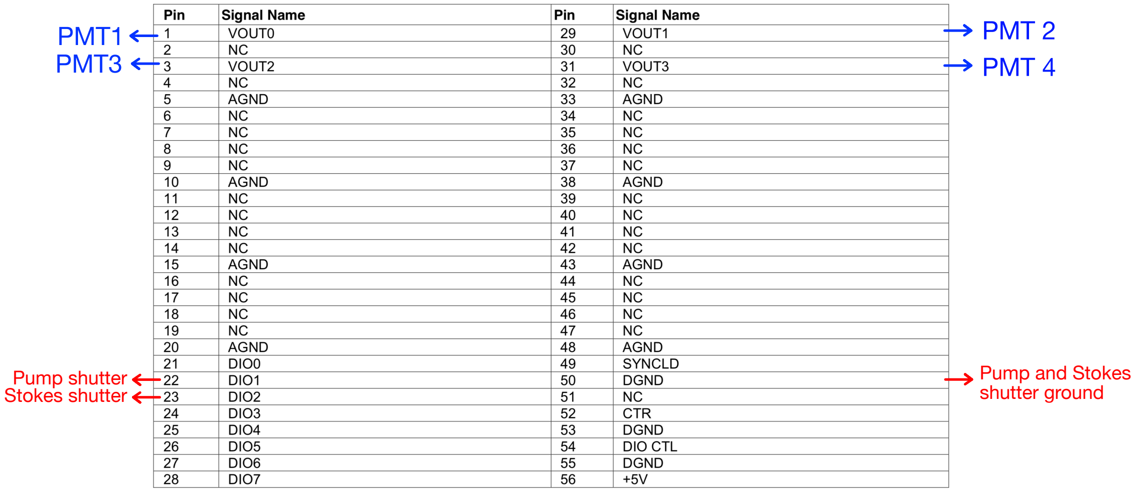

Pin	Signal Name	Pin	Signal Name
1	VOUT0	29	VOUT1
2	NC	30	NC
3	VOUT2	31	VOUT3
4	NC	32	NC
5	AGND	33	AGND
6	NC	34	NC
7	NC	35	NC
8	NC	36	NC
9	NC	37	NC
10	AGND	38	AGND
11	NC	39	NC
12	NC	40	NC
13	NC	41	NC
14	NC	42	NC
15	AGND	43	AGND
16	NC	44	NC
17	NC	45	NC
18	NC	46	NC
19	NC	47	NC
20	AGND	48	AGND
21	DIO0	49	SYNCLD
22	DIO1	50	DGND
23	DIO2	51	NC
24	DIO3	52	CTR
25	DIO4	53	DGND
26	DIO5	54	DIO CTL
27	DIO6	55	DGND
28	DIO7	56	+5V

Figure D.2: Diagram view of the MCCDAQ USB-3101. Figure adapted and modified from Measurement Computing.

waveform. The multifunction IO device is also responsible for acquiring PMT signals (voltage) at rates up to 5×10^6 samples per second [4].

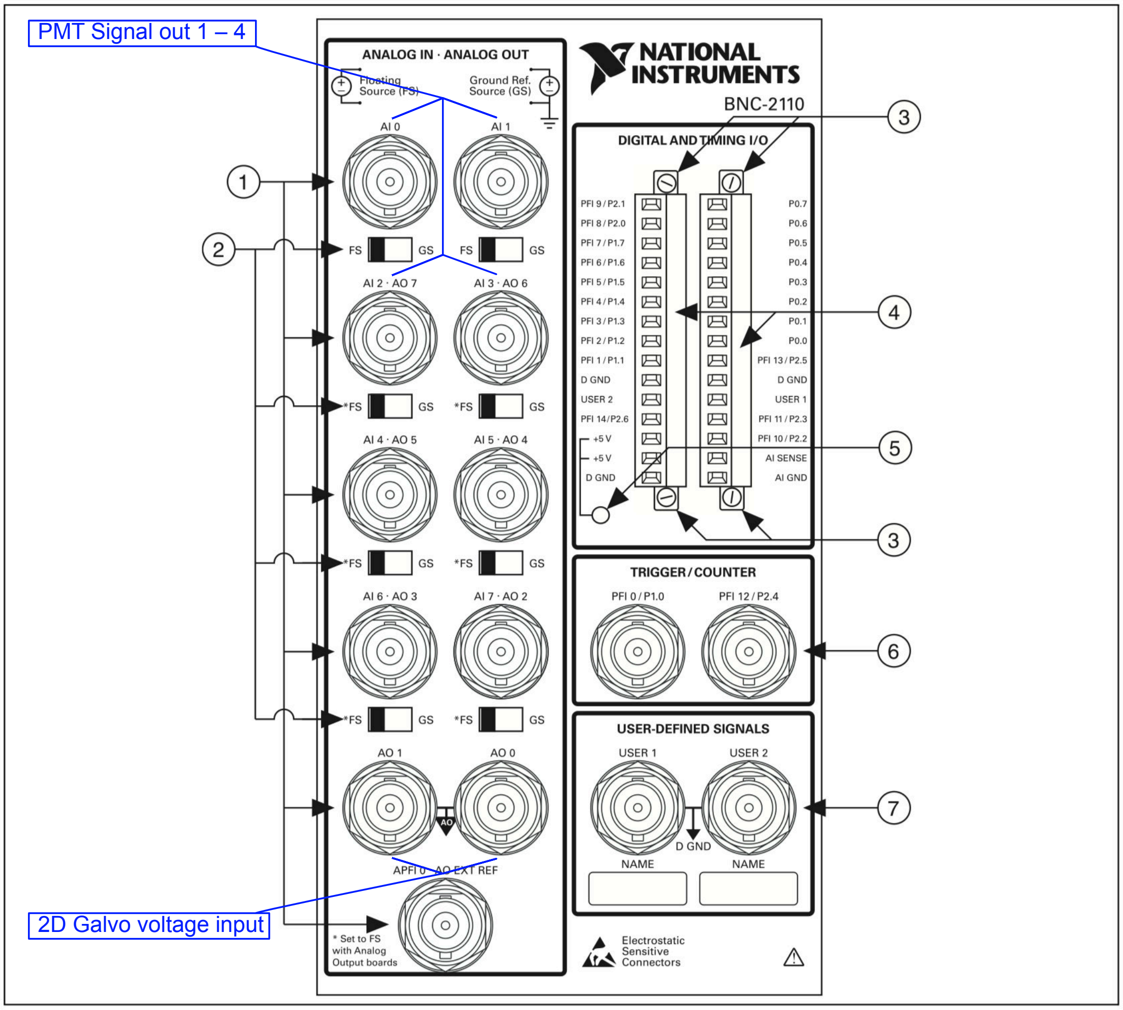

1 Analog Input/Analog Output BNC Connectors
2 FS/GS Switches
3 Terminal Block Retaining Screws
4 Digital and Timing I/O Spring Terminal Blocks
5 Power Indicator Light
6 Trigger/Counter BNC Connectors
7 User-Defined Signals BNC Connectors

Figure D.3: Connection of the PMTs and Galvos to a high-speed multifunction input/output device (National Instruments PCI-6110 with BNC2110 adapter). Figure adapted and modified from National Instruments.

Appendix E

Software developed for microscope control and data analysis

To aid with data acquisition, I wrote two software packages coded in LabView and Python 3. These software packages allow the synchronization between multiple instruments and can produce data significantly faster for my research purposes. For example, performing a high-resolution CARS calibration scan, such as in Fig. 2.3, may take several minutes to hours since for each delay stage position, a spectrum must be collected and then later collated and analyzed. By automating this procedure, a CARS calibration scan now merely requires a minute of alignment and a few minutes (usually less than ten) for the computer to acquire and analyze. The same is true for spectral surfing, without the aid of these software packages, spectral surfing would be a formidable task.

I have made these software packages open-source and accessible through Github.

- https://github.com/JeremyPorquez/MicroscoperPython

- https://github.com/JeremyPorquez/microscoper-LabView

Porting these software packages for use in other microscope systems require changing commands related to device movement and acquisition, therefore requires some knowledge of Python, LabView and in some cases, C programming.

MicroscoperPython

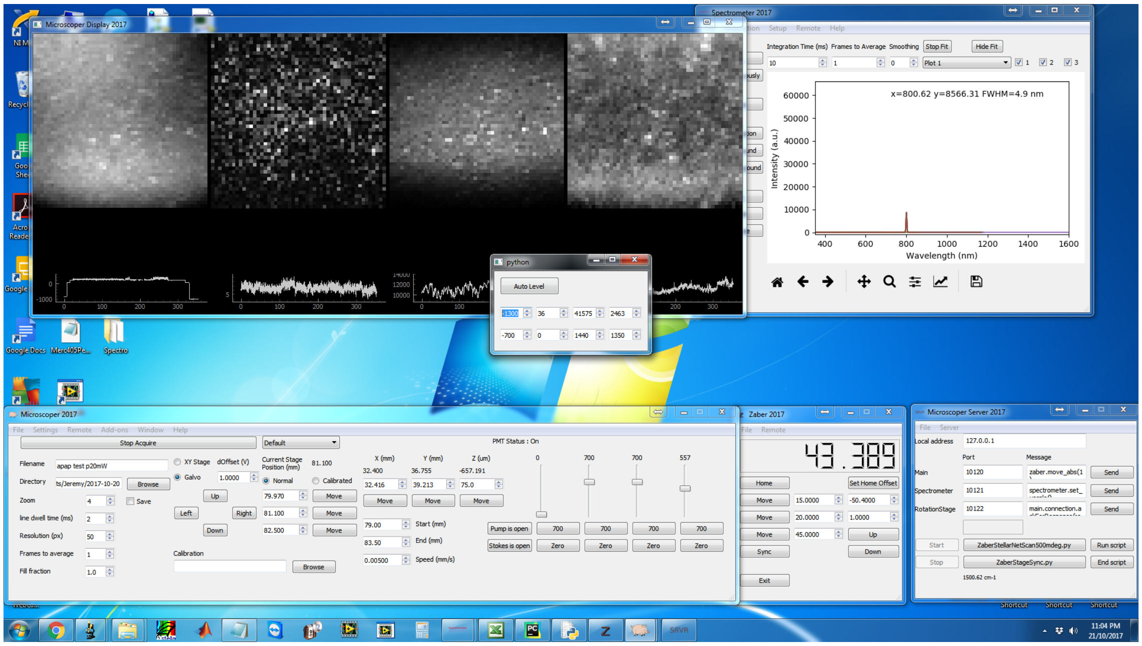

Figure E.1: Screenshot of the microscope control software written in Python. The code can be accessed on Github.

The MicroscoperPython is a Python version of the microscope software package. It requires Python3 to operate. The user interface is programmed using PyQt5. This version is the most updated version since Python is a fully open-source environment and thus many aspects are customizable.

MicroscoperLabView

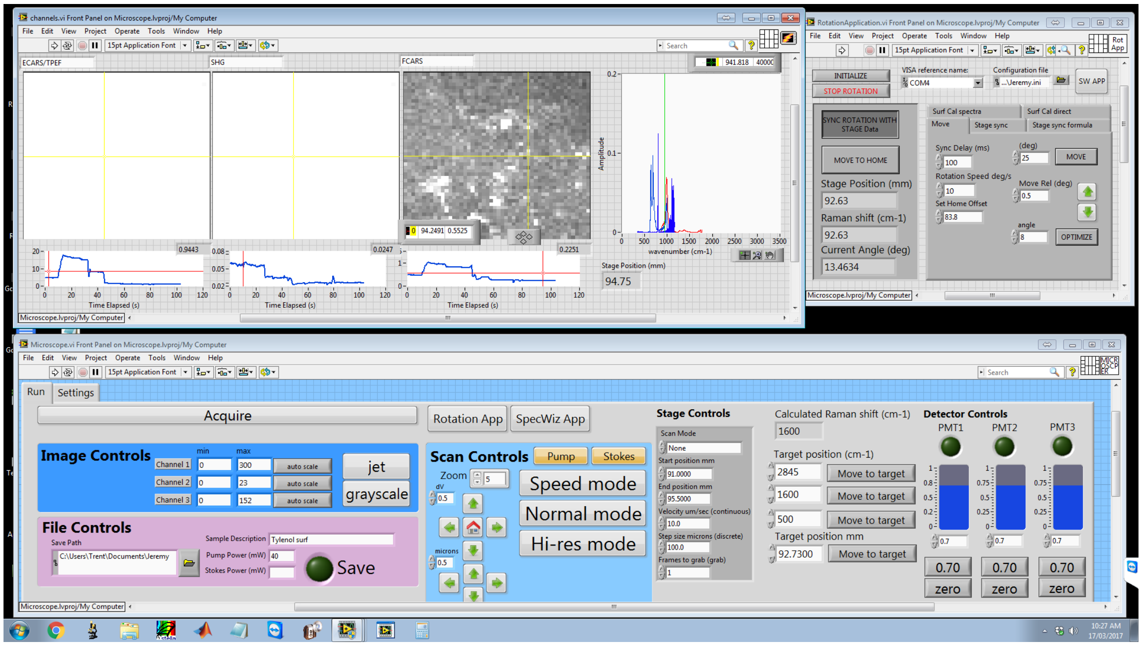

Stage Position (mm) 94.75

VISA reference name: COM4
Configuration file ...\Jeremy.ini
Stage Position (mm) 92.63
Raman shift (cm-1) 92.63
Current Angle (deg) 13.4634
Sync Delay (ms) 100
(deg) 25
Rotation Speed deg/s 10
Move Rel (deg) 0.5
Set Home Offset 83.8
angle 8

Channel 1 min 0 max 300
Channel 2 min 0 max 23
Channel 3 min 0 max 152
Save Path C:\Users\Trent\Documents\Jeremy
Sample Description Tylenol surf
Pump Power (mW) 40
Stokes Power (mW)
Zoom 5
dV 0.5
microns 0.5
Scan Mode None
Start position mm 91.0000
End position mm 95.5000
Velocity um/sec (continuous) 10.0
Step size microns (discrete) 100.0
Frames to grab (grab) 1
Calculated Raman shift (cm-1) 1600
Target position (cm-1) 2845
1600
500
Target position mm 92.7300
PMT1 0.7 0.70
PMT2 0.7 0.70
PMT3 0.7 0.70
10:27 AM 17/03/2017

Figure E.2: Screenshot of the microscope control software written in LabView. The code can be accessed on Github.

The MicroscoperLabView is a LabView version of the microscope software package. It requires a minimum version of LabView 2012 to operate.

Stage calibration software

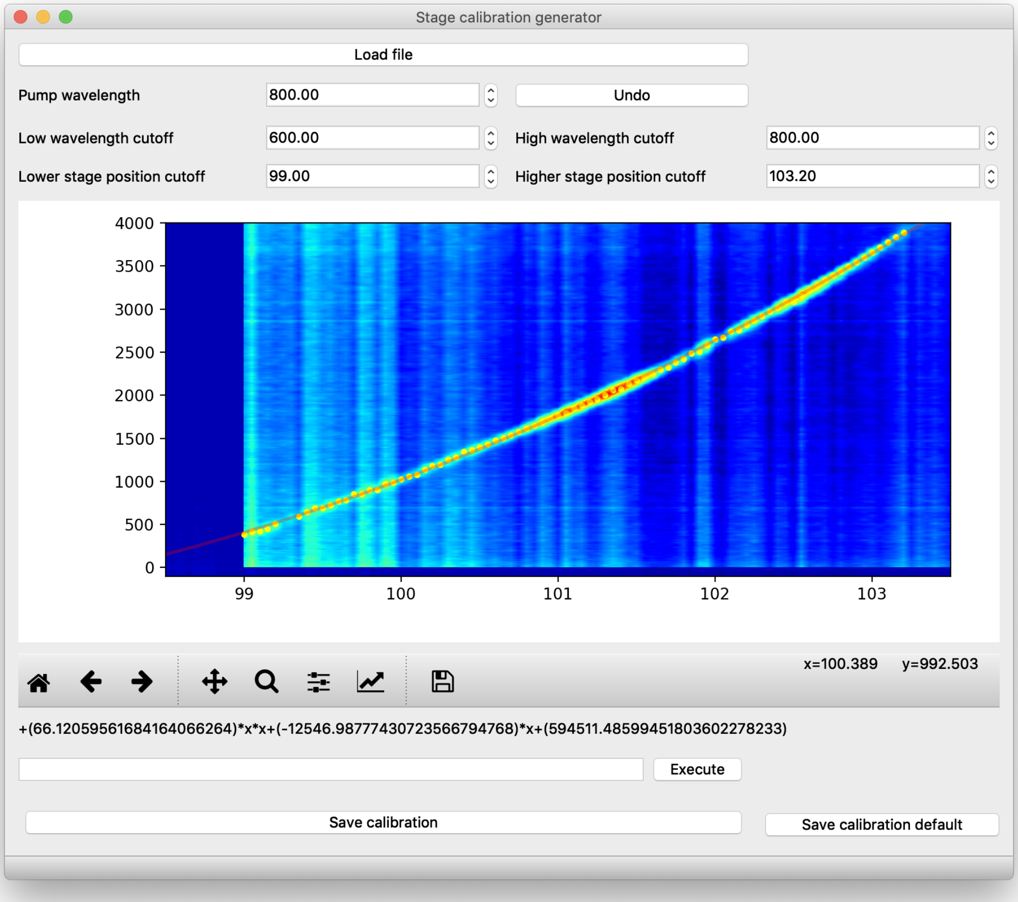

Pump wavelength 800.00

Low wavelength cutoff 600.00

High wavelength cutoff 800.00

Lower stage position cutoff 99.00

Higher stage position cutoff 103.20

x=100.389 y=992.503

```
+(66.12059561684164066264)*x*x+(-12546.98777430723566794768)*x+(594511.48599451803602278233)
```

Figure E.3: Screenshot of the stage calibration software written in Python. The code can be accessed on Github.

The stage calibration software takes a spectrogram that is generated through MicroscoperPython or MicroscoperLabView. The user can change parameters, filter the data, and remove outliers so the software can generate a calibration function. The vertical axis of the spectrogram represents the difference frequency and the horizontal axis represents the delay stage position.

Spectral surfing calibration software

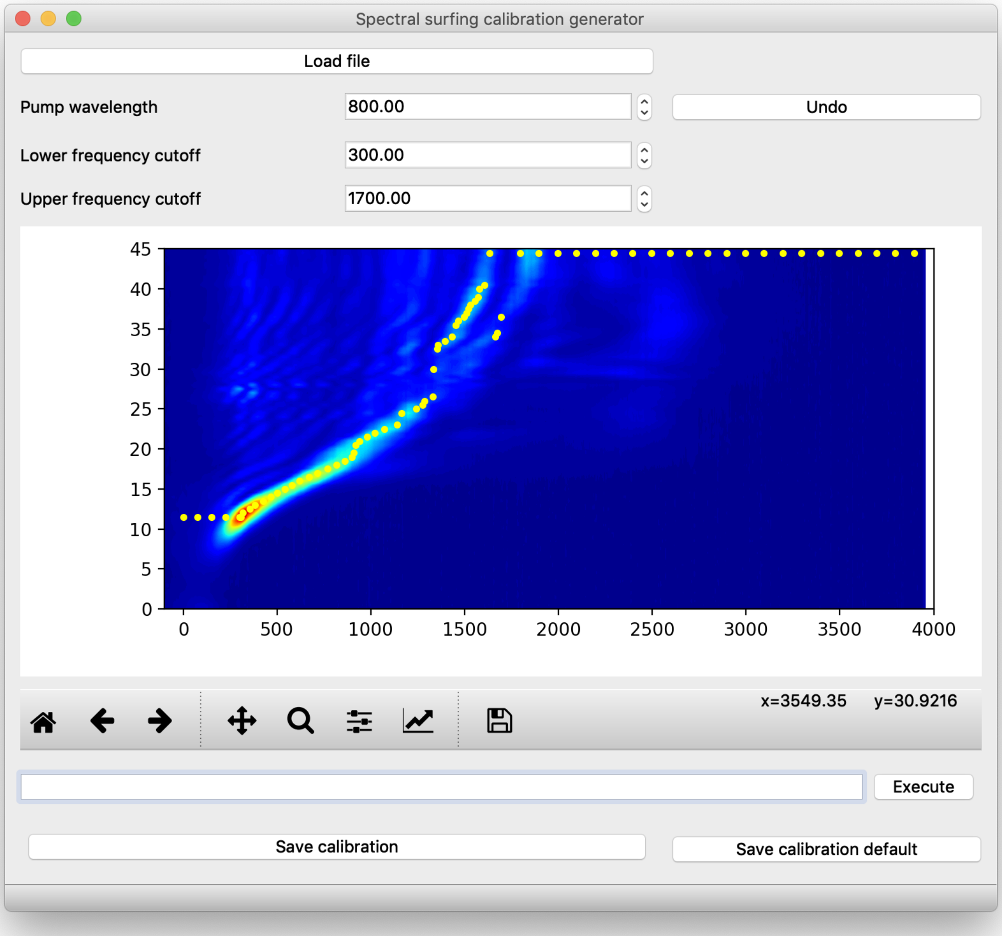
Spectral surfing calibration generator

Pump wavelength 800.00

Lower frequency cutoff 300.00

Upper frequency cutoff 1700.00

x=3549.35 y=30.9216

Figure E.4: Screenshot of the stage calibration software written in Python. The code can be accessed on Github.

The spectral surfing calibration software is similar to the stage calibration software. It takes a spectrogram that is generated through MicroscoperPython or MicroscoperLabView. The user can change parameters, filter the data, and remove outliers so the software can generate a spectral surfing calibration data. The vertical axis of the spectrogram represents the half-wave plate angle and the horizontal axis represents the difference frequency.

Appendix F

Different image acquisition methods for CARS

Acquiring higher quality CARS images can be done by prolonging scan times which can be done in several ways, two of which are acquiring dense hyperspectral data and acquiring multiple images at a certain vibrational frequency. Figure F.1 shows these two aforementioned methods. Figure F.1(a) is a high-quality CARS image of DMSO and benzonitrile acquired by taking single frames (500 × 500-pixel images) at a DMSO resonance at 2910 cm^{-1} and a benzonitrile resonance at 2230 cm^{-1}. Each frame took 2 seconds to acquire yielding a total image acquisition time of 4 seconds. Figure F.1(b), reproduced from Fig. 2.4, was acquired by taking a 200 × 200-pixel hyperspectral image that spans a wide range of frequencies yielding a total acquisition time of 9 minutes. Even though the higher quality CARS image (Fig. F.1(a)) was acquired in significantly less time, knowledge of the resonance locations of the sample must be known beforehand. Alternatively, high-quality CARS images can also be obtained from a single frame in a hyperspectral image through noise reduction and contrast enhancement procedures as detailed in Appendix I.

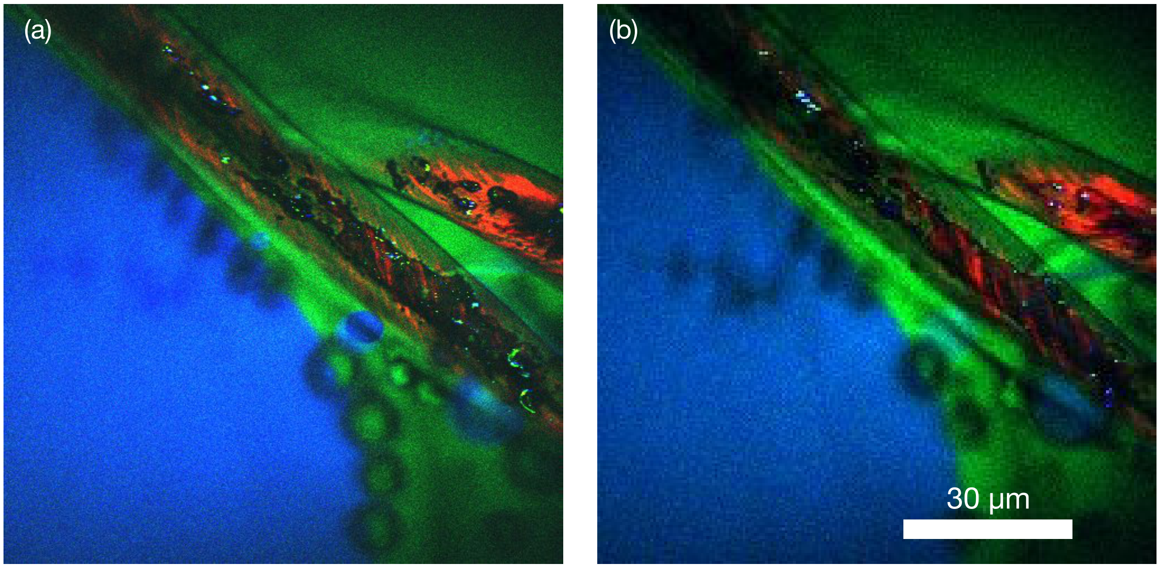

Figure F.1: Multimodal CARS images of benzonitrile, DMSO, and cellulose fibre. (a) 500 × 500 pixel multimodal CARS image where single frames were taken at discrete frequencies, 2230 cm^{-1} and 2910 cm^{-1} to generate the benzonitrile (blue) and DMSO (green) color maps, respectively. Similarly, a frame was taken from the SHG channel to generate the cellulose fiber color map (red). (b) Reproduced from Fig. 2.4; a 200 × 200 pixel multimodal CARS image obtained from a 900 frame CARS hyperspectral data where the DMSO color map was generated from an average of 13 frames centred at 2910 cm^{-1} and the benzonitrile color map was generated from an average of 12 frames centred at 3070 cm^{-1}.

Appendix G

Raman retrieval via time-domain Kramers-Kronig Relation

Much of the mathematical techniques in this section can be found in the textbook, Mathematical Methods for Physicists by George B. Arfken.

Theory

The susceptibility can be written as any function in terms of its modulus and phase

$$\chi(\omega) = \big|\chi(\omega)\big| e^{i\phi(\omega)} \tag{G.1}$$

And in using the property of logarithms

$$ln\big(\chi(\omega)\big) = ln\big|\chi(\omega)\big| + i\phi(\omega) \tag{G.2}$$

With $\ln(\chi(\omega))$ analytic in the upper-half of the complex plane. The susceptibility can be extracted by taking the contour integral, with a pole at $\omega' = \omega$ such that

$$\oint \frac{ln\big(\chi(\omega)\big)d\omega'}{\omega' - \omega} = P\int \frac{ln\big(\chi(\omega)\big)d\omega'}{\omega' - \omega} - i\pi ln\big(\chi(\omega)\big) \tag{G.3}$$

where P denotes the principal value—the value obtained in first revolution of the contour. The second term is due to the contour integral having a clockwise direction. The first term, on the right-hand side of the above equation can be expanded such that

$$\oint \frac{ln\big(\chi(\omega)\big)d\omega'}{\omega' - \omega} = P\int \frac{ln\big|\chi(\omega)\big|d\omega'}{\omega' - \omega} + iP\int \frac{\phi(\omega')d\omega'}{\omega' - \omega} - i\pi ln\big(\chi(\omega)\big) \tag{G.4}$$

Note that the complex integral, $\oint \frac{ln\big(\chi(\omega)\big)d\omega'}{\omega'-\omega}$, is equal to zero since it is analytic and circles the exterior of the contour (see Cauchys integral theorem [5]) thus we can write

$$\begin{aligned}
P\int \frac{ln\big|\chi(\omega)\big|d\omega'}{\omega' - \omega} + iP\int \frac{\phi(\omega')d\omega'}{\omega' - \omega} - i\pi ln\big(\chi(\omega)\big) &= 0\\
P\int \frac{ln\big|\chi(\omega)\big|d\omega'}{\omega' - \omega} + iP\int \frac{\phi(\omega')d\omega'}{\omega' - \omega} - i\pi\Big(ln\big|\chi(\omega)\big| + i\phi(\omega)\Big) &= 0\\
P\int \frac{ln\big|\chi(\omega)\big|d\omega'}{\omega' - \omega} + iP\int \frac{\phi(\omega')d\omega'}{\omega' - \omega} = i\pi\Big(ln\big|\chi(\omega)\big| - \pi\phi(\omega)\Big)
\end{aligned} \tag{G.5}$$

By equating both real and imaginary parts

$$\phi(\omega) = -\frac{1}{\pi}P\int \frac{ln\big|\chi(\omega)\big|d\omega'}{\omega' - \omega} \tag{G.6}$$

$$ln\big|\chi(\omega)\big| = \frac{1}{\pi}P\int\frac{\phi(\omega')d\omega'}{\omega'-\omega} \tag{G.7}$$

In CARS, the imaginary part of $\chi(\omega)$, is closely related to the Raman lineshape by first approximation at the resonance, i.e. $\Omega_R = \omega_P - \omega_S$ [6, 7]

$$\chi(\omega) = \frac{A}{i\Gamma_R} \tag{G.8}$$

Therefore,

$$I_{Raman} \propto Im\big(\chi(\omega)\big) \tag{G.9}$$

and

$$Im(\chi(\omega)) = |\chi(\omega)|sin(\phi(\omega)) \tag{G.10}$$

Therefore

$$I_{Raman} \propto= \big|\chi(\omega)\big|sin\Big(\frac{1}{\pi}P\int\frac{ln\big|\chi(\omega)\big|d\omega'}{\omega'-\omega}\Big) \tag{G.11}$$

Due to the length of the actual code, a flowchart is shown instead that follows the implementation of Liu *et al.* [8] is shown in Fig. G.1. However, a more recent work by Camp *et al.* can be accessed in ref. [6].

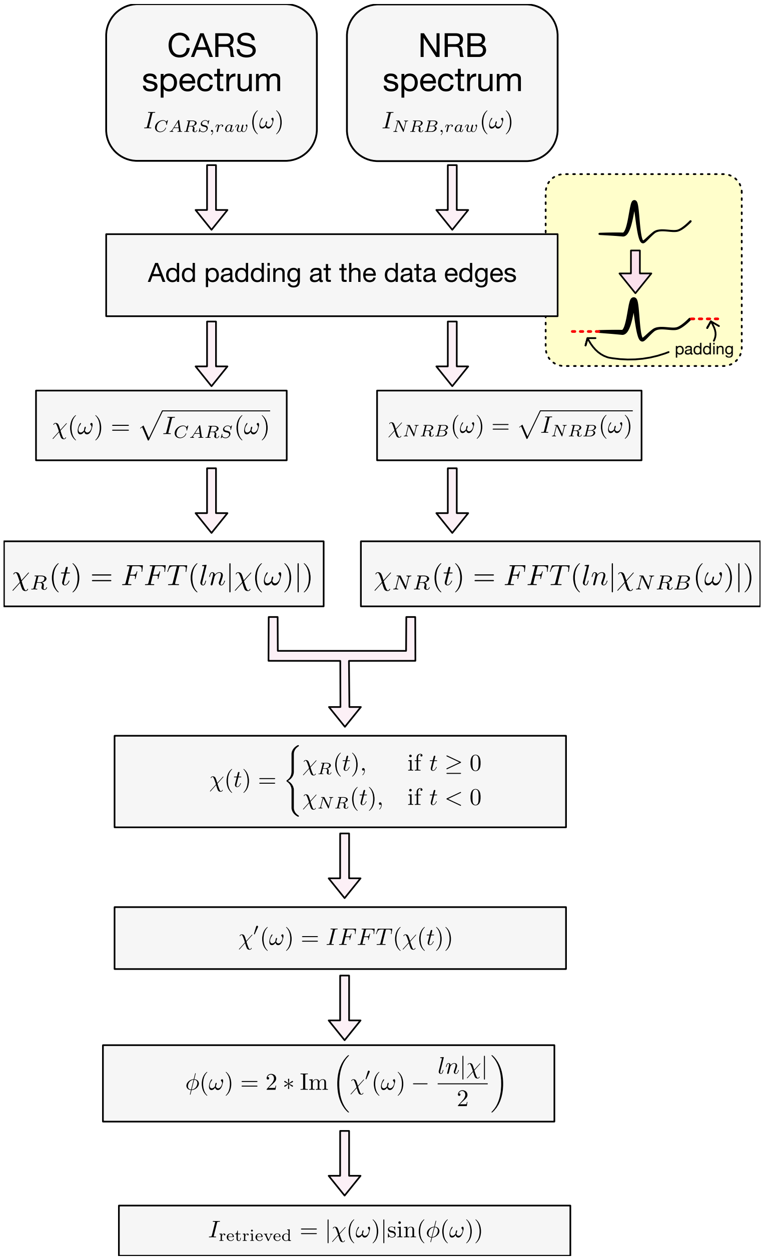

Figure G.1: Flowchart of the Raman-retrieval algorithm based on the Kramers-Kronig transform closely following the algorithm by Liu *et al.* [8].

Appendix H

Some considerations for spectral surfing

Spectral surfing is first implemented by acquiring a calibration curve through a power-dependence scan of the Stokes spectrogram as shown in Fig. H. As the pump delay stage moves, the spatial overlap of both pump and Stokes beam correspond to a difference frequency, $\omega_P - \omega_S$. A certain condition for powering the PCF, controlled by a HWP-polarizer pair, generates a Stokes that strongly stimulates the difference frequency which corresponds to the yellow dots. A computer automatically solves this HWP angle through a cubic spline fitting function based on the data (yellow dots).

To perform spectral surfing in a consistent manner, it is important to consider the stability of the laser oscillator. Most important to consider is that the oscillator should be operating properly in a mode-locked condition. Secondly, the bandwidth, duration, and the wavelength of the PCF pump pulse should be adjusted in order to obtain a smoothly traceable spectral surfing curve. Also shown in Fig. H.1 are different obtainable spectral surfing calibration curves with different PCF pump qualities.

With a high PCF pump bandwidth and decreased pulse duration, or in the unfortunate case when an imperceptible CW breaking (not highly mode-locked) occurs, spectral surfing becomes difficult to perform as shown in Fig. H(a). By decreasing the laser bandwidth and increasing the pulse duration, a spectral surfing curve can be established such that it can trace difference frequencies as close to 1900 cm^{-1} (or the 945 nm ZDW) as shown in Figs. H.1(b,c). This allows the PCF to function similar to a all-normal dispersion fiber but with the generation of a strong traceable soliton. In general, an ideal case for spectral surfing is when the supercontinuum generated by a fiber contains a single strong soliton within its ADR that is power-traceable up until it reaches the upper ZDW.

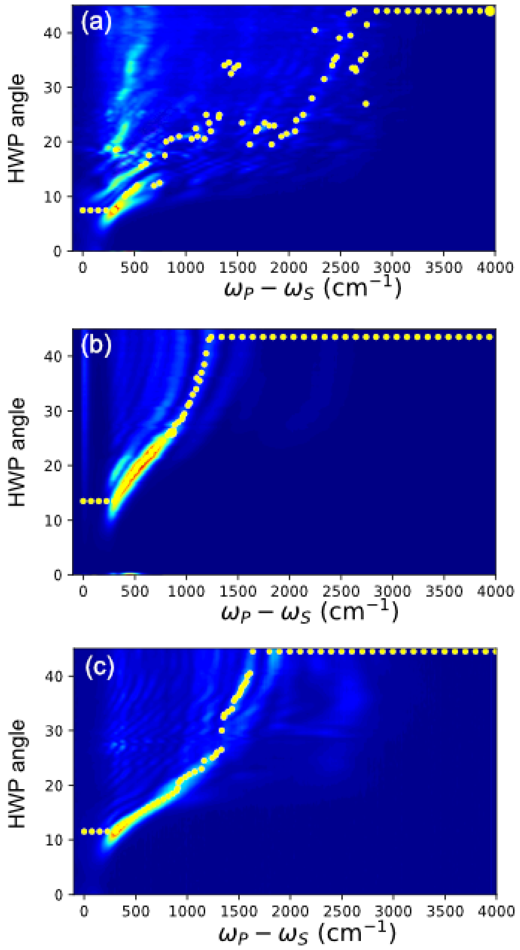

Figure H.1: Spectral surfing calibration curves. (a) Calibration curve with unoptimized PCF pump enabling reliable spectral surfing up to 600 cm^{-1}. (b) Calibration curve with optimized PCF pump allowing reliable spectral surfing up to 1300 cm^{-1}. (c) Calibration curve with better optimized PCF pump allowing reliable spectral surfing up to 1700 cm^{-1}.

Appendix I

Contrast enhancement and noise reduction of CARS hyperspectra

I.1 Contrast enhancement

SF-CARS has the advantage of acquiring dense hyperspectral data similar to multiplex CARS. This allows image-enhancement techniques that are easily applicable to such data sets. Contrast-enhancement in hyperspectral CARS images can be done by subtracting on-peak (crest) and off-peak (trough) resonance CARS images as shown in Fig. I.1. The technique is conceptually similar to the contrast enhancement techniques implement in differential-CARS [9] and frequency-modulated CARS [10], and has been demonstrated in ref [11]. This procedure exploits the dispersive nature of the CARS line shape and with sharp resonances, the NRB line shape is approximately constant thus also effectively zeroing out the NRB. However, the presence of a chemical with a similarly close may affect the contrast-enhancement procedure and yield sub-optimal results.

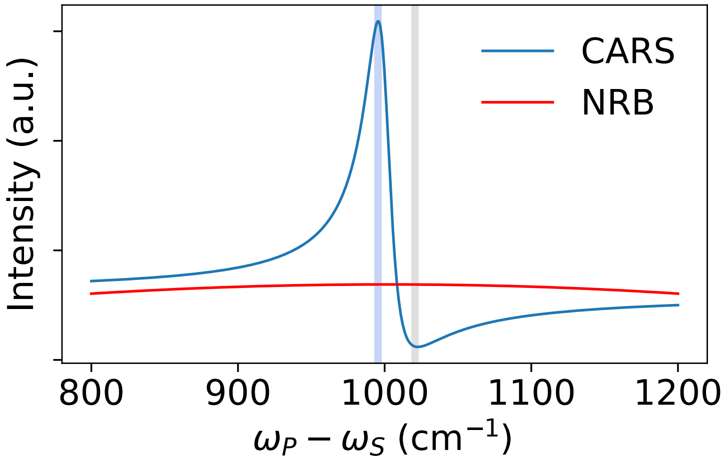

Figure I.1: Contrast-enhancement utilizing the CARS dispersive lineshape. The off-peak higher-frequency image components (gray highlight) are subtracted to on-peak, lower-frequency image components (blue highlight). Non-resonant components (NRB) of the image are also concurrently processed.

I.2 Singular value decomposition

Image enhancement can be performed using noise-reduction algorithms and one of the popular methods is singular-value decomposition (SVD). SVD separates unique spectral components (2D image) in a hyperspectral data (3D hyperspectra) therefore enabling unsupervised chemical mapping. Hyperspectral noise can be separated by keeping the first few singular values that primarily contain spectral information, e.g. the first 10 in most cases [12].

Before SVD, it is necessary to take the Anscombe transform of the hyperspectra. This transform can be approximated by taking the root intensity of the CARS hyperspectra [13, 14]. SVD can be subsequently applied and an inverse Anscombe transform retrieves the hyperspectra with reconstituted intensity levels. An excerpt of a *Python* algorithm based on *Numpy* is shown in Fig. I.2.

Functions

```python
def anscombe(data):
    return 2 * np.sqrt(data + 3. / 8)

def inverse_anscombe(data):
    return (data / 2.) ** 2 - 3. / 8

def svd_filter(data, full_matrices=False, singular_values=10, full_result=False):
    '''

    :param data:            3D numpy matrix with shape [spectra, y, x]

    :param full_matrices:   bool, optional
                            performs full SVD or reduced SVD

    :param singular_values: int, optional
                            number of first singular values to retain

    :param full_result:     bool, optional
                            returns SVD filtered image, U, S, V
                            else returns SVD filtered image

    :return:
                            SVD filtered image (optional: U, S, V with full_result = True)
    '''



    if not type(data) == np.ndarray:
        data = np.array(data)
    assert len(data.shape) == 3, 'data must be in 3-D'
    assert type(singular_values) == int
    z, y, x = data.shape
    svd_data = data.reshape((z,y*x))
    U, s, V = np.linalg.svd(svd_data,full_matrices=full_matrices)
    s_approx = s.copy()
    s_approx[singular_values:] = 0
    print('variance is {}'.format(s_approx.sum()/s.sum()))

    filtered_image = np.dot(U, np.dot(np.diag(s_approx),V))
    filtered_image = filtered_image.reshape((z, y, x))

    if full_result:
        return filtered_image, (U, s, V)
    else:
        return filtered_image
```

Command

```python
image = anscombe(image)
image = svd_filter(image, full_matrices=False, singular_values=10, full_result=False)
image = inverse_anscombe(image)
```

Figure I.2: Excerpt of Python code used to perform singular-value decomposition. The code is based on the Numpy package. The complete Python package can be accessed in ref [15].

I.3 Enhanced CARS hyperspectra

Fig. I.3 shows the results of the image enhancement algorithm. Fingerprint-based CARS images were generated by extracting image frames based on the 460 cm^{-1} resonance of benzonitrile (blue) and 670 cm^{-1} resonance of DMSO (green) while silent-CH-based CARS images were generated by extracting image frames based on the 2230 cm^{-1} resonance of benzonitrile (blue) and 2910 cm^{-1} resonance of DMSO. No averaging was performed on the 200 × 200 pixel CARS images as it was found to be unnecessary. With SVD and contrast-enhancement, the quality of the fingerprint CARS image is on par with the highly contrasting CARS images based on the silent-CH resonances.

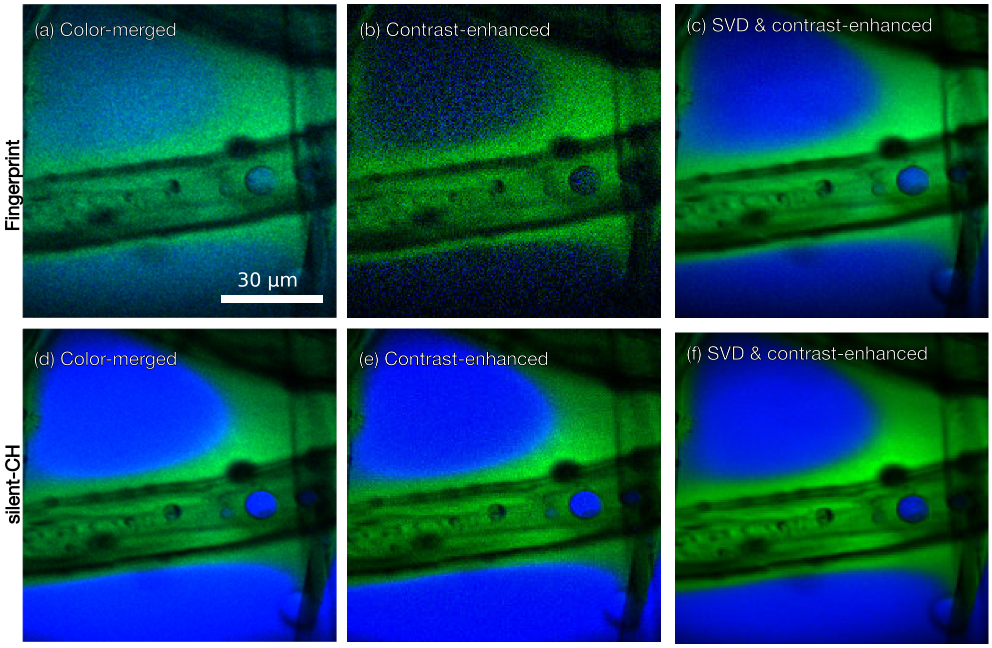

Figure I.3: Effect of noise-reduction on CARS images of benzonitrile and DMSO mixture in the fingerprint (top row) and silent-CH resonances (bottom row). (a) Color-merged, (b) contrast-enhanced, and (c) SVD, contrast-enhanced images of benzonitrile (460 cm^{-1}) and DMSO (670 cm^{-1}). (d) Color-merged, (e) contrast-enhanced, and (f) SVD, contrast-enhanced images of benzonitrile (2230 cm^{-1}, blue) and DMSO (2910 cm^{-1}, green).

References

1. Trebino, R. *Talks (Lectures)* `http://frog.gatech.edu/talks.html` (2018).
2. Hecht, E. *Optics* 5th (Pearson, 2016).
3. Saito, Y., Ishibashi, T. & Hamaguchi, H. Polarization-resolved coherent anti-Stokes Raman scattering (CARS) spectroscopy: a new probe of molecular symmetry through accurate determination of the Raman depolarization ratio. *Journal of Raman Spectroscopy* **31,** 725–730 (2000).
4. National Instruments. *NI PCI-6110/6111 Specifications* `http://www.ni.com/pdf/manuals/370980a.pdf` (2019).
5. Arfken, G. B., Weber, H. J. & Harris, F. E. *Mathematical Methods for Physicists* arXiv: `arXiv:1011.1669v3` (2013).
6. Camp Jr, C. H., Lee, Y. J. & Cicerone, M. T. Quantitative, comparable coherent anti-Stokes Raman scattering (CARS) spectroscopy: Correcting errors in phase retrieval. *Journal of Raman Spectroscopy* **47,** 408–415 (2016).
7. Tolles, W. M., Nibler, J. W., McDonald, J. R. & Harvey, A. B. A Review of the Theory and Application of Coherent Anti-Stokes Raman Spectroscopy (CARS). *Appl. Spectrosc.* **31,** 253–271 (1977).

8. Liu, Y., Lee, Y. J. & Cicerone, M. T. Broadband CARS spectral phase retrieval using a time-domain Kramers–Kronig transform. *Optics Letters* **34,** 1363 (2009).
9. Rocha-Mendoza, I., Langbein, W., Watson, P. & Borri, P. Differential coherent anti-Stokes Raman scattering microscopy with linearly chirped femtosecond laser pulses. *Optics letters* **34,** 2258–2260 (2009).
10. Ganikhanov, F., Evans, C. L., Saar, B. G. & Xie, X. S. High-sensitivity vibrational imaging with frequency modulation coherent anti-Stokes Raman scattering (FM CARS) microscopy. *Optics Letters* **31,** 1872 (2006).
11. Ryu, I. S., Camp Jr, C. H., Jin, Y., Cicerone, M. T. & Lee, Y. J. Beam scanning for rapid coherent Raman hyperspectral imaging. *Optics Letters* **40,** 5826 (2015).
12. Camp Jr, C. H. *et al.* High-speed coherent Raman fingerprint imaging of biological tissues. *Nature Photonics* **8,** 627–634 (2014).
13. Di Napoli, C. *et al.* Hyperspectral and differential CARS microscopy for quantitative chemical imaging in human adipocytes. *Biomedical Optics Express* **5,** 1378 (2014).
14. Bradley, J. *et al.* Quantitative imaging of lipids in live mouse oocytes and early embryos using CARS microscopy. *Development* **143,** 2238–2247 (2016).
15. Porquez, J. G. *CRASHyperspectralAnalysis* `https://github.com/JeremyPorquez/CRASHyperspectralAnalysis` (2018).